PolyPublie
Polytechnique Montréal

POLYTECHNIQUE MONTRÉAL
UNIVERSITÉ D'INGÉNIERIE

Titre: Development of a Global Digital Image Correlation Approach for Fast High-Resolution Displacement Measurements
Title:

Auteur: Farhad Mortazavi
Author:

Date: 2013

Type: Mémoire ou thèse / Dissertation or Thesis

Référence: Mortazavi, F. (2013). Development of a Global Digital Image Correlation Approach for Fast High-Resolution Displacement Measurements [Ph.D. thesis, École Polytechnique de Montréal]. PolyPublie. https://publications.polymtl.ca/1076/
Citation:

Document en libre accès dans PolyPublie
Open Access document in PolyPublie

URL de PolyPublie: https://publications.polymtl.ca/1076/
PolyPublie URL:

Directeurs de recherche: Isabelle Villemure, & Martin Lévesque
Advisors:

Programme: Génie mécanique
Program:

Ce fichier a été téléchargé à partir de PolyPublie, le dépôt institutionnel de Polytechnique Montréal
This file has been downloaded from PolyPublie, the institutional repository of Polytechnique Montréal

https://publications.polymtl.ca

UNIVERSITÉ DE MONTRÉAL

DEVELOPMENT OF A GLOBAL DIGITAL IMAGE CORRELATION APPROACH FOR FAST HIGH-RESOLUTION DISPLACEMENT MEASUREMENTS

FARHAD MORTAZAVI
DÉPARTEMENT DE GÉNIE MÉCANIQUE
ÉCOLE POLYTECHNIQUE DE MONTRÉAL

THÈSE PRÉSENTÉE EN VUE DE L'OBTENTION
DU DIPLÔME DE PHILOSOPHIÆ DOCTOR
(GÉNIE MÉCANIQUE)
MARS 2013

© Farhad Mortazavi, 2013.

UNIVERSITÉ DE MONTRÉAL

ÉCOLE POLYTECHNIQUE DE MONTRÉAL

Cette thèse intitulée :

DEVELOPMENT OF A GLOBAL DIGITAL IMAGE CORRELATION APPROACH FOR FAST HIGH-RESOLUTION DISPLACEMENT MEASUREMENTS

présentée par : MORTAZAVI Farhad
en vue de l'obtention du diplôme de : Philosophiæ Doctor
a été dûment acceptée par le jury d'examen constitué de :

M. AUBIN Carl-Éric, Ph.D., président
Mme VILLEMURE Isabelle, Ph.D., membre et directrice de recherche
M. LÉVESQUE Martin, Ph.D., membre et codirecteur de recherche
M. GOUSSARD Yves, Ph.D., membre
M. PIERRON Fabrice, Ph.D., membre

À mes parents :
Shirin et Mahmoud

À mes amours :
Maryam et Ava

ACKNOWLEDGEMENTS

Foremost, I would like to express my sincere gratitude to my supervisors, Professors Isabelle Villemure and Martin Lévesque for their time, support and most importantly, their trust throughout this thesis work. Your great interest and assistance encouraged me to be creative and persistent in my research.

I acknowledge the contributions of Luis P. Canal currently at École Polytechnique Fédérale de Lausanne and Elias Ghossein at École Polytechnique de Montréal for feeding this research very interesting experimental and numerical results necessary for the evaluations.

A great thank you goes to all my colleagues in office A-114, especially to Ali Shahvarpour for the fruitful discussions we had everyday, to Behzad Rahmani for his exchange of information between our closely related works, and to Amine El Mourid for his great helps and comments that greatly improved my French writings.

I would like to thank the Fonds Québécois de la recherche sur la nature et les technologies (FQRNT) for the financial support that made this project possible.

Finally and most importantly, I would like to express my gratitude to my family : to my beloved, Maryam, for her unwavering love and her encouragements not only as an extraordinary wife but also as a colleague, classmate and an expert in my domain of expertise ; to my beautiful and lovely Ava who has made each minute of my work full of pleasure since her entrance to our world 17 months ago ; To my wife's parents who devoted their past year exclusively to us and our daughter, your help was absolutely crucial to accomplish this thesis ; and last but not the least, to my parents who devoted all their life to my success. I wish you health and happiness throughout the rest of your life.

RÉSUMÉ

La Corrélation d'Images Numériques (CIN) est l'une des techniques de mesure de champs sans contact les plus répandues en mécanique expérimentale en raison de sa simplicité ainsi qu'à ses faibles coûts d'expérimentation. La multitude de mesures fournies par la technique a donné lieu à des applications dans différents domaines de recherche. Ces applications comprennent, sans s'y limiter, l'identification des propriétés mécaniques, la vérification de simulations numériques, la cartographie de déformations ainsi que le repérage de phénomènes locaux (par exemple, l'amorce de la plasticité ou de fissures). La CIN consiste à établir des corrélations spatiales entre deux images numériques acquises à partir de la surface d'un échantillon dans deux états différents de déformation. En outre, en utilisant des systèmes d'imagerie 3D pour acquérir des images en volume, la même méthode peut être utilisée pour corréler textures 3D dans les volumes, ce qui augmente la gamme d'application de la technique. Cette dernière est appelée la Corrélation de Volume Numérique (CVN).

La première approche de la CIN se fondait sur la corrélation de sous-fenêtres d'images dans toute la région d'intérêt, ce qui permettait de suivre le mouvement de points individuels sur la surface (plus récemment, dans le volume). Les vecteurs de déplacements ainsi mesurés étaient obtenus indépendamment les uns des autres, à la fois en termes de calcul et de base cinématique. Cette non-conformité des mécanismes de déformation entre les sous-fenêtres adjacentes pouvait réduire la fiabilité de mesures. En effet, à haute résolution, les hétérogénéités de déformation doivent être précisément capturées à des niveaux microstructuraux. Cette problématique a fait l'objet de recherches pour développer des approches globales, où un seul mécanisme de déformation était visé pour l'ensemble de la région d'intérêt en utilisant un grand nombre de Degrés de Liberté (DDL). Cependant, les algorithmes implémentés étaient coûteux en calcul, surtout pour les DDL élevés. Le problème devenait encore plus important dans le cas de la CVN, où une quantité énorme de données devait être récolté.

L'objectif principal de cette thèse était de développer et de valider une meilleure approche globale, permettant de concilier la précision et l'efficacité nécessaires pour des mesures à haute résolution, tant en 2D qu'en 3D.

Tout d'abord, une approche globale s'appuyant sur une décomposition spectrale pour le champ de déplacement recherché a été adoptée et améliorée par la suite. L'amélioration a consisté d'abord à modifier la base cinématique de corrélation avec des séries de Fourier. Cette modification a eu pour but d'améliorer la vitesse de convergence ainsi que de diminuer l'incertitude de mesure pour une vaste gamme de champs de déplacements. En outre, une stratégie particulière a été développée afin de corriger les effets de bords issus de fonctions

de base périodiques. L'algorithme développé a été testé à l'aide d'essais artificiels. Les résultats ont démontré la fonctionnalité des modifications apportées. De plus, l'algorithme a été comparé à l'approche locale. Il a été démontré que l'approche spectrale modifiée est plus performante que la méthode basée sur les sous-fenêtres grâce à son cadre global ainsi qu'à sa grande capacité d'estimation de déplacements complexes.

Deuxièmement, les applications potentielles de l'approche développée ont été étudiées pour les matériaux composites à l'échelle microscopique. Des images au Microscope Électronique à Balayage (MEB) de la surface d'une résine époxy renforcée par des fibres de verre à l'échelle microscopique ont été tirées de la littérature. Les bons paramètres de mesure ont été identifiés à l'aide d'une mesure à priori et des évaluations sur des expériences artificielles où les images MEB ont été artificiellement déformées selon une simulation éléments Finis (EF) de la microstructure reproduite. L'étude a également pris en compte l'effet du bruit enregistré. Les évaluations sur les essais simulés ont prouvé le grand potentiel de l'approche pour les mesures de champs de déformations à l'échelle de la fibre. La comparaison des résultats obtenus avec ceux déjà publiés antérieurement pour les mêmes images a révélé en outre cette capacité.

Enfin, l'approche développée a été étendue en 3D par un algorithme CVN-Spectral. Le potentiel de l'approche développée a été démontré par plusieurs expériences artificielles simulant les images en volume de composites à des échelles fines enregistrées avant et après déformation. La résolution appropriée d'imagerie pour la capture d'hétérogénéités de déformation a été estimée en fonction de la taille des particules et la résolution recherchée de déplacement en utilisant une analogie utile présentée dans l'approche 2D.

La principale contribution de cette thèse est le développement d'une approche globale pour une mesure précise de champs de déformations à haute résolution en 2D et 3D. Cette approche est très prometteuse pour la cartographie de déformation aux nivaux microstructuraux car elle concilie bien l'efficacité de calcul et la richesse de mesures. Présentement, il existe peu d'approches en 3D permettant des mesures à ce niveau de précision.

ABSTRACT

Digital Image Correlation (DIC) is one of the non-contact full-field measurement techniques widely used in experimental mechanics due to its simplicity and low experimental costs. The abundance of knowledge provided by the full-field measurement, has led to emerging applications in different areas of research. These applications include, but not limited to, mechanical properties identification, verification of numerical simulations, strain mapping and pinpointing local phenomena (e.g. onset of plasticity or cracks). DIC is based on establishing spatial relations between two digital images acquired from the surface of a specimen in two different deformation states. Furthermore, if volume images are acquired using X-ray tomography, for instance, the same image correlation method in 3D can be used to correlate the 3D texture within the volumes. The latter method is called Digital Volume Correlation (DVC) and leads to the measurement of internal strains, thus further extending the application range of the technique.

The earliest approach of DIC was based on the successive correlation of image subsets. The resulting motion vectors were thus obtained independently from each other, both in terms of computation and the kinematic basis. This nonconformity of the deformation mechanisms among neighboring subsets, however favorable for low-cost computations, may downgrade the measurement reliability, especially at high resolutions. This issue justified the development of global approaches, where one deformation mechanism was sought for the whole region of interest using a large number of Degrees of Freedom (DOF) and through correlating the whole region once and for all. However, the implemented algorithms became computationally expensive, especially at high resolutions. The problem became even more prominent for DVC measurements, in which a huge amount of data should be treated.

The main purpose of this thesis was to develop and validate an improved global approach that can reconcile the accuracy and computational efficiency needed for high-resolution measurements in 2D and 3D.

First, a global DIC approach based on Fourier decomposition for the sought displacement field was adopted and subsequently improved. The improvement consisted firstly in modifying the Fourier-based kinematic to achieve more rapid convergence and lower uncertainties for a wider class of displacement fields. Also, a special strategy was developed for properly correcting for the edge effects stemming from periodic basis functions. The developed algorithm was tested using computer-generated experiments, the results of which proved the functionality of the introduced modifications. Furthermore, it was fairly compared to the local approach. It was shown that the improved spectral approach outperformed the subset-based method in

equal conditions due to the global framework as well as the high capacity of the method in estimating complex displacements.

Second, potential applications of the developed approach were investigated for composite materials at micro-scale. Scanning Electron Microscopy (SEM) images from the surface of a Fiber-Reinforced Polymer (FRP) at micro-scale were taken from the literature. Suitable measurement parameters were identified using a priori measurements and evaluations on artificial experiments, i.e. Finite Element (FE) simulated displacement field of the exact microstructure artificially applied to the SEM images. The study also took the effect of the recorded noise into account. The evaluation on the simulated experiments proved the high potentials of the approach in measuring full-field strains in the fiber scale. Comparing the obtained experimental results with those previously reported for the same experiment in the literature further revealed this capability.

Finally, the developed global approach was extended to 3D leading to an improved spectral DVC approach. The potentials of the developed DVC technique were demonstrated by several artificial experiments simulating the volume images of composites at particle-scale recorded before and after deformation. Proper imaging resolution for accurate capturing of strain heterogeneities was estimated as a function of particle size and displacement resolution using a useful analogy presented in the 2D approach.

The main contribution of this thesis was the development of a global approach for accurate measurement of high-resolution full-field strains in 2D and 3D. This approach is very promising for strain mapping at micro-structural levels since it reconciles low computational costs and high sought resolutions. Especially, there are very limited approaches in 3D by now that enable measurements at this level of accuracy.

TABLE OF CONTENTS

LIST OF TABLES

LIST OF FIGURES

LIST OF ANNEXES

LIST OF SYMBOLS AND ABBREVIATIONS

$\mathcal{A}$	Set of admissible choices for DOF parameters $\mathbf{p}$
$B_{m,p}(\xi)$	B-Spline basis function of order p
d	Characteristic subset length defined in chapter 3. Aslo denoted by ℓ elsewhere
E	Isotropic elastic Young's modulus
E_f	Elastic Young's modulus of fiber in FRP
E_m	Elastic Young's modulus of matrix
E_p	Elastic Young's modulus of reinforcing particle
$f(\mathbf{x})$	Intensity function corresponding to the undeformed image
$f_e(\mathbf{x})$	Subset of the undeformed image defined over element e
$g(\mathbf{x})$	Intensity function corresponding to the deformed image
$g_e(\mathbf{x})$	Subset of the deformed image defined over element e
H_κ	Gaussian mask in the Fourier domain with cutoff wavenumber κ
$\hat{\imath}$	Imaginary unit $= \sqrt{-1}$
$\mathbf{J}_{mn}$	Jacobian tensor elements of the DIC governing equations (1.7a)
$\widetilde{\mathbf{J}}_{m-n}$	Jacobian tensor elements of the spectral DIC defined in equation (1.15a)
K	Total number of basis functions used to generate the sought displacement field
ℓ	Characteristic subset length
L	Image (smallest) half-width
$\mathbf{M}(\mathbf{x})$	Tensor field of the dyadic product $\nabla_{\mathbf{x}} g \otimes \nabla_{\mathbf{x}} g$ defined in chapter 3
N_n	Finite element shape functions
N	Total number of image pixels in chapter 3
$\mathbf{p}$	Set of unknown DOF in a pattern matching problem
$\mathbf{p}_e$	Element-based set of unknown DOF in FE-DIC
$u_n \quad (n = 1, 2, 3)$	Displacement components
$\mathbf{u}(\mathbf{x})$	Displacement vector field
$\mathbf{u}_e$	Element-based local displacement
$x_n \quad (n = 1, 2, 3)$	Spatial coordinates
$\mathbf{x}$	Spatial coordinate vector
$\mathbf{x}^{\langle n \rangle}$	Coordinate vectors of individual pixels (voxels)
$\nabla_{\mathbf{a}}\,[\,]$	Gradient operator containing partial derivatives with respect to vector $\mathbf{a}$

$\mathbf{E}[\,]$	Mathematical expectation
$\|\mathbf{a}\|_2^2$	ℓ^2-norm for vector $\mathbf{a}$ (also denoted by $\|\,\|^2$)
$\|\mathbf{A}\|_F^2$	Frobenius norm for matrix $\mathbf{A}$
$\mathbf{a}\otimes\mathbf{b}$	Dyadic tensor product of vectors $\mathbf{a}$ and $\mathbf{b}$
$\langle a(\mathbf{x})\rangle$	Spatial average of the function $a(\mathbf{x})$
$\mathcal{F}\{a\}_{[m]}$	Discrete Fourier transform of function $a(\mathbf{x})$
$\widetilde{a}(\boldsymbol{\omega}_m)$	Alternative notation for the Discrete Fourier transform used in chapter 3
$\widehat{a}(\mathbf{x})$	Frequency-domain filtered function using the Gaussian mask H_κ

Greek symbols

δ_{ij}	Kronecker's delta
$\widetilde{\delta}_{[n]}$	Impulse response in the Fourier domain
ε_{ij}	Elements of the infinitesimal strain tensor
κ	Gaussian filter cutoff wavenumber
λ_1	Smallest eigenvalue of a second-order tensor
ν	Isotropic Poisson's ratio
ν_f	Poisson's ratio of fiber in FRP
ν_m	Poisson's ratio of matrix
ν_p	Poisson's ratio of the reinforcing particle
$\boldsymbol{\rho}_m$	Right-hand side of the DIC governing equation (1.7a)
$\widetilde{\boldsymbol{\rho}}_{[m]}$	Right-hand side of the spectral DIC governing equation (1.17)
σ	Standard deviation of the white noise (noise level)
$\sigma_{\delta\mathbf{u}}$	Root mean square of the displacement correction at each iteration in the improved spectral approach
$\boldsymbol{\upsilon}_n$	Sequence of the vector amplitudes associated with basis function $\psi_n(\mathbf{x})$
$\psi_n(\mathbf{x})$	Basis functions used to define the sought displacement field
$\boldsymbol{\omega}_n$	Discrete radian frequency defined in the spectral decomposition (1.14a)
$\boldsymbol{\omega}^{\langle n\rangle}$	Alternative notation for the radian frequency defined in chapter 3
Ω_e	Domain of element e

Abbreviations

CCC	Cross-correlation coefficient
CM	Confocal microscopy
DFT	Discrete Fourier transform
DIC	Digital image correlation

DOF	Degrees of freedom
DVC	Digital volume correlation
FE	Finite elements
FEMU	Finite-element model updating
FFT	Fast Fourier transform
FRP	Fiber-reinforced polymer
GA	Genetic algorithm
IS-DVC	Improved spectral digital volume correlation
ISA	Improved spectral approach
ISACP	Improved spectral approach with cubic polynomial interpolation
ISACS	Improved spectral approach with cubic spline interpolation
LM	Levenberg-Marquardt
MNOS	Multi-scale non-linear optimization algorithm
NURBS	Non-uniform rational B-splines
PGD	Proper-generalized decomposition
Q4-FE	4-node quadratic finite element
RMS	Root mean square
ROI	Region of interest
SA	Spectral approach
SEM	Scanning electron microscopy
SO1	First-order subset
SO1CP	First-order subset with cubic polynomial interpolation
SO1CS	First-order subset with cubic spline interpolation
SO2	Second-order subset
SO2CP	Second-order subset with cubic polynomial interpolation
SO2CS	Second-order subset with cubic spline interpolation
SSD	Sum of squared differences
XFEM	Extended finite element modeling
ZOI	Zone of interest

INTRODUCTION

Many of the recent advances in theoretical solid mechanics are due to the quantitative observations made available by *experimental solid mechanics*. The latter describes the measurement of quantities representing the behavior of materials in response to loading. This includes essentially the measurement of strains at one or several locations. The availability of such information leads to the development and verification of analytical models and assumptions, as well as to the identification of characteristic properties.

The burgeoning growth in the complexity of analytical models necessitates the accessibility of numerous measurements to ensure the accuracy of parameter estimations and model verifications. Traditional strain gauge measurements have therefore become less practical for this purpose. On the other hand, techniques providing full-field measurements are of particular interest since they provide multiple displacement and strain readings in a single experiment. This wealth of knowledge, besides parameter estimation, has triggered other interesting applications such as strain mapping and full-field validation of numerical simulations.

There exists different full-field measurement methods with different levels of accuracy and convenience. Among them, Digital Image Correlation (DIC) has been widely used in experimental mechanics due to its low experimental costs as well as little amount of required post-processing of the recorded data. DIC is based on establishing spatial correspondences between two digital images acquired from the surface of a specimen in two different deformation states. The main requirement is the existence of a surface pattern by which the deformation can be tracked. This pattern may either be provided by the application of speckle patterns on the surface or stem from the intrinsic texture of the microstructure. The digital images may be acquired by various types of imaging systems, from optical cameras and microscopes to Scanning Electron Microscopy (SEM) imaging, etc. More interestingly, and thanks to the advances made in the 3D imaging technology, the framework of DIC can be extended to 3D, in which case it is referred to Digital Volume Correlation (DVC). With DVC, it is possible to non-destructively access the deformation behavior of the *inside* of materials.

With the remarkable achievements of DIC in macroscopic full-field measurements, there has been an increasing interest in capturing strain heterogeneities at the micro-structural level, which is referred to high-resolution measurements. The success of measurements at this level of accuracy depends, in the first place, on the versatility of the considered kinematic basis for the pattern matching process. Furthermore, the measurement reliability of DIC, as an ill-posed inverse problem, may be degraded by increasing the measurement resolution

unless meticulous attention is paid to the employed approach to solve the inverse problem.

The earliest and the most widely used approach of DIC relied on the correlation of subsets throughout the image to obtain full-field discrete measurements. However, the lack of inter-subset continuity increases the sensitivity of the local approach against noise and low intensity variations. This sensitivity is amplified at high sought resolutions, which consequently may lead to aberrant measured displacements at several points. These points should be smoothed out prior to differentiation to palliate their effects on the strain, which is subsequently detrimental to the measurement resolution.

In the past decade, several global approaches were presented to circumvent the inter-subset independency problem. The correlation problem was therefore solved for the global region of interest using a large number of Degrees of Freedom (DOF) for the kinematic basis of the deformation. However, the implemented algorithms became computationally expensive, especially at high resolutions. The problem becomes even more prominent for DVC measurements, in which a huge amount of data should be treated.

The main purpose of this thesis was to develop a global approach to DIC and DVC, which is both fast and reliable at high resolutions. The method is an improved approach based on a previously developed framework in 2D from the literature. The study had two main themes:

- To develop and validate the improved 2D DIC approach using both artificial experiments as well as experimental data from the literature
- To extend the developed 2D approach to 3D and investigate the potential applications at high resolutions

This thesis is organized as follows. Chapter 1 presents a literature review on the methods and applications of DIC and DVC. Chapter 2 introduces the objectives of the project according to the remarks made in Chapter 1, followed by relating the contributions of the publications to the research objectives. The three articles resulting from this work are included in Chapters 3 to 5. Chapter 3 introduces an improved global DIC approach, in response to the aimed objectives, and its validation. Chapter 4 studies potential applications of the approach for high-resolution strain measurements in composite materials using simulated and real experiments taken from the literature. Chapter 5 extends the improved approach to 3D and presents its potential applications in composites at particle scale. Chapter 6 discusses the connection between the articles and the reviewed literature. The contributions from this thesis are finally summarized and topics for future studies are recommended.

CHAPTER 1

LITERATURE REVIEW

1.1 Metrological definitions

Two terms in this thesis need to be defined first, namely, the notions of displacement resolution and spatial resolution. The following definitions are according to the ISO metrological vocabulary (ISO/IEC guide 99, 2007), which is also elaborated in (Surrel, 2004).

- **Displacement resolution:** The resolution of the measured displacement is the smallest change in the displacement to be measured that produces a perceptible change in the measured displacement. In this sense, the resolution is quantified by the level of noise in the measured displacement, which comes from numerous sources of error including (but not limited to) the image noise, gray level quantization and image distortions stemming from the optical technique. In physical units (other than pixels), it is also a function of the sampling resolution (magnification) of the imaging system.
- **Spatial resolution:** The spatial resolution is defined as the smallest distance between two points for which two independent measurements can be obtained. The spatial resolution of a full-field measurement algorithm (more generally measurement system) determines how many measurements can the full-field technique provide. Note that this resolution is defined in the spatial domain and is therefore inversely related to the well-known frequency-domain resolution (see chapter 3). Therefore, as opposed to the intuitive understanding, a smaller spatial resolution is more favorable. However, the term "high-resolution" is used in this thesis in its more intuitive sense and in consistence with the notion of frequency-domain resolution constituting the core of this thesis.
  It is well known that there is a compromise between the displacement resolution and the spatial resolution (as will be discussed in section 1.4.5). Also, note that the displacement smoothing, either through the use of continuous kinematic bases in the global approach (section 1.3.2) or using post-processing of the discrete measures in the local approach (section 1.3.1), increases the spatial resolution (less desirable) since it spatially correlates the measurement errors of the independent measurements.

1.2 Basic concepts

The underlying concept of pattern matching is to identify the displacement field by correlating an image taken from a specimen in the undeformed configuration with a second image

from its corresponding deformed configuration. The challenge is classified within the framework of *ill-posed* inverse problems (Aster *et al.*, 2005). A solution is found in the following way: a model with some unknown parameters is assumed to describe the displacement field, within a certain Zone of Interest (ZOI). These parameters act as DOF according to which the images are allowed to distort. The displacement field is applied to one of the two configurations within the ZOI (e.g. to correct for the deformed image back to the undeformed configuration). The duly mapped image is compared with its corresponding pair, and the parameters providing the best match are chosen as the solution to the problem. Figure 1.1 depicts the schematic of image matching mentioned above. A digital image is regarded as a matrix whose elements are positive integers, called intensity values, representing the surface brightness and each element is called a pixel. The matching criterion is the minimization of the Sum of Squared Differences (SSD) between intensity values of the image pair (Figure 1.1(c)) or equivalently, maximization of their Cross-Correlation Coefficient (CCC). Thus, one can write the aforementioned steps in the following mathematical formulation:

$$\mathbf{u}_{\text{exact}}(\mathbf{x}) \simeq \mathbf{u}(\mathbf{x}; \mathbf{p_{opt}}), \quad \text{such that} \tag{1.1a}$$

$$\mathbf{p_{opt}} = \arg\min_{\mathbf{p}\in\mathcal{A}} \left\{ \int_{\text{ZOI}} [f(\mathbf{x}) - g(\mathbf{x} + \mathbf{u}(\mathbf{x}; \mathbf{p}))]^2 \, \mathbf{dx} \right\} \quad \text{or} \tag{1.1b}$$

$$\mathbf{p_{opt}} = \arg\max_{\mathbf{p}\in\mathcal{A}} \left\{ \int_{\text{ZOI}} f(\mathbf{x}) g(\mathbf{x} + \mathbf{u}(\mathbf{x}; \mathbf{p})) \mathbf{dx} \right\} \tag{1.1c}$$

where $f(\mathbf{x})$ and $g(\mathbf{x})$ are the corresponding intensity functions of the undeformed and deformed images, respectively; $\mathbf{x} = (x_1, x_2, x_3)$ [1] is the coordinate vector in the cartesian space; $\mathbf{u}(\mathbf{x}; \mathbf{p})$ is the displacement field model with $\mathbf{p}$, the set of unknown DOF, $\mathcal{A}$ is the set of admissible choices for $\mathbf{p}$, and $\mathbf{u}_{\text{exact}}(\mathbf{x})$ denotes the real solution to be estimated through the minimization scheme. For the sake of simplicity, the above formulation is written assuming the intensity functions are continuous, hence the use of integral operators.

1.3 Solution strategies

Different approaches of DIC depend on how the sought displacement field is formulated. Irrespective of their formulation, the displacement fields for different approaches can be expressed as the linear combination of several chosen basis functions (Hild and Roux, 2012):

1. 3D coordinates are defined to maintain the generality within the whole document. However, it is reduced to 2D wherever the case may be.

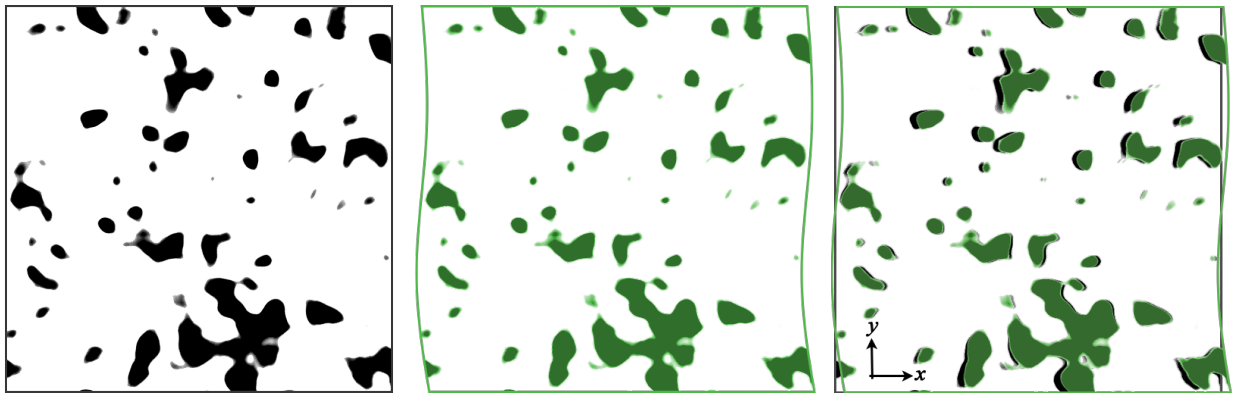

(a) ZOI, undeformed image (b) corrected ZOI, deformed image (c) pattern matching

Figure 1.1 Graphical illustration of DIC framework. One of the images is shown in green to make the two sets recognizable in (c)

$$\mathbf{u}(\mathbf{x};\mathbf{p}) = \sum_{n=1}^{K} \boldsymbol{\upsilon}_n \psi_n(\mathbf{x}) \quad \text{or in vectorial form} \tag{1.2a}$$

$$\mathbf{u}(\mathbf{x};\mathbf{p}) = \begin{bmatrix} \psi_1(\mathbf{x}) & \psi_2(\mathbf{x}) & \cdots & \psi_K(\mathbf{x}) \end{bmatrix} \begin{bmatrix} \boldsymbol{\upsilon}_1 \\ \boldsymbol{\upsilon}_2 \\ \vdots \\ \boldsymbol{\upsilon}_K \end{bmatrix} \tag{1.2b}$$

$$\text{where} \quad \mathbf{p} \equiv \{\boldsymbol{\upsilon}_n | n = 1, 2, \cdots, K\} \tag{1.2c}$$

where $\boldsymbol{\upsilon}_n$ are the series of unknown 2×1 (or 3×1 depending on the DIC dimensions) vectors associated with basis functions $\psi_n(\mathbf{x})$ and K is the total number of basis functions. The solution to the problem (1.1) is usually obtained through an iterative process, i.e. it starts with an initial solution $\mathbf{p}^{(0)}$ (leading to $\mathbf{u}^{(0)}$); at iteration i, $g(\mathbf{x}+\mathbf{u})$ is corrected for $\mathbf{u}^{(i-1)}$ and the new solution lies in finding the increment $\delta\mathbf{u}^{(i)} = \mathbf{u}^{(i)} - \mathbf{u}^{(i-1)}$.

Except for some approaches (Hild *et al.*, 1999; Pilch *et al.*, 2004; Jin and Bruck, 2005), a Newton iterative strategy is used to proceed with the mentioned iterations. It is assumed that the sought increment, $\delta\mathbf{u}^{(i)}$, is small enough so that one can linearize $g\left(\mathbf{x} + \mathbf{u}^{(i-1)}(\mathbf{x}) + \delta\mathbf{u}(\mathbf{x})\right)$ as:

$$g\left(\mathbf{x} + \mathbf{u}^{(i-1)}(\mathbf{x}) + \delta\mathbf{u}(\mathbf{x})\right) \approx g\left(\mathbf{x} + \mathbf{u}^{(i-1)}(\mathbf{x})\right) + \nabla_{\mathbf{x}}^{T} g\left(\mathbf{x} + \mathbf{u}^{(i-1)}(\mathbf{x})\right) \delta\mathbf{u}(\mathbf{x}) \tag{1.3a}$$

$$\text{provided that } \forall \mathbf{x},\ \|\delta\mathbf{u}(\mathbf{x})\| < \|\boldsymbol{\eta}\|. \tag{1.3b}$$

where $\boldsymbol{\eta}$ is a small real vector, $\nabla_{\mathbf{x}}$ denotes the gradient operator with respect to vector $\mathbf{x}$, and $\square^T$ indicates the vector transpose. Therefore, the First-order Optimality for the problem (1.1b) is written as:

$$\nabla_{\boldsymbol{v}_n}\left[\int_{\text{ZOI}}\left[f(\mathbf{x})-\breve{g}^{(i-1)}(\mathbf{x})-\nabla_{\mathbf{x}}^T\breve{g}^{(i-1)}(\mathbf{x})\delta\mathbf{u}(\mathbf{x};\mathbf{p})\right]^2\mathbf{dx}\right]=\mathbf{0}\quad n=1,2,\cdots,K \tag{1.4}$$

and

$$\breve{g}^{(i)}(\mathbf{x})=g\left(\mathbf{x}+\mathbf{u}^{(i)}(\mathbf{x})\right) \tag{1.5}$$

Upon differentiation, and after simplifications, equation (1.4), is turned into:

$$\begin{aligned}\int_{\text{ZOI}}\left(\nabla_{\mathbf{x}}^T\breve{g}^{(i-1)}(\mathbf{x})\begin{bmatrix}\psi_1(\mathbf{x}) & \psi_2(\mathbf{x}) & \cdots & \psi_K(\mathbf{x})\end{bmatrix}\begin{bmatrix}\boldsymbol{v}_1\\ \boldsymbol{v}_2\\ \vdots\\ \boldsymbol{v}_K\end{bmatrix}\psi_n(\mathbf{x})\nabla_{\mathbf{x}}\breve{g}^{(i-1)}(\mathbf{x})\right)\mathbf{dx}\\ =\int_{\text{ZOI}}\Big(\left(f(\mathbf{x})-\breve{g}^{(i-1)}(\mathbf{x})\right)\psi_n(\mathbf{x})\nabla_{\mathbf{x}}\breve{g}^{(i-1)}(\mathbf{x})\Big)\mathbf{dx}\qquad n=1,2,\cdots,K\end{aligned} \tag{1.6}$$

The above equation can be reorganized into a system of linear equations, i.e.

$$\begin{bmatrix}\mathbf{J}_{11} & \mathbf{J}_{12} & \cdots & \mathbf{J}_{1K}\\ \mathbf{J}_{21} & \ddots & & \vdots\\ \vdots & & \ddots & \vdots\\ \mathbf{J}_{K1} & \cdots & \cdots & \mathbf{J}_{KK}\end{bmatrix}\begin{bmatrix}\boldsymbol{v}_1\\ \boldsymbol{v}_2\\ \vdots\\ \boldsymbol{v}_K\end{bmatrix}=\begin{bmatrix}\boldsymbol{\rho}_1\\ \boldsymbol{\rho}_2\\ \vdots\\ \boldsymbol{\rho}_K\end{bmatrix} \tag{1.7a}$$

where $\mathbf{J}_{mn}$ and $\boldsymbol{\rho}_m$ are 2×2 (or 3×3) and 2×1 (or 3×1) matrices calculated as:

$$\mathbf{J}_{mn}=\int_{\text{ZOI}}\Big(\left(\nabla_{\mathbf{x}}\breve{g}^{(i-1)}\otimes\nabla_{\mathbf{x}}\breve{g}^{(i-1)}\right)(\mathbf{x})\psi_m(\mathbf{x})\psi_n(\mathbf{x})\Big)\mathbf{dx} \tag{1.7b}$$

$$\boldsymbol{\rho}_m=\int_{\text{ZOI}}\Big(\left(f(\mathbf{x})-\breve{g}^{(i-1)}(\mathbf{x})\right)\psi_m(\mathbf{x})\nabla_{\mathbf{x}}\breve{g}^{(i-1)}(\mathbf{x})\Big),\mathbf{dx} \tag{1.7c}$$

respectively, and $\otimes$ denotes the dyadic product. Equation (1.7a) is considered as the governing equation for the gradient-based pattern matching, and is used in different DIC approaches explained in the sequel.

1.3.1 Local DIC approaches

A popular approach to implement the strategy explained in section 1.2 and 1.3 is to discretize the sought displacement field on a selected grid. Figure 1.2(b) exemplifies the resulting displacement field from such an approach. The technique consists in the following steps: first a Region of Interest (ROI) [2] is selected on the reference image (Figure 1.2(a)), which is subsequently meshed with a set of evenly spaced grid points. The idea is to locate the new positions of the points on the deformed image so that the full-field displacements could be calculated. To this end, pattern matching is applied on subsets of the undeformed and deformed images. These subsets are selected so that their center points are located on the grid points. Thus, the ZOI in equation (1.1) for the measurements associated to each grid point is the local subset region considered for that point, hence the name local approach. For each subset, the unknown parameters of the displacement model is found using the governing equation (1.7a) in an iterative process. Once the model parameters are found, the displacement vector at the center point is stored and the procedure moves on to the next subset. Depending on the assumed displacement model, the measurement procedure could be either simplified to fast algorithms (non-gradient-based) or performed as nonlinear optimization schemes. The local displacement models are considered as polynomial functions of different orders. Polynomials up to the second-order can be stated in the following general form:

$$\mathbf{u}(\mathbf{x}) = \sum_{m=0}^{2} \sum_{n=0}^{m} \boldsymbol{\upsilon}_q x_1^{m-n} x_2^n \tag{1.8a}$$

and

$$q = \frac{m(m+1)}{2} + n + 1 \tag{1.8b}$$

Different model orders are discussed in the following:

• **Zero-order model:** When the assumed model contains only the first term of equation 1.8a, the model approximates any kind of deformation with a rigid-body translation. This approximation is valid for smooth displacement fields and by considering sufficiently small subset regions. One solution to this problem is to proceed through nonlinear optimization, as performed by Davis and Freeman (1998). However, one can note that the second objective function in Equation 1.1c simplifies to a standard cross-correlation product:

$$C(p) = \iint f(\mathbf{x}) g(\mathbf{x} + \mathbf{p}) d\mathbf{x} \tag{1.9}$$

2. The ROI and ZOI are distinguished from each other in this document. Indeed, the ZOI is a more general term, which may either refer to a subset or be extended over the whole ROI.

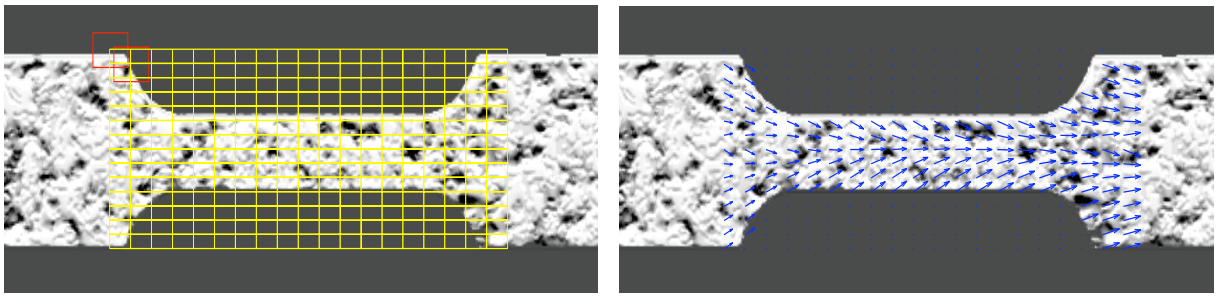

(a) (b)

Figure 1.2 Illustration of subset-based DIC (local approach). (a) The yellow rectangle denotes the ROI which is filled by evenly spaced grid points. The red square is the chosen subset (ZOI) used to find the displacement of the grid point located at its center point. (b) The typical displacement field resulted from subset-based measurement.

In the *discrete* cross-correlation product, the output is a matrix whose elements represent the realization of the above sum for an incremented value of p, and thus a local maximum could be located by searching through the elements of the cross-correlation matrix. Moreover, the calculation of the mentioned product could be performed in the frequency domain, where the correlation product simplifies to a simple product. Using the Fast Fourier Transform (FFT) (Chen *et al.*, 1993; Chiang *et al.*, 1997; Hild *et al.*, 1999), this approach highly increased the measurement speed.

• **First and second-order models:** First-order (Bruck *et al.*, 1989) and second-order models (Lu and Cary, 2000) provided better versatility to capture the spatial inhomogeneities in the displacement field, when compared to the zero-order model. Obviously, this came at the price of increasing the computational cost. Different iterative methods have been used to find the best model parameters. The Newton-Raphson method provided good results (Bruck *et al.*, 1989), but it required the second-order derivatives for the calculation of the Hessian matrix. However, as shown in section 1.3, the second-order terms could be neglected (by linearizing $g(\mathbf{x}+\mathbf{u})$) provided the initial solution is sufficiently close to the final solution. The initial guess could be calculated from a standard cross-correlation technique resulted from a zero-order assumption (Equation 1.9) while initially assuming zero values for the first-order terms (Vendroux and Knauss, 1998). The SSD criterion 1.1b was also use along with the Levenberg-Marquardt method to solve the minimization problem (Schreier and Sutton, 2002). While these methods were gradient-based and hence prone to get trapped in local extrema, Genetic Algorithms (GAs) were also used as an alternative being potentially able to converge to global extrema (Pilch *et al.*, 2004; Jin and Bruck, 2005). The large amount of required information for finding the global optimum, however, made GAs computationally

cumbersome.

It is worth noting that the mentioned subset orders allow for different DOF as illustrated in Fig. 1.3 Specifically, there are 2, 6 and 12 unknowns for zero- first- and second-order models. Besides these DOF, one additional unknown was also passed to the optimization problem to account for the brightness offset as a result of out-of-plane motion of the surfaces (Vendroux and Knauss, 1998; Lu and Cary, 2000). Finally, Bornert *et al.* (2009) used even higher-order terms in the subset formulation, including $x_1^2x_2^2$, $x_1^2x_2$, and $x_1x_2^2$ to assess different error regimes associated to subset-based DIC (as discussed in section 1.4).

• **Subset splitting at displacement discontinuities:** Poissant and Barthelat (2010) recently developed a new strategy for dealing with displacement fields containing discontinuities (cracks, shear bands, etc.) while using a local approach. The strategy (referred to as subset splitting) used the same first-order subset model for all subsets in the ROI in the first step of the correlation, while pinpointing the subsets requiring splitting according to their correlation coefficient magnitude. The located subsets were re-correlated using additional DOF, which allowed for splitting of the subsets according to an inclined line. The individual split subsets were then considered to each follow independent first-order models, hence calling for the optimization of 12 parameters per subset. Furthermore, the position and the slope of the splitting line was adjusted for each subset through the iterations. Evaluations on artificial and real experiments led to successful results, when compared to the classical subset-based method (Poissant and Barthelat, 2010).

1.3.2 Global DIC approaches

During the past decade, efforts have been made to implement DIC, within a global framework. In these approaches, the minimization problem (Equation 1.1b) was considered for the whole ROI all at once, i.e. instead of dealing with several small problems, one minimization problem was solved. Thus, the calculation of the matrices (1.7b) and (1.7c) of the governing equation (1.7a) necessitated integrations over the ROI (instead of ZOI). Moreover, a large number of DOF was required to model the sought displacement field. The integration ranges were reduced to smaller regions thanks to the use of basis functions with compact support Cheng *et al.* (2002); Besnard *et al.* (2006). For the same reason, the resulting Jacobian matrix (1.7b) became significantly sparse, hence being suitable for a sparse implementation of the algorithms (Cheng *et al.*, 2002; Besnard *et al.*, 2006). Several types of basis functions were used to formulate the sought displacement field, which is explained in the following:

• **FE-based displacement field:** Perhaps the most famous global approach is that based on FE shape functions (Sun *et al.*, 2005; Besnard *et al.*, 2006) due to its strong relation with the computational mechanics. Analogously to FE in solid mechanics, Besnard *et al.* (2006)

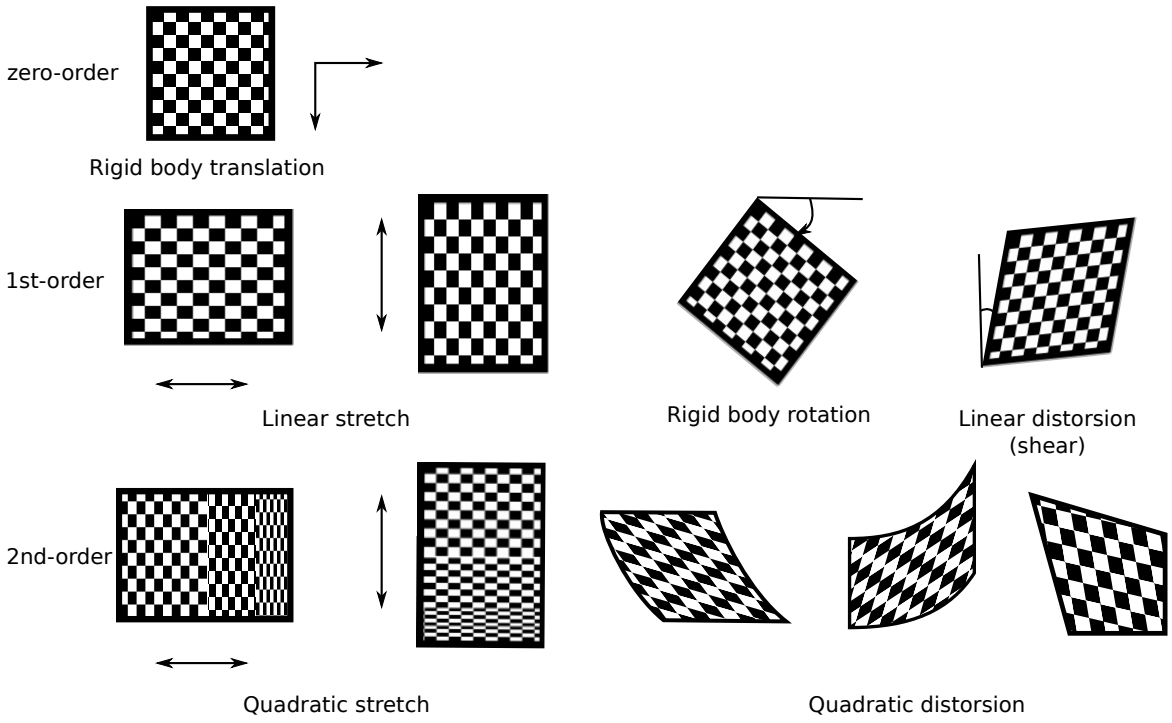

Figure 1.3 Illustration of various DOF for subsets with different orders.

meshed the ROI with bilinear rectangular elements (Q4-FE), so that the displacement field within each element could be described as:

$$\mathbf{u}_e(\boldsymbol{\xi}) = \sum_{n=1}^{4} \boldsymbol{\upsilon}_n N_n(\boldsymbol{\xi}) \tag{1.10a}$$

with

$$N_n(\boldsymbol{\xi}) \in \left\{ \begin{array}{cccc} (1-\xi_1)(1-\xi_2) & \xi_1(1-\xi_2) & (1-\xi_1)\xi_2 & \xi_1\xi_2 \end{array} \right\} \tag{1.10b}$$

where $\boldsymbol{\xi} = (\xi_1, \xi_2)$ denotes the local element coordinates defined in $[0,1] \times [0,1]$, and subscript e refers to the element index. With this local formulation, the global SSD criterion could be considered as the sum of local SSDs over all elements,i.e.:

$$\text{SSD} = \sum_{e=1}^{N_e} \int_{\Omega_e} \left[f_e(\boldsymbol{\xi}) - g_e(\boldsymbol{\xi} + \mathbf{u}_e(\boldsymbol{\xi}; \mathbf{p}_e)) \right]^2 \mathbf{d}\boldsymbol{\xi} \tag{1.11}$$

where f_e and g_e refer to the portions of f and g in the element domain, Ω_e, respectively. In the same way as explained in section 1.3, governing equation (1.7a) were locally established for each element (using Ω_e instead of ZOI), followed by an assembly of the so-called local *mass* matrices and *force* vectors (Besnard *et al.*, 2006). Sun *et al.* (2005) also used a

similar approach. In their work, they resorted to Newton-Raphson iteration with the same linearization of the Hessian matrix as explained in section 1.3. For the examples considered in (Sun *et al.*, 2005), they evaluated the convergence range of the optimization as ± 5 pixels [3]. Besnard *et al.* (2006) developed a different strategy to attack the minimization problem, namely, a multiscale scheme. The multiscale strategy consisted in down-sampling the images to sufficiently low sampling resolutions, so that the sought displacement field became in the order of a few coarse grains (the finest grain is a pixel in this sense). Thus, the iterations can start using zero values for the unknown DOF (or maximum a rigid body motion) by solving the governing equation (1.7a). The displacement field thus found was then interpolated to a smaller spatial resolution using the same basis functions as the DIC approach. The iterations continued until specific stopping criteria (objective function, displacement increment, etc.) were met.

Most of the studies that used FE-DIC were based on the Q4 finite elements. However, T3 elements (linear triangular) have been used as well (Leclerc *et al.*, 2009). Passieux and Périé (2012) recently used Proper Generalized Decomposition (PGD) with FE basis functions instead of the standard FE-DIC to reduce the dimensionality of the correlation problem. Using the separation of variables, the proposed methodology reduces a 2D (or even 3D) correlation problem to several computationally low-cost 1D problems based on 1D elements. Hence, the computational costs associated to the number of DOF was significantly reduced. The computational savings in the PGD-DIC, however, are highly dependent on the separability of the sought displacement field (Passieux and Périé, 2012).

One potential advantage of the FE-DIC discussed in (Besnard *et al.*, 2006) was the common language that it establishes in connection with the mechanical properties identification using the FE Model Updating (FEMU) method (Avril *et al.*, 2008). Indeed, the nodal displacements found from an FE-based DIC can be readily introduced into the FEMU algorithm without further need for interpolation or surface fitting. This possibility, however appealing, suffers from two shortcomings. Firstly, small and refined elements are essential for FE analyses on complex geometries in order for the FE solution to converge to the representative mechanical response of the body. This will necessitate, in turn, a large number of elements for the FE-DIC to match with the kinematic field of the FEMU. Therefore, the measurement time and computational cost becomes prohibitive unless one resorts to parallel computing (Leclerc *et al.*, 2009). Secondly, the displacement uncertainty in the FE-DIC is inversely proportional to the element size (see section 1.4). Thus, small elements lead to poor measurements, especially for regions where there is not enough texture intensity variations,

3. Convergence range is the range within which the difference between the initial and the actual solutions ensures the convergence during the optimization.

which becomes subsequently detrimental to the mechanical properties identification. The second limitation was overcome by Leclerc *et al.* (2009) by discarding the uncertain measured nodal displacements from the inverse identification and using only the non-free boundary elements as inputs to the FEMU. Alternatively, Réthoré (2010) developed a two-fold regularized FE-DIC, in which both the constitutive law parameters and the nodal displacements were identified simultaneously. The regularizing constraint, aiming at ensuring the equilibrium within elements, was updated as the mechanical parameters changed at each iteration. Thus, reliable measurements could be achieved even for small internal elements while simultaneously identifying the mechanical parameters.

Finally, it is worth noting that higher-order FE shape functions have been recently used within the same framework. For example, Hild *et al.* (2009) used Beam elements to directly measure DOF obeying the kinematics defined by the Euler-Bernoulli beam hypothesis (Hild *et al.*, 2009). More recently, Langerholc *et al.* (2012) employed planar isoparametric elements with 24 DOF to ensure the strain continuity across the elements. They used Newton-Raphson iterative procedure to minimize the SSD criterion.

• **Extended FE functions:** DIC approaches based on continuous displacement fields can not fully capture the the displacement heterogeneities in the vicinity of cracks (or other forms of displacement discontinuities such as shear bands). Although it is possible in Q4 FE-DIC to use very refined meshes around a crack (Réthoré *et al.*, 2005) while excluding the the crack itself from the ROI, this strategy has limited functionalities. Indeed, refined meshes are unfavorable in terms of both accuracy and computational time (as discussed earlier). The problem becomes even more prominent, in the presence of inclined cracks or discontinuities with irregular shapes. Recently, Réthoré *et al.* (2008a) implemented the principles of the eXtended FE Method (known as XFEM, Moës *et al.*, 1999) into the FE-DIC, hence allowing for enriched kinematic fields that allow for various kinds of discontinuities without the need for mesh refinements. In the proposed method, the original non-refined mesh was used while allowing for additional DOF with enriched bases for nodes of elements cut by the crack line. Réthoré *et al.* (2008a) also proposed a strategy to optimize the crack path configuration. With the proposed strategy, it was possible to evaluate the stress intensity factors (Roux and Hild, 2006; Réthoré *et al.*, 2009) as well as crack tip location (Réthoré *et al.*, 2009) with low uncertainties.

• **B-Spline functions:** Cheng *et al.* (2002) first used B-Spline functions to make displacement fields with continuous derivatives. These functions are piece-wise polynomials that unlike FE shape functions, may possess specified degrees of continuity making them very powerful and efficient in constructing smooth curves and surfaces. The displacement field in

2D thus defined is expressed as:

$$\mathbf{u}(\boldsymbol{\xi}) = \sum_{m=1}^{K_1} \sum_{n=1}^{K_2} \boldsymbol{\upsilon}_{m,n} B_{m,p}(\xi_1) B_{n,p}(\xi_2) \tag{1.12}$$

where $B_{i,p}(\xi)$ is the i-th univariate B-Spline basis function (of p-degree), $\boldsymbol{\xi} = (\xi_1, \xi_2)$ here is the normalized form of the (x_1, x_2) coordinates in the ROI so that they range within the parametric region $[0,1] \times [0,1]$, K_1 and K_2 are the total numbers of basis functions in each direction and $\boldsymbol{\upsilon}_{m,n}$ are the vector amplitudes associated to the 2D basis functions. To define a univariate B-Spline function, a knot sequence in the parametric space is needed, say $\{\xi^{\langle 1 \rangle}, \xi^{\langle 2 \rangle}, \cdots, \xi^{\langle K+p+1 \rangle}\}$, which is analogous to FE nodes except that B-Splines may include knots with multiplicities. Knowing the knot sequence, the B-Spline basis function is defined using the following recursive formula:

$$B_{m,0}(\xi) = \begin{cases} 1 & \xi^{\langle m \rangle} \leq \xi < \xi^{\langle m+1 \rangle} \\ 0 & \text{otherwise} \end{cases} \tag{1.13a}$$

$$B_{m,p}(\xi) = \frac{\xi - \xi^{\langle m \rangle}}{\xi^{\langle m+p \rangle} - \xi^{\langle i \rangle}} B_{m,p-1}(\xi) + \frac{\xi^{\langle m+p+1 \rangle} - \xi}{\xi^{\langle m+p+1 \rangle} - \xi^{\langle m+1 \rangle}} B_{m+1,p-1}(\xi) \tag{1.13b}$$

The DOF in this formulation can be considered as the displacements of the control points defining the shape of the whole region, which is similar to nodal displacements in FE method. However, unlike in FE-based transformation, the deformed shape does not necessarily coincide with the deformed *control net*. This is due to the fact that the B-Spline basis functions are not *interpolatory* (at least at interior knots), which leads to curves and surfaces of maximum C^{p-1} continuity. This advantage improves the versatility of the transformation without significantly increasing the number of DOF.

Cheng *et al.* (2002) used Levenberg-Marquardt method to minimize the SSD criterion. The initial solution was obtained from a B-Spline surface fitted to discrete displacement field from a primary subset-based measurement. Furthermore, they found the convergence range in the order of ± 3 pixels. Later, Réthoré *et al.* (2010), who used Non-Uniform Rational B-Splines (NURBS) in their study, employed the multiscale strategy of Besnard *et al.* (2006) instead of the Levenberg-Marquardt iterations. They also showed that the NURBS function improve on the uncertainty of the displacement fields and their derivatives when compared to FE shape functions.

• **Spectral approach:** Roux *et al.* (2002) and Wagne *et al.* (2002) introduced a very appealing approach based on the Fourier decomposition of the sought displacement field in 1D

and 2D, respectively. In this framework, the displacement field was expressed as:

$$\mathbf{u}(\mathbf{x}) = \sum_{n=-K/2}^{K/2-1} \boldsymbol{\upsilon}_n \exp(\hat{\imath}\boldsymbol{\omega}_n \cdot \mathbf{x}) \tag{1.14a}$$

where

$$\boldsymbol{\omega}_n \in \left\{ \left(\frac{i\pi}{L}, \frac{j\pi}{L} \right) \Big| -M \leq i, j \leq M-1, \, (M \leq L) \right\}, \tag{1.14b}$$

$K = 4M^2$ is the total number of basis functions, L denotes the ROI half-width and $M \leq L$ implies that only Fourier coefficients within a square of size $2M \times 2M$ were used to estimate the displacement field. In the extreme case where this square extends over the whole ROI size (i.e. $M = L$), the displacement field is aimed to be exactly reconstructed. However, this is not possible due to the ill-posed nature of the inverse problem. In their study, Wagne *et al.* (2002) showed that $M \ll L$ must be ensured in order for the approach to lead to meaningful results. It is easy to show that with the chosen formulation, matrix elements of the governing equation, i.e. equations (1.7b) and (1.7c), turn into the following Fourier transforms:

$$\mathbf{J}_{mn} = \mathcal{F}\left\{ \left(\nabla_{\mathbf{x}} \breve{g}^{(i-1)} \otimes \nabla_{\mathbf{x}} \breve{g}^{(i-1)} \right) \right\}_{[-m-n]} := \widetilde{\mathbf{J}}_{[-m-n]} \tag{1.15a}$$

$$\boldsymbol{\rho}_m = \mathcal{F}\left\{ \left(f - \breve{g}^{(i-1)} \right) \nabla_{\mathbf{x}} \breve{g}^{(i-1)} \right\}_{[-m]} := \widetilde{\boldsymbol{\rho}}_{[-m]} \tag{1.15b}$$

where the Fourier transform of a function $h(\mathbf{x})$ is defined as:

$$\mathcal{F}\{h\}_{[m]} = \int_{\mathrm{ROI}} h(\mathbf{x}) \exp\left(-\hat{\imath}\boldsymbol{\omega}_m \cdot \mathbf{x}\right) \mathbf{dx} \tag{1.16}$$

(note that only the Fourier terms within the $2M \times 2M$ square are calculated in equations (1.15a) and (1.15b)). Therefore, equation (1.7a) can be written in the following form using the Einstein notation:

$$\widetilde{\mathbf{J}}_{[m-n]} \boldsymbol{\upsilon}_n = \widetilde{\boldsymbol{\rho}}_{[m]} \quad \text{summation over } n \tag{1.17}$$

The left-hand side of the above equation is a convolution product. The main interest of the spectral approach lies in the fact that instead of directly solving equation (1.17) in the frequency domain, one may bring the calculations back to the spatial domain. Thus, the convolution operation turns into a simple matrix product in the real space. In doing so, equation (1.17) is transformed to the following practical form:

$$\left(\widehat{\left(\nabla_{\mathbf{x}} g \otimes \nabla_{\mathbf{x}} g \right)} \cdot \mathbf{u} \right)(\mathbf{x}) = \left(\widehat{(f-g)\nabla_{\mathbf{x}} g} \right)(\mathbf{x}) \tag{1.18}$$

where $\widehat{(\,)}$ denotes low-pass filtering in the frequency domain by preserving only $2M \times 2M$ coefficients. One faces here a 2×2 linear algebraic system for each point in the space. Such a system is analytically solved giving rise to two explicit expressions for the estimated displacement components. The main computational burden is performing a forward and a backward FFT to apply the Fourier low-pass filtering.

Wagne *et al.* (2002) used multiscale iterations for large displacement magnitudes. The developed strategy showed high reconstruction capacities while having drastically low computational costs. However, their approach suffered from a limitation stemming from the periodic nature of the utilized basis functions, i.e. the approach highly relied on periodic displacement fields and periodic images; a condition that is rarely met in real experiments. Meanwhile, this limitation was shown to be alleviated in 1D by using prior displacement correction using measurements based on a linear displacement model (Roux *et al.*, 2002) .

1.3.3 Global vs. local approaches

Both local and global approaches have been widely used in different applications. The local approach has been better established in the experimental mechanics community due to its simplicity, long history and dedicated comprehensive references (Sutton *et al.*, 2009). Furthermore, it is easy to be carried out on parallel computers due to the fact that the measurements for different points are done independently from each other (Gates *et al.*, 2011). This advantage, however, may become a drawback, when compared to the global approach. Indeed, the lack of inter-subset continuity increases the sensitivity of the local approach against noise and small image gradients (intensity variations). Consequently, aberrant displacements (Fig. 1.4) are sometimes measured, which should be smoothed out prior to differentiation to palliate their effects on the strain (Pan *et al.*, 2006a). The global approach, on the other hand, imposes additional spatial constraints so that the matching (DOF estimation) in one ZOI depends also on that of other adjacent zones, thus the conditioning of the inverse problem is improved. An analytical and numerical comparison of both approaches in response to noise has been addressed in (Hild and Roux, 2012), which validates this notion. Similar observations were made by other researchers while comparing local and global approaches (Cheng *et al.*, 2002; Sun *et al.*, 2005; Besnard *et al.*, 2006). By enforcing higher-order continuities, the radius of the dependence of DOF estimation mentioned above extends from adjacent ZOIs to even further regions as it is the case in high-order FE (Langerholc *et al.*, 2012), B-Splines (Cheng *et al.*, 2002), and the Fourier basis functions (Wagne *et al.*, 2002). In the latter, the dependence extends over the whole ROI due to the C^{∞}-continuity property of the mentioned functions. It should be noted that this regularization is not limited to continuity but also to the enforcement of discontinuity as it is the case in extended FE-DIC (Réthoré

et al., 2008a).

Another drawback of the local approach is related to its implementation, especially, as far as sub-pixel interpolation (see section 1.4) is concerned. Indeed, in a subset-based method, the subset spacing is so that there is significant overlapping between adjacent subsets. Technically, this means that repetitive image information are used each time to calculate interpolation coefficients per subset, which redundantly increases the computational cost of the algorithm. This problem was overcome in the case of DIC with cubic polynomial interpolation (Pan and Li, 2011) by using interpolation coefficients lookup table, which was calculated once for all pixels.

1.4 DIC uncertainties

Despite its simpler experimental setup compared to other techniques, the accuracy of DIC is not any less vulnerable to imperfect situations in the whole measurement process. Table 1.1 lists some of the most addressed sources of error, which are divided into those related to experimental setup or algorithmic sources. In all of the works related to error assessment, the purpose has been either to diagnose and quantify the impact of uncertainty sources so as to evaluate the measurement system resolution, or even to improve algorithms so as to reduce those uncertainties and thus increasing the reliability. In the following, the most relevant uncertainty sources are briefly discussed.

1.4.1 Correlation criterion

During a DIC experiment, it is very likely that the exposure and lighting of the reference and deformed images turn out to be different. This happens due to either a change in lighting condition or the fact that the texture pattern is deformed and thus reflects different intensities. This phenomenon, along with the noise effects on the intensity variations, can cause instability problems in the course of optimization. It is therefore recommended to use normalized correlation criteria to account for intensity changes of the acquired images.

Table 1.1 Uncertainty sources of DIC

Uncertainty sources	
Experimental	**Algorithmic**
Image acquisition	Correlation criterion
Texture pattern	Sub-pixel interpolation
Image noise	Reconstruction error
Optical device	

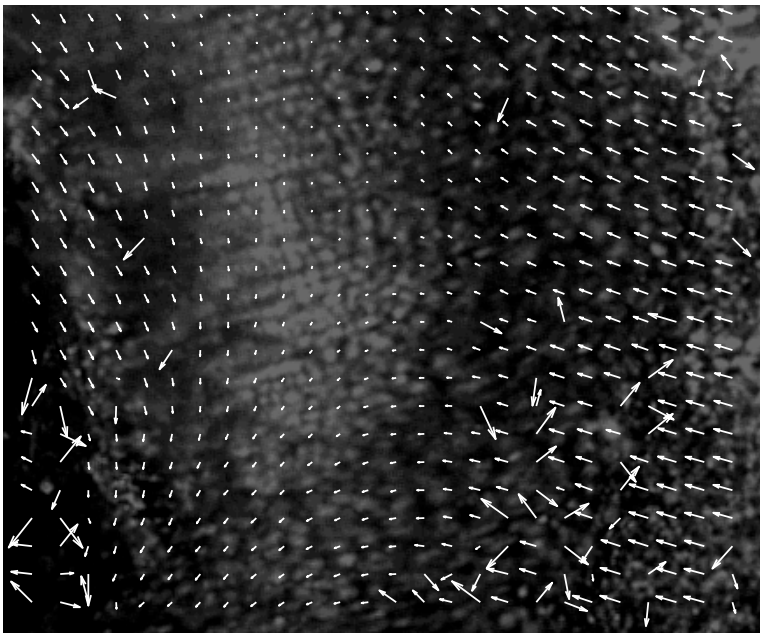

Figure 1.4 Typical aberrant measurements sometimes occurring in a local approach due to the independency of local DOF computation across adjacent subsets.

Different criteria have been used which are invariant to either a shift or a linear change in the intensity. An evaluation and comparison of different correlation criteria showed that, despite its additional complexity, a combined offset and linear change-invariant criterion shows better performance than just a linear or shift-invariant criterion, in terms of both noise-robustness and accuracy of the converged solution (Tong, 2005).

1.4.2 Sub-pixel interpolation

To perform the optimization required by the pattern matching, image functions and their derivatives are needed to be interpolated, hence making a continuous objective function. Different interpolation schemes are availbale from various categories of polynomials and splines (Lehmann *et al.*, 1999). In case of a zero-order displacement model, which leads to the standard cross-correlation product, the resulting correlation matrix was interpolated in the neighborhood of its peak to find the position of the *sub-pixel* peak (Hild *et al.*, 1999; Řiha *et al.*, 2007). This strategy is significantly fast; however, it does not guarantee a high sub-pixel accuracy. Due to the phase-shift error (Jähne, 2004) resulting from spatial interpolation schemes, all sub-pixel registration algorithms induce positional errors in measured displacements, the magnitude of which depends on the sub-pixel value of the actual displacement (Schreier *et al.*, 2000). Such phenomenon is easily observable in a set of incremental rigid-

body translation tests, in which the deformed image is a shifted version of the reference configuration. Figure 1.5 shows a typical systematic error caused by intensity interpolation in the translation test. Each of the values on the abscissa in this figure represents a sub-pixel value by which the specimen is translated in a separate test. The error values on the ordinate correspond to the mean difference between the measured and the actual displacements. This kind of systematic error (called interpolation bias) has detrimental effects on the strain accuracy when it is calculated from numerical differentiation. The exact quantification of these errors is very complicated and depends on the intensity variations specific to the surface pattern, noise etc. (Wang *et al.*, 2009). However, the comparison of different algorithms based on their corresponding produced errors of this kind is used for benchmarking the performance of different DIC-based approaches (Pan *et al.*, 2006b). A numerical study (Schreier *et al.*, 2000) has shown the necessity of using high-order sub-pixel interpolation schemes, typically bicubic spline (Unser *et al.*, 1993a,b), to obtain reliable strain measurements. Furthermore, it is possible to design optimal interpolation kernels for given kernel sizes that produce smaller bias compared to other interpolation methods with the same kernel size (Sutton *et al.*, 2009).

1.4.3 Texture pattern

Due to their ill-posed nature, accuracy and reliability of DIC-based measurements strongly depend on the variations of the intensity gradients, which is visually perceived as abundance of speckle-like features or textured patterns on/within the specimen. From a mathematical point of view, the displacement uncertainty is inversely proportional to the integral of image gradients' magnitude (Wang *et al.*, 2009; Roux and Hild, 2006; Pan *et al.*, 2010). This necessitates sufficient intensity variations within the images, which can be alternatively assessed from the image spectrum (as done in the spectral approach (Wagne *et al.*, 2002)) or the image autocorrelation function (Triconnet *et al.*, 2009). Quantitative study of the texture pattern leads to *a priori* estimation of the maximum attainable accuracy for a particular experiment. For example, Triconnet *et al.* (2009) proposed a methodology to evaluate the texture , in which two *a priori* criteria (i.e. minimum standard deviation and *representative* speckle radius) were introduced for this purpose.

It is worth noting that very efficient experimental methods have been developed to create rich patterns on the surface of metallic or polymeric materials at sub-micron levels (Scrivens *et al.*, 2007).

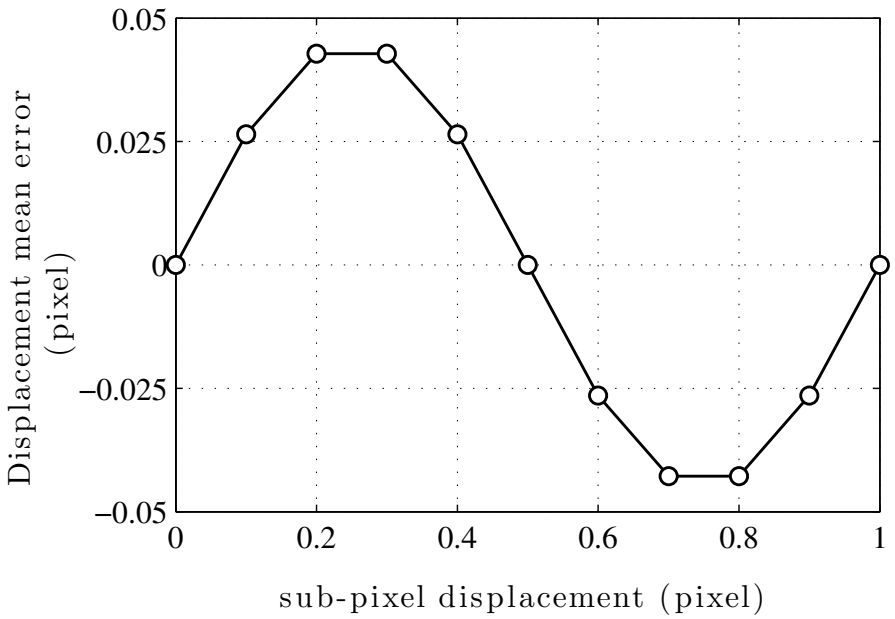

Figure 1.5 Typical systematic error caused by intensity interpolation. The sub-pixel displacement differs from the real position by an error whose value depends on the real sub-pixel position.

1.4.4 Noise

Undesirable random oscillations of gray levels are always recorded during image acquisitions due to various experimental reasons, which is referred to as image noise. Consequently, uncertainties in the measured data are inevitable. It is therefore necessary to determine the noise sensitivity of the measurement process. Remarkable studies have been done in the past few years to quantify noise-induced errors both in local (Wang *et al.*, 2009) and global approaches (Besnard *et al.*, 2006). In both works, the sensitivity to noise is inversely proportional to the intensity variations as discussed earlier. Wang *et al.* (2009) also showed that the noise induces additional interpolation bias as a result of image interpolation.

1.4.5 Reconstruction error

As mentioned in section 1.2, the displacement field is always approximated using basis functions to solve the inverse problem. The resulting error depends on the complexity of the sought displacement field and cannot be quantified unless for a priori known kinematic fields (Schreier and Sutton, 2002; Bornert *et al.*, 2009). However, it can be remedied by using a kinematic basis with smaller spatial resolution through choosing smaller subsets (in local approach), smaller elements (in B-Splines and FE approximation), or high-frequency

basis functions (in the spectral approach). However, as the spatial resolution decreases (more desirable), the DIC algorithm becomes more sensitive to noise and interpolation error (depending on the texture richness) (Bornert *et al.*, 2009; Triconnet *et al.*, 2009; Besnard *et al.*, 2006), hence the displacement resolution is decreased (less desirable). This is due to the fact that smaller elements or subsets contain less information in terms of intensity variations to establish reliable correlations. Two divergent trends for the uncertainty can be thus observed as a function of the spatial resolution. In practice, it is at the discretion of the user to determine optimum spatial resolutions for which a compromise is achieved between estimating a displacement field rich in details and keeping the noise-induced uncertainties (as well as interpolation bias) at low levels. Such decisions, besides the information about the noise level, would also require some a priori knowledge about the overall complexity of the displacement field (e.g. through finite element analysis). In that case, it is possible to determine the optimal parameters by performing simulated experiments (Canal *et al.*, 2012).

1.5 Digital volume correlation

The theoretical concepts of DIC can be easily developed into three dimensions, in which case it is called Digital Volume Correlation (DVC). The primary requirement is a 3D imaging system capable of acquiring three-dimensional digital images of a specimen. X-ray tomography, Confocal Microscopy (CM), and Scattered Light are some of available methods mostly used in the literature for this purpose (see Bay *et al.*, 1999; Franck *et al.*, 2007; Germaneau *et al.*, 2008, for instance). However, practical issues related to image acquisition, storage, and calculation have not only limited the applications of DVC to feasible cases but also hindered the full exploitation of DIC accuracy. Some of these issues are briefly discussed in the following:

• **Choice of material:** Not all kinds of materials can reveal enough inherited contrast for DVC. As for X-ray tomography, this contrast should stem from the difference between the capacity of the constituent phases in attenuating the emitted X-ray energy. Materials with cellular or granular structures have shown to be suitable for this purpose (Bay *et al.*, 1999; Roux *et al.*, 2008; Forsberg *et al.*, 2008; Forsberg and Siviour, 2009; Hall *et al.*, 2010). Metal matrix composites, such as nodular graphite cast iron (Réthoré *et al.*, 2011) or man-made composites (Bornert *et al.*, 2004), have also been studied. In the latter (as well as in (Barranger *et al.*, 2010)), small particles can be added during the elaboration process in order to create the required texture. These particles should be chosen so as not to significantly alter the overall mechanical properties (Bornert *et al.*, 2004).

• **Imaging artifacts:** Spurious features are normally produced during the reconstruction

procedure and do not belong to the texture of material. Although image pre-processing partly alleviates the problem (Forsberg, 2008; Germaneau *et al.*, 2008), further regularization of the inverse problem might be required for DVC at small spatial resolutions (Leclerc *et al.*, 2011).

• **Computational complexities:** As a result of the extension from 2D to 3D, the amount of data as well as the number of DOF for DVC is significantly increased in both local and global approaches, when compared to their 2D counterparts. Consequently, DVC algorithms are highly demanding in terms of computer resources. This limitation has hindered the application of DVC for complex displacements and strains. Having been first introduced by Bay *et al.* (1999), its early version was an extension of the local DIC approach with a zero-order subset mode. The minimization of SSD was achieved using Levenberg-Marquardt method along with a tricubic interpolation for obtaining sub-pixel values. Later, more accuracy was added to the technique (Smith *et al.*, 2002) by taking into account rotation parameters in the displacement model, i.e. 3 parameters for translation and 3 for rotation. Verhulp *et al.* (2004) considered a displacement model of the first-order representing an affine transform of the subset. This involved minimization of 12 parameters. In their work, besides the improvement on the displacement model, they used normalized CCC as objective function, which was minimized by a Quasi-Newton technique. Others preferred simpler algorithms, in which a trilinear interpolation method was used to evaluate the objective function at sub-pixel locations (Bornert *et al.*, 2004; Germaneau *et al.*, 2008). Also, a simple steepest descent strategy was substituted for the Quasi-Newton method in the two mentioned works. In a completely different approach, Franck *et al.* (2007) demonstrated a *stretch*-correlation technique, in which displacement parameters, capable of modeling only pure stretch were identified in the Fourier domain at a faster speed. Higher-order subvolume models have been also implemented. Forsberg *et al.* (2010) used Chebyshev basis functions to formulate the displacement field within subvolumes. They also used a special weighted average to interpolate the discrete displacement field at points other than the subvolume centers.

As in the case of DIC, implementation of a global approach is advantageous provided the resulting minimization problem is amenable to solve. Yoshikawa *et al.* (2006) extended the B-Spline-based DIC (Cheng *et al.*, 2002) into 3D along with an incompressibility constraint on the optimization procedure. Roux *et al.* (2008) developed the FE-based approach (Besnard *et al.*, 2006) to 3D to obtain displacement fields using 8-node cubic (trilinear) elements. The 3D algorithm underperformed its 2D counterpart due to several simplifying replacements in the algorithm steps. For instance, the FFT-based calculation of image gradients was simply replaced with finite differences to reduce the computational costs. Recently, Leclerc *et al.* (2011) have furthered improved the algorithm by adding a mechanical constraint enforcing the equilibrium on elements. Therefore, voxel-scale measurements can be achieved using a

more robust correlation. Extended FE-DIC was also extended to 3D (Réthoré *et al.*, 2008b), hence allowing for extracting stress intensity factors in 3D (Réthoré *et al.*, 2011)

1.6 Applications

The main characteristic distinguishing the full-field measurement techniques from traditional approaches, such as strain gauge measurements, is the abundance of knowledge that they provide from a single mechanical test throughout a whole region of interest. This remarkable advantage has led to many emerging applications since its early use in experimental mechanics (Sutton *et al.*, 1983). Some of these applications, related to DIC and DVC, are briefly introduced in the following:

- **Identification:** One famous application of DIC is in the field of material parameters identification. The large amount of provided experimental data enables identification of better constitutive laws (Réthoré *et al.*, 2013), mechanical properties (Geymonat and Pagano, 2003) and damage laws (Périé *et al.*, 2009; Claire *et al.*, 2004; Réthoré, 2010). The availability of full-field measurements for mechanical properties identification has fostered the growth of efficient identification methods, a comprehensive review of which can be found in (Avril *et al.*, 2008).
- **Strain mapping:** DIC has been also used to relate the strain field with microstructural heterogeneities (Gioacchino and Fonseca, 2012; Nicoletto *et al.*, 2011; Fonseca *et al.*, 2005). It has also found numerous applications in biomedical science both in 2D (Bay, 1995; Amini *et al.*, 2013) and 3D (Bay *et al.*, 1999; Benoit *et al.*, 2009; Brémand *et al.*, 2008). Furthermore, due to the availability of whole field strain data, it is possible to pinpoint local phenomena, such as the onset of plasticity (Wu *et al.*, 2011) or crack (Qiu *et al.*, 2008).
- **Validation of theories and simulations:** Constitutive theories and numerical models have been also validated through qualitative and quantitative comparison of experimental and theoretical full-field data. For example, Chevalier *et al.* (2001) used DIC full-field measurements to compare different hyper-elastic models for rubber-like materials. FE simulations can be also validated by DIC measurements (Lomov *et al.*, 2008; Barranger *et al.*, 2010; Guillebaud-Bonnafous *et al.*, 2012). Barranger *et al.* (2010) used DVC-aided validation to conclude that 3D numerical simulations provide more accurate predictions than a 2D plane-stress theory in a cracked specimen loaded in mode I.

CHAPTER 2

OBJECTIVES AND RATIONALE

2.1 Rationale of the thesis

Based on this literature review, the rationale of the project can be explained as follow:

1. Studies such as those of Gioacchino and Fonseca (2012) and Réthoré *et al.* (2013) have shown the useful application of high-resolution full-field measurements for strain mapping and identification applications. This capacity has even greater potentials for DVC to percolate into different areas of research because of the possibility of non-destructive internal measurements. However, limited studies have been devoted to DVC at microstructure level due to the huge amount of calculations accompanying high-resolution 3D measurements (Leclerc *et al.*, 2011).
2. Most studies carried out on the high-resolution DIC have been based on the local approach (Nicoletto *et al.*, 2011; Canal *et al.*, 2012; Gioacchino and Fonseca, 2012). However, several studies (Hild and Roux, 2012; Besnard *et al.*, 2006; Sun *et al.*, 2005; Cheng *et al.*, 2002) have shown that a global framework resulted in lower uncertainties, when compared to the local formulation, due to the fact that it imposes additional relevant constraints on the kinematic basis of correlation problem. This difference becomes more accentuated at high frequency-domain resolutions since the measurement sensitivity is inversely proportional to this resolution (Bornert *et al.*, 2009; Besnard *et al.*, 2006). On the other hand, computational costs for most global strategies become prohibitive when measurements at high resolutions are concerned unless one resorts to parallel computing (Leclerc *et al.*, 2009). In this sense, global approaches reconciling spatial versatility and computational efficiency become very appealing.
3. Within this category, the 2D spectral approach proposed by Wagne *et al.* (2002) has shown great potentials due to its rich kinematic basis as well as low computational costs. However, it worked very well with *periodic* displacement fields and *periodic* images, a situation that rarely occurs in experimental conditions. Further study is required to properly reduce and take account of edge effects as well as to improve the convergence for a broader category of displacement fields.

2.2 Hypothesis

It is believed that proper improvements on the spectral approach will make it reliable and operational for practical cases. Therefore, one can benefit from the low computational costs already demonstrated in the spectral approach.

To evaluate this hypothesis, the improved approach should compete or outperform, in terms of produced errors, when compared to already validated techniques.

2.3 Objectives

The general objective of this research was to develop a global image correlation approach in 2D and 3D, which is both fast and reliable at high resolutions. This work was divided into three specific objectives:

1. **Improvement of the spectral approach**

   The first and fundamental specific objective of this thesis aimed at developing and validating an improved spectral approach based on the following essential modifications and studies:
   - to incorporate a strategy that takes account of non-periodicities in the sought displacement field;
   - to improve on the convergence and accuracy of the approach at high resolutions;
   - to validate the improvements using artificial experiments and by comparison with previous approaches;
   - to investigate the effect of sub-pixel interpolation and texture properties on the accuracy of measurements at high resolution
   - to quantify the noise sensitivity of the developed approach based on texture properties and spatial resolution.

2. **Case study: Application to composites at micro-scale**

   The second specific objective of this thesis was to experimentally explore micro-scale strain heterogeneities in composites arising from the heterogeneous mechanical properties within these materials. This objective, besides verifying the functionality of the improved approach for experimental applications, aimed at supplying a companion thesis work with input data, which focuses on the mechanical properties identification of composite materials. This objective consisted of a case study using both simulated and real experiments from previously published works in the literature.

3. **Extension of the developed approach to 3D**

The third specific objective of this thesis was to extend the improved DIC spectral approach to 3D, thus enabling high-resolution strain measurements from volume images. Finally, potential applications of the developed DVC algorithm on 3D composites at particle scale were investigated using simulated artificial experiments.

2.4 Scientific approach

The core of this thesis is divided into three sections. Each section presents a research article that was prepared during this project in order to complete the objectives stated in Chapter 2. The following describes the contents of each article as well as its context with respect to the three specific objectives.

2.4.1 Article 1: Image-based continuous displacement measurements using an improved spectral approach

This article presents an improved global DIC approach based on the Fourier decomposition of displacement field. The improvements dealt particularly with cases of non-periodic images and non-periodic displacement fields in contrast with the original spectral approach. The developed algorithm was tested using computer-generated experiments. Furthermore, it was fairly compared to the local approach, the results of which confirmed the superiority of the improved spectral approach due to the global framework as well as the high capacity of the method in estimating complex displacements.

The main contributions of this paper are:

- a modified kinematic basis based on the Fourier decomposition, which improves on the previously developed method by its more rapid convergence and lower uncertainty, as well as an analogy providing a more tangible measure of resolution in the spatial domain;
- a prior correction strategy for taking account of non-periodic displacement fields which efficiently reduces the edge effects due to the employed kinematic basis;
- an enhanced algorithm to progressively allow for large number of Fourier modes using proper decision-making criteria within the measurement procedure;
- a validated theoretical framework to quantify the sensitivity of the improved spectral approach to image noise, which establishes a relation between the displacement resolution, noise level and texture properties.

The results obtained in this article suggest new applications of the improved spectral approach to more challenging problems such as composite materials at micro scale.

The revised manuscript of this article was submitted to “Strain” on January 21, 2013, and

was subsequently accepted on January 29, 2013. This journal publishes original contributions on all aspects of experimental solid mechanics. This article was written 90% by the author of this thesis.

2.4.2 Article 2: A global digital image correlation approach to high-resolution full-field strain measurements: Applications to composites at micro-scale

This article explores potential applications of high-resolution reconstruction of full-field displacements and strains in composites using the improved approach developed in the first article. SEM images from the surface of a fiber-reinforced polymer epoxy at micro-scale were taken from the work of Canal *et al.* (2012), who evaluated strain fields using a local DIC approach. Furthermore, the real experiments were simulated using preset displacement fields coming from FE simulation of the exact microstructure, which were artificially applied on the reference SEM images as well as a synthetic image. The simulated experiments, besides feeding the real experiments with suitable input parameters, enabled quantitative assessment of the approach in dealing with full-field measurements in the fiber scale while taking account of noise effects. The main contributions of this paper are:

- a slight variant of the improved spectral approach, which implements a prior multiscale pattern matching based on B-Spline basis functions for the correction of edge effects;
- an investigation on the application of the improved spectral approach for micro-scale strain measurements in composites and its comparison with the previously published data.

The results of this study reveals the possibilities and limits of fiber-scale strain measurements with the improved approach and may further pave the way for bridging the gap between theoretical modeling and real characteristics of composites.

This article was submitted to "Composites Part A" on February 2, 2013. This journal publishes original research dealing with all scientific and technological aspects of composites. This article was written 80% by the author of this thesis.

2.4.3 Article 3: High resolution measurement of internal full-field displacements and strains using global spectral digital volume correlation

This article presents the extension to 3D of the 2D global approach developed in the first paper. Slight modifications with respect to the 2D approach were first discussed, which improved on the algorithm criteria. The functionality of the improved spectral DVC was then validated by several artificial experiments using a priori known displacement fields from numerical simulations of randomly generated composite geometries. Proper imaging resolu-

tion for accurate capturing of strain heterogeneities was estimated as a function of particle size and displacement resolution using the analogy presented in the first paper. The main contribution of this article is the development of an accurate global DVC approach for high-resolution strain measurements inside materials. The developed approach is very promising for 3D measurements thanks to its low computational costs.

This article was submitted to "Optics and Lasers in Engineering" on February 19, 2013. This journal publishes original research on the development and application of optical techniques and laser technology in engineering, including optical metrology, non-destructive testing and new theoretical foundations for experimental methods. This article was written 90% by the author of this thesis.

CHAPTER 3

ARTICLE 1: IMAGE-BASED CONTINUOUS DISPLACEMENT MEASUREMENTS USING AN IMPROVED SPECTRAL APPROACH

F. Mortazavi, M. Lévesque, I. Villemure (2013). Accepted for publication in *Strain* on January 29, 2013.

3.1 Abstract

Digital Image Correlation (DIC) algorithms capable of determining continuous displacement fields are receiving growing attention in the field of mechanical properties identification. In this paper, we develop an Improved Spectral Approach (ISA) to reconstruct continuous displacements based on their Fourier-decomposition. This approach leads to a time- and memory-efficient algorithm thanks to the Fast-Fourier-Transform. Moreover, the Fourier-based decomposition enables accurate heterogeneous measurements. Improvements consist in increasing the accuracy and convergence rate as well as dealing with non-periodic displacements and images. Furthermore, a theoretical framework is presented to quantify the noise sensitivity of the ISA from which useful information are retrieved. The approach is evaluated using synthetic images deformed by heterogeneous displacement fields. Comparisons show that the introduced modifications lead to lower uncertainties by one order of magnitude in the case of non-periodic images and displacement field studied. Moreover, first-order (SO1) and second-order (SO2) subset-based DIC algorithms are compared with the ISA. The comparisons herein reveal that the uncertainties of the ISA are 6-9 times smaller than those of the SO1 due to insufficiency of the first-order shape function for the estimation of heterogeneous displacements, while being slightly smaller than those of the SO2. Moreover, as the image smoothness decreases, the uncertainties of the SO2 deviate from those of the ISA and the exact displacements. The presented approach shows great potentials for challenging applications such as strain measurements at micro-structural levels.

3.2 Introduction

Techniques providing full-field measurements are of particular interest in the field of mechanical properties identification since they provide multiple displacement/strain readings in a single experiment. Among these techniques, Digital Image Correlation (DIC) has been widely used in experimental mechanics. DIC is based on establishing spatial correspondences

between two images acquired from the same test specimen in the unloaded and loaded states. The technique has been used for different purposes from strain mapping in biomedical (Bay, 1995; Hardisty and Whyne, 2009) and materials science applications (Fonseca *et al.*, 2005) to mechanical properties identification (Grédiac, 2004; Geymonat and Pagano, 2003) and damage characterization (Périé *et al.*, 2009; Claire *et al.*, 2004; Qiu *et al.*, 2008).

The earliest approach of DIC in solid mechanics (Sutton *et al.*, 1983), which is still being used for many applications, relies on a point-wise subset-based correlation scheme. Consequently, the corresponding algorithm results in a discrete displacement field. One advantage of this method is that it is computationally efficient since the displacement of each individual point is estimated by correlating small subsets independently. Furthermore, if the level of spatial heterogeneities allows one to limit the degrees of freedom of a subset to rigid body movements, the resulting algorithm may lead to even faster correlations in Fourier domain using Fast Fourier Transform (FFT) (Hild *et al.*, 1999). However, despite further improvements in terms of displacement field models (Vendroux and Knauss, 1998; Lu and Cary, 2000) and data smoothing (Meng *et al.*, 2007; Pan *et al.*, 2006; Wattrisse *et al.*, 2001), aberrant measurements are still likely to occur due to the lack of continuity between adjacent subsets (Sun *et al.*, 2005).

Efforts have been made in the past decade to globally identify displacement fields through minimization of a global dissimilarity criterion (Cheng *et al.*, 2002; Sun *et al.*, 2005; Besnard *et al.*, 2006; Réthoré *et al.*, 2010), which is referred to as global approaches (Hild and Roux, 2012). The global formulation requires the solution of a non-linear least-squares problem (Cheng *et al.*, 2002). This may be eluded by using the optical flow approach along with multiscale iterations (Besnard *et al.*, 2006; Réthoré *et al.*, 2010). However, despite smaller uncertainties (Cheng *et al.*, 2002; Hild and Roux, 2012), at least for the strain (Sun *et al.*, 2005), the non-linear algorithms may require large amount of computer resources to deal with high-resolution displacement measurements, which makes the processing times prohibitive. This limitation can be partly alleviated by taking advantage of sparseness properties of the Jacobian matrix as a result of basis functions with compact support (Cheng *et al.*, 2002; Besnard *et al.*, 2006). Parallel computing was shown to be effective in the case of T3 FE shape functions where displacement fields with very large number of degrees of freedom (DOF) are sought (Leclerc *et al.*, 2009). Alternatively, Proper Generalized Decomposition (PGD) was used to reduce the dimensionality of the correlation problem, hence significantly reducing the computational costs associated to the number of DOF (Passieux and Périé, 2012). The computational savings in the latter, however, are highly dependent on the separability of the sought displacement field (Passieux and Périé, 2012). In this sense, global approaches reconciling spatial flexibility and computational efficiency became very appealing.

A remarkable approach in this category was developed by Wagne *et al.* (2002) who used spectral decomposition to approximate the displacement field. This type of formulation leads to a fast and memory-efficient algorithm using FFT while estimating continuous displacement fields in a more natural way (i.e. reconstructing the displacement Fourier expansion). The computational burden associated to the displacement estimation consists in performing FFT and matrix-vector products in the maximum order of image size. The proposed algorithm successively incorporates higher DOFs in the estimation of the sought displacement by only increasing a cutoff frequency in the formulation of the displacement correction. Thus, more complex displacement fields can be determined without significantly increasing the complexity of the correlation procedure. However, the approach highly relies on periodic displacement fields and periodic images (Wagne *et al.*, 2002); a condition that is rarely met in a real experiment.

In this paper, an Improved Spectral Approach (ISA), within the category of global approaches, is presented with the goal of decreasing the measurement uncertainties as well as making the method operational for non-periodic displacement fields and images, thus benefitting from both accuracy and computational efficiency. Sections Background and Improved spectral approach deal with the mathematical formulation of the improved approach within the framework of a minimization problem while in section Noise sensitivity analysis, the sensitivity of the algorithm in response to noise is investigated using the statistical formulations of error propagation. Sections Evaluations and Results and discussion are devoted to the performance evaluation of the algorithm. Particularly in these sections, the performance of the algorithm is compared to the originally developed spectral approach as well as the first- and second-order subset-based DIC. Finally, further important observations are discussed in section Discussion.

3.3 Notations and conventions

Unless otherwise specified, the notation $\mathbf{A}$ denotes a matrix, whereas $\mathbf{a}$ and a (or A) represent a vector and a scalar, respectively. Also, matrix- or vector-valued functions (fields) appearing in the formulations are denoted by $\mathbf{A}(\mathbf{x})$ or $\mathbf{a}(\mathbf{x})$, respectively, where $\mathbf{x} = (x_1, x_2)$ is the coordinate pair of points in the Euclidean space. In the following sections, images and their derivatives are considered as continuous functions sampled at pixel positions. Therefore, discrete pixel coordinates in the 2D plane are denoted by $\mathbf{x}^{\langle i \rangle}$, where the superscript indicates that the point is associated to the i-th pixel of the image. For an image size of $2L \times 2L$, these are the coordinates of the 2D grid $[0, 2L-1] \times [0, 2L-1]$. The Discrete Fourier Transform

(DFT) of a function and its inverse are given by the following pair of equations:

$$\tilde{a}(\boldsymbol{\omega}^{\langle k\rangle}) = \sum_{i=1}^{N} a(\mathbf{x}^{\langle i\rangle}) \exp\left(-\hat{\imath}\boldsymbol{\omega}^{\langle k\rangle} \cdot \mathbf{x}^{\langle i\rangle}\right) \tag{3.1a}$$

$$a(\mathbf{x}^{\langle i\rangle}) = \frac{1}{N} \sum_{k=1}^{N} \tilde{a}(\boldsymbol{\omega}^{\langle k\rangle}) \exp\left(\hat{\imath}\boldsymbol{\omega}^{\langle k\rangle} \cdot \mathbf{x}^{\langle i\rangle}\right) \tag{3.1b}$$

where $\tilde{a}(\boldsymbol{\omega}^{\langle k\rangle})$ denotes the DFT of $a(\mathbf{x}^{\langle i\rangle})$ and N is the total number of pixels (or alternatively, frequency samples). $\boldsymbol{\omega} = (\omega_1, \omega_2)$ is the pair of radian frequencies (rad/pixel) in the Fourier domain within the square $[-\pi, \pi) \times [-\pi, \pi)$, which is uniformly discretized so that $\boldsymbol{\omega}^{\langle k\rangle}$ refers to the k-th frequency sample, i.e.:

$$\boldsymbol{\omega}^{\langle k\rangle} \in \left\{ \left(\frac{m\pi}{L}, \frac{n\pi}{L} \right) \,\middle|\, -L \leq m, n \leq L-1 \right\} \tag{3.2}$$

Finally, the pointwise operations between two fields (in both domains) are denoted according to the following notation:

$$(a\mathbf{B})(\mathbf{x}) := a(\mathbf{x})\mathbf{B}(\mathbf{x}) \tag{3.3}$$

3.4 Background

3.4.1 General framework of global approaches

Let $f(\mathbf{x})$ and $g(\mathbf{x})$ represent the intensity functions corresponding to the undeformed and deformed images, respectively. In ideal conditions, these two configurations are correlated through a mapping of coordinates, which is expressed by the following relation:

$$f(\mathbf{x}) = g(\breve{\mathbf{x}}) \quad \text{where} \tag{3.4a}$$

$$\breve{\mathbf{x}} = \mathbf{x} + \mathbf{u}(\mathbf{x}) \tag{3.4b}$$

where $\mathbf{u} = (u_1, u_2)$ is the displacement vector as a result of the applied loads. Within the framework proposed by Hild and Roux (2012) for global approaches, the 2D displacement components on the whole Region Of Interest (ROI) are decomposed over a finite set of chosen functions as:

$$u_p(\mathbf{x}) = \sum_{n \in \mathcal{P}} \upsilon_n^{(p)} \psi_n(\mathbf{x}) \quad (p = 1, 2) \tag{3.5}$$

where the sequence $\{\psi_n \,:\, n \in \mathcal{P}\}$ is the set of functions and $\mathcal{P}$ is the set of admissible indices. $\upsilon_n^{(p)}$ are the unknown amplitudes asscociated to the basis functions for the displacement component u_p. The solution to $\boldsymbol{\upsilon}^{(p)}$ is obtained through solving the following global minimization

problem:

$$\min_{\upsilon_n^{(p)}\in\mathbb{C}} \sum_{i=1}^{N} r_i^2\left(\boldsymbol{\upsilon}^{(1,2)}\right), \quad \text{where} \tag{3.6a}$$

$$r_i\left(\boldsymbol{\upsilon}^{(1,2)}\right) := f(\mathbf{x}^{\langle i\rangle}) - g\left(\mathbf{x}^{\langle i\rangle} + \mathbf{u}\left(\mathbf{x}^{\langle i\rangle}; \boldsymbol{\upsilon}^{(1,2)}\right)\right) \tag{3.6b}$$

is called the vector of residuals being a measure of the mismatch between the two configurations. Variables $\upsilon_n^{(p)}$ may take on complex or real values (according to the choice of basis functions). Provided that the displacements to be determined are sufficiently small, one may use the following approximation by linearizing the residuals $r_i\left(\boldsymbol{\upsilon}^{(1,2)}\right)$ using the first-order Taylor expansion with respect to $\upsilon_n^{(p)}$:

$$\begin{aligned} r_i\left(\boldsymbol{\upsilon}^{(1,2)}\right) &\simeq r_i\left(\boldsymbol{\upsilon}^{(1,2)}=\mathbf{0}\right) + \sum_{p=1}^{2}\sum_{n\in\mathcal{P}} \left.\frac{\partial r_i}{\partial \upsilon_n^{(p)}}\right|_{\boldsymbol{\upsilon}^{(1,2)}=\mathbf{0}} \upsilon_n^{(p)} \\ &\simeq (f-g)(\mathbf{x}^{\langle i\rangle}) - \sum_{p=1}^{2}\sum_{n\in\mathcal{P}} \upsilon_n^{(p)} \left(\frac{\partial g}{\partial x_p}\psi_n\right)(\mathbf{x}^{\langle i\rangle}) \end{aligned} \tag{3.7}$$

where the fact that $g\left[\breve{\mathbf{x}}\left(\boldsymbol{\upsilon}^{(1,2)}=\mathbf{0}\right)\right] = g(\mathbf{x})$ has been used in the last line of the equation. Consequently, the first-order optimality condition is approximated as:

$$\sum_{i=1}^{N} r_i \frac{\partial r_i}{\partial \upsilon_n^{(p)}} \simeq -\sum_{i=1}^{N}\left[(f-g)(\mathbf{x}^{\langle i\rangle}) - \sum_{s=1}^{2}\sum_{m\in\mathcal{P}} \upsilon_m^{(s)}\left(\frac{\partial g}{\partial x_s}\psi_m\right)(\mathbf{x}^{\langle i\rangle})\right]\left(\frac{\partial g}{\partial x_p}\psi_n\right)(\mathbf{x}^{\langle i\rangle}) = 0 \tag{3.8}$$

from which the key equation of image correlation is deduced, which reads:

$$\sum_{i=1}^{N}\sum_{q=1}^{2}\sum_{m\in\mathcal{P}} \upsilon_m^{(q)}\left(\frac{\partial g}{\partial x_p}\frac{\partial g}{\partial x_q}\psi_m\psi_n\right)(\mathbf{x}^{\langle i\rangle}) = \sum_{i=1}^{N}\left((f-g)\frac{\partial g}{\partial x_p}\psi_n\right)(\mathbf{x}^{\langle i\rangle}) \tag{3.9}$$

If small displacements are assumed, the solution to the above algebraic system leads to a close estimation of the displacements. The same framework is used in the spectral approach which is explained in the sequel.

3.4.2 Spectral approach

As its name implies, the method relies on the spectral decomposition of the displacement field using the following Fourier basis functions (Wagne *et al.*, 2002; Roux *et al.*, 2002):

$$\psi_n(\mathbf{x}) = \exp\left(\hat{\imath}\boldsymbol{\omega}^{\langle n\rangle}\cdot\mathbf{x}\right) \quad (n=1,2,\cdots,N) \tag{3.10}$$

To ensure consistency with the conventions used in the DFT, let us define $v^{(p)}(\boldsymbol{\omega}^{\langle n\rangle}) = v_n^{(p)}$. Consequently, the spectral decomposition of the displacement field can be written as:

$$u_p(\mathbf{x}) = \sum_{n=1}^{N} \left(H_\kappa v^{(p)}\right)(\boldsymbol{\omega}^{\langle n\rangle}) \exp\left(\hat{\imath}\boldsymbol{\omega}^{\langle n\rangle} \cdot \mathbf{x}\right) \tag{3.11}$$

where the multiplied mask function,

$$H_\kappa(\boldsymbol{\omega}) = \begin{cases} 1 & \|\boldsymbol{\omega}\|_\infty \leq \dfrac{\pi\kappa}{L} < \pi \\ 0 & \text{otherwise} \end{cases}, \tag{3.12}$$

implies that only Fourier terms whose frequencies lie within the square $[-\pi\kappa/L, \pi\kappa/L) \times [-\pi\kappa/L, \pi\kappa/L)$ (κ being the cutoff wavenumber) are used to estimate the displacement components. Figure 3.1 illustrates such a decomposition (depicting only positive frequency samples). Customizing equation (3.9) for the spectral decomposition (5.16) leads to:

$$\sum_{m=1}^{N}\sum_{q=1}^{2} H_\kappa(\boldsymbol{\omega}^{\langle n\rangle}) \left(H_\kappa v^{(q)}\right)(\boldsymbol{\omega}^{\langle m\rangle}) \left(\sum_{i=1}^{N} \left(\frac{\partial g}{\partial x_p}\frac{\partial g}{\partial x_q}\right)(\mathbf{x}^{\langle i\rangle}) \exp\left(\hat{\imath}(\boldsymbol{\omega}^{\langle m\rangle} + \boldsymbol{\omega}^{\langle n\rangle}) \cdot \mathbf{x}^{\langle i\rangle}\right)\right) =$$
$$H_\kappa(\boldsymbol{\omega}^{\langle n\rangle}) \sum_{i=1}^{N} \left((f-g)\frac{\partial g}{\partial x_p}\right)(\mathbf{x}^{\langle i\rangle}) \exp\left(\hat{\imath}\,\boldsymbol{\omega}^{\langle n\rangle} \cdot \mathbf{x}^{\langle i\rangle}\right) \tag{3.13}$$

Comparison of equations (3.1b) and (5.16) reveals that:

$$\left(H_\kappa v^{(q)}\right)(\boldsymbol{\omega}^{\langle m\rangle}) = \frac{1}{N}\tilde{u}_q(\boldsymbol{\omega}^{\langle m\rangle}) \tag{3.14}$$

After substituting equation (3.14) into equation (3.13) and using the definition of DFT, equation (3.13) is simplified to the following form, which is expressed in vector notation using image gradient:

$$\frac{1}{N}\sum_{m=1}^{N} H_\kappa(\boldsymbol{\omega}^{\langle n\rangle})\widetilde{\mathbf{M}}(\boldsymbol{\omega}^{\langle n\rangle} - \boldsymbol{\omega}^{\langle m\rangle}) \cdot \widetilde{\mathbf{u}}(\boldsymbol{\omega}^{\langle m\rangle}) = \widetilde{\left(H_\kappa(f-g)\nabla g\right)}(\boldsymbol{\omega}^{\langle n\rangle}) \tag{3.15}$$

where

$$\mathbf{M}(\mathbf{x}) := \left(\nabla g \nabla g^\intercal\right)(\mathbf{x}) \tag{3.16}$$

and $-\boldsymbol{\omega}^{\langle n\rangle}$ has been replaced by $\boldsymbol{\omega}^{\langle n\rangle}$. One could slightly modify $H_\kappa(\boldsymbol{\omega}^{\langle n\rangle})$ inside the series into $H_\kappa(\boldsymbol{\omega}^{\langle n\rangle} - \boldsymbol{\omega}^{\langle m\rangle})$ provided that $\kappa \ll L$. Thus, the series in the left-hand-side of the

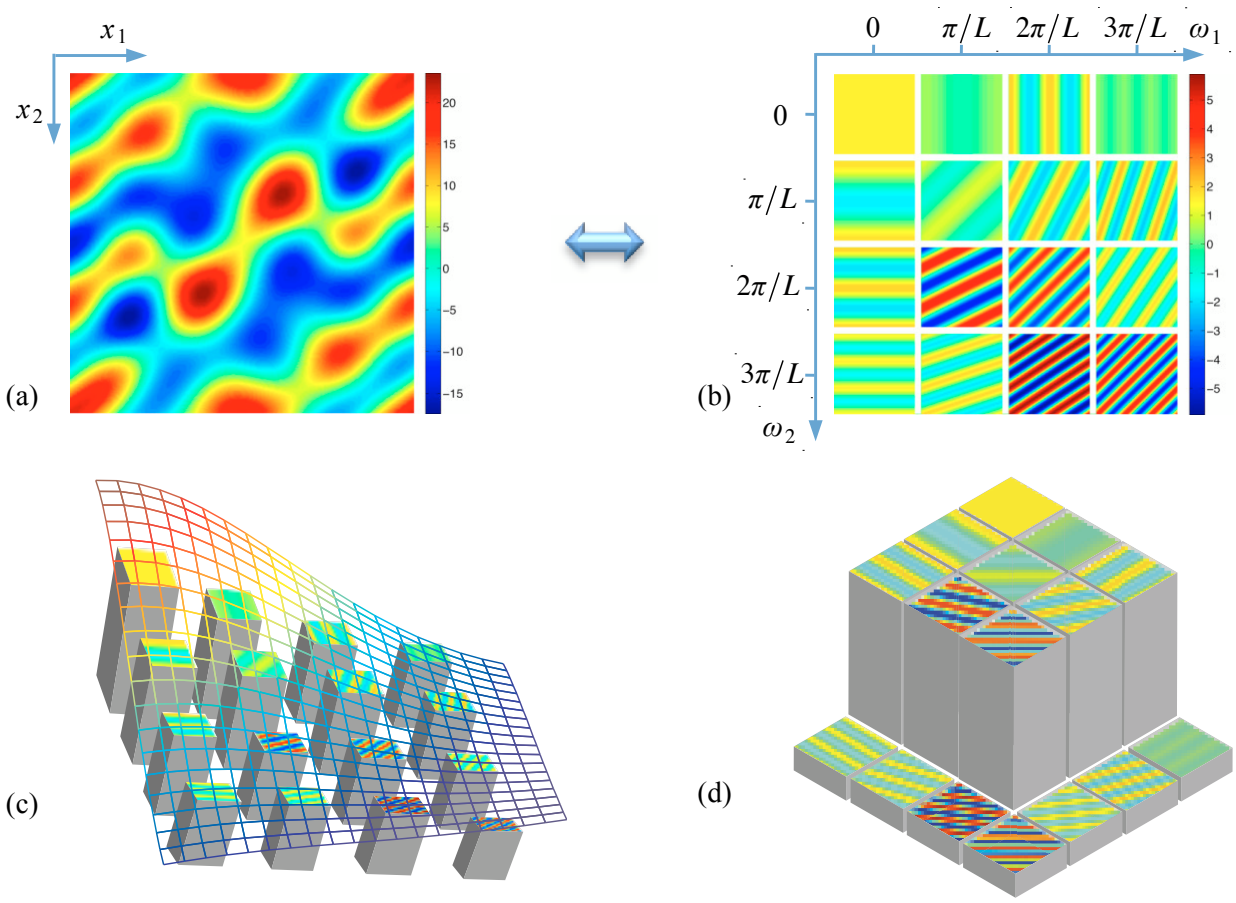

Figure 3.1 Orthogonal decomposition of a displacement field with the spectral approach (a) continuous displacement (b) decomposition over the set of Fourier basis functions (c) Gaussian attenuation of high frequency terms (d) Ideal cutoff of high frequency terms

equation becomes a discrete convolution product, i.e.

$$\frac{1}{N}\left(H_\kappa \widetilde{\mathbf{M}} \star \widetilde{\mathbf{u}}\right)(\boldsymbol{\omega}^{\langle n\rangle}) = \left(H_\kappa \widetilde{(f-g)\nabla g}\right)(\boldsymbol{\omega}^{\langle n\rangle}) \tag{3.17}$$

where $\star$ denotes the discrete convolution product. The main interest of the spectral approach lies in the fact that instead of directly solving the above equation in the frequency domain, one may bring the calculations back to the spatial domain. Thus, the convolution operation turns into a simple matrix product in the real space. In doing so, equation (3.15) is transformed to the following practical form:

$$\left(\widehat{\mathbf{M}} \cdot \mathbf{u}\right)(\mathbf{x}^{\langle i\rangle}) = \left(\widehat{(f-g)\nabla g}\right)(\mathbf{x}^{\langle i\rangle}) \tag{3.18}$$

where $\widehat{(\,)}$ denotes low-pass filtering in the frequency domain using the mask H_κ (i.e. $\hat{f} = \mathrm{DFT}^{-1}\{(H_\kappa \tilde{f})\}$). One faces here a 2×2 linear algebraic system for each point in the space. Such a system is analytically solved giving rise to two explicit expressions for the estimated displacement components. Subsequently, the explicit expressions may be evaluated for all the pixels simultaneously (e.g. using array operations of MATLAB). The main computational burden is performing a forward and a backward DFT to apply the filtering. However, thanks to FFT algorithm, these operations are carried out quite efficiently leading to a fast and memory-efficient algorithm. In practice, equation (3.18) is repeatedly solved while gradually increasing κ so as to progressively enrich the reconstructed displacement field. This is discussed in section Implementation. It is worth noting that the assumption $\kappa \ll L$ (small cutoff wavenumber) is an important requirement to be met. The reason is that the tensor field, $\mathbf{M}(\mathbf{x})$, is a rank-deficient matrix unless it is low-pass filtered by a sufficiently small cutoff wavenumber. This limitation is strongly related to the bandwidth of the image spectrum; an image rich in frequency contents will accept higher cutoff frequencies without $\widehat{\mathbf{M}}$ becoming rank deficient. In other words, an image with a rich texture that carries more information is more capable of reconstructing details of displacements compared to a relatively plain image.

3.5 Improved spectral approach

3.5.1 Gaussian frequency filtering

Obviously, the incorporation of more Fourier terms enriches the displacement model so that it can estimate more complex displacement fields. However, κ can not be boundlessly increased due to the ill-posed nature of the correlation problem. On the other hand, the ideal filtering of high-frequency terms would introduce small oscillations in the displacement hence increasing the uncertainties. Therefore, a modification is introduced herein, which uses a Gaussian low-pass filter instead of the ideal filter so that the amplitudes of the Fourier coefficients are gradually attenuated at high frequencies rather than a sharp cutoff (see Figure 3.1-c and -d). The Gaussian filter is expressed by the following exponential function(Gonzalez and Woods, 2007):

$$H_\kappa(\boldsymbol{\omega}) = \exp\left(-\frac{L^2\|\boldsymbol{\omega}\|^2}{2\pi^2\kappa^2}\right) \tag{3.19}$$

where κ is the cutoff wavenumber corresponding to this type of filtering. Thus, one may expect to involve more Fourier terms, at least partially, when compared to the ideal filter.

3.5.2 Analogy to subset-based DIC

Considering the reciprocal equivalence between the Gaussian masks in the spatial and Fourier domains (Gonzalez and Woods, 2007) written as

$$\kappa_{\text{spatial}} \Longleftrightarrow \frac{1}{\pi}\left(\frac{L}{\kappa_{\text{Fourier}}}\right), \tag{3.20}$$

one may rewrite equation (3.18) using the formulation of filtering in spatial domain (Gonzalez and Woods, 2007). In doing so, the expression for the displacement vector reads:

$$\mathbf{u}(\mathbf{x}) = \left[\sum_{\mathbf{S}\in\mathcal{C}} w_\kappa(\mathbf{S})\Big(\nabla g \nabla g^{\intercal}\Big)(\mathbf{x}+\mathbf{S})\right]^{-1} \cdot \left[\sum_{\mathbf{S}\in\mathcal{C}} w_\kappa(\mathbf{S})\Big((f-g)\nabla g\Big)(\mathbf{x}+\mathbf{S})\right] \tag{3.21}$$

where $w_\kappa(\mathbf{S})$ is the gaussian mask in the spatial domain with the standard deviation of the distribution being κ_{spatial} and $\mathcal{C}$ is the spatial domain within which the filtering is effective. Considering the notion of filtering in spatial domain, the above equation could be hypothetically analogized, in form, to a local approach where the subset size is chosen as to be equal that of $\mathcal{C}$. For instance, for $w_\kappa(\mathbf{S}) = w_0(\mathbf{S}) = 1$, the above equation is similar to the zero-order formulation of the subset-based DIC (Wang *et al.*, 2009) for a single subset. It should be noted, however, that unlike the local approaches, the displacements from the ISA are globally reconstructed. This is justified in equation (3.21) by the fact that the spatial Gaussian mask extends over the entire image area. However, its values effectively vanish at points away from the center point. Therefore, one may roughly estimate an upper bound for the characteristic subset size (denoted by d) as the region within which 99.7% of the mask data lie, i.e

$$d = 6\kappa_{\text{spatial}} = 6 \times \frac{L}{\pi\kappa} = \frac{2L}{1.05\kappa} \tag{3.22}$$

Assuming that the local mean values of the images and their derivatives within subsets do not largely vary from one subset to another, the spatial filtering can be roughly approximated with a weighted sum. From this perspective, another estimation for d could be found as the size of a zero-order weight function that establishes the following equivalence:

$$\sum_{i=1}^{d^2} w_0(\mathbf{x}^{\langle i\rangle}) f(\mathbf{x}^{\langle i\rangle}) = \sum_{i=1}^{N} w_\kappa(\mathbf{x}^{\langle i\rangle}) f(\mathbf{x}^{\langle i\rangle}) \Rightarrow \quad d^2 \times \langle f\rangle = 2\pi\kappa^2_{\text{spatial}} \times \langle f\rangle \tag{3.23}$$

from which the characteristic subset size is obtained as:

$$d = \sqrt{2\pi}\kappa_{\text{spatial}} = \sqrt{2\pi}\frac{L}{\pi\kappa} = \frac{2L}{1.25\kappa} \tag{3.24}$$

where $\langle\,\rangle$ denotes the spatial average (mean value). The above mentioned analogies provide upper and lower bounds for the characteristic subset-set size for a cutoff wavenumber κ, which turns out to be $2L/\alpha\kappa$ ($\alpha \approx 1.05 - 1.25$). The characteristic subset size provides a better understanding of the effect of κ on the spatial domain variables, such as the size of the edge-affected zone (as discussed in Discussion).

3.5.3 Non-periodicity correction

Due to the perodicity of the sinusoidal basis functions, the reconstructed displacements are periodic regardless of whether the original displacement is periodic or not. Consequently, the estimated displacements at the boundaries are likely to contain significant errors. These errors may influence the accuracy of the whole measurement if the original displacement function is highly non-periodic (high discrepancy between function values at opposing boundaries). This restriction can be overcome if one decomposes the sought displacement field into two vector functions (see Figure 3.2); the first part is a non-periodic displacement field with non-zero average strain and the second part is a periodic fluctuation with zero average strain, which can be formulated by its spectral decomposition, i.e.:

$$\mathbf{u}^{(ISA)} = \mathbf{u}^{(D)} + \sum_{n=1}^{N} \big(H_\kappa \mathbf{v}\big)(\boldsymbol{\omega}^{\langle n\rangle}) \exp\big(\hat{\imath}\boldsymbol{\omega}^{\langle n\rangle} \cdot \mathbf{x}\big) \tag{3.25}$$

Using equation (3.25) instead of (5.16) in the correlation process requires that $\mathbf{u}^{(D)}$ is given as the initial solution. Therefore, a two-fold correlation algorithm is required. The first step aims at finding a displacement field with boundary values being a rough estimation of those of the true displacement field. Taking the results of the first step as the initial solution, the second step aims at reconstructing the displacement correction, which is *almost* periodic at boundaries. The first step employs a simple *non-spectral* approach (i.e. with non-periodic assumption for the displacement) whereas the second step uses the spectral algorithm to improve the finer details of the displacement field (see Figure 3.2). The same strategy was used in (Roux *et al.*, 2002) for 1D signals in which a linear displacement field (affine transform) was estimated in the first step. However, considering the intrinsic complexities of displacement fields associated to 2D framework, the affine transform was not used herein. Instead, the adopted strategy employs a point-wise DIC scheme (Vendroux and Knauss, 1998), which results in a discrete displacement field at a coarse mesh of grid points. In order to have a global estimate of the displacement field, a smooth surface is then fitted to the measured data. Since the grid points can not be located on the image borders, the fitting surface may need to be somehow extrapolated to reach the image borders. To this end,

the "gridfit" surface fitting code (D'Errico, 2005) written in MATLAB capable of smoothly extrapolating beyond the convex hull of the measured data was used.

For the first-order Taylor expansion in the global approach to lead to a meaningful estimate, the induced displacements are required to be sufficiently small. Thanks to the rough estimation performed beforehand, the residual displacements are small enough to fulfill this requirement. It should be noted, however, that deviations of $\mathbf{u}^{(D)}$ from the actual displacement field (in the order of a few pixels) are not crucial to the final accuracy of the measured displacement field (3.25) since they will be corrected through the iterative process. The main requirement is that the values of $\mathbf{u}^{(D)}$ at the boundaries mimic roughly the actual displacement values so that the residual fluctuation is almost periodic. Therefore, the input parameters for the local approach leading to $\mathbf{u}^{(D)}$ may be roughly chosen. Typically, a subset size $\simeq d$ (characteristic subset size) would be a wise choice and was used herein. For the evaluations herein, a subset spacing in the range 20-40 pixels led to acceptable results at boundaries. However, smaller (or even larger) step sizes may be better choices for other applications depending on the complexity level of the displacement field. With the selected parameters, the point-wise algorithm allows for a relatively fast measurement procedure. Hence, the whole measurement time is not significantly increased using the adopted strategy.

3.5.4 Further comments

As discussed earlier, the positive definiteness of the dyadic tensor $\widehat{\mathbf{M}}$ is crucial to the continuation of the iterations. When using ideal H_κ mask, it might happen that the smallest eigenvalue of $\widehat{\mathbf{M}}$ becomes negative even for small values of κ, hence hindering the successful progression of the iterations. This is due to the ringing artifacts resulting from the ideal filtering. In such cases, the authors found that slight modifications of the dyadic tensor would help getting around this restriction. Similar to the Hessian modification in the non-linear optimization (Nocedal and Wright, 2000), one may define a positive scalar-valued function $\tau(\mathbf{x})$ so that:

$$\forall \mathbf{x}^{\langle i \rangle}, \quad \mathbf{B}(\mathbf{x}^{\langle i \rangle}) := \widehat{\mathbf{M}}(\mathbf{x}^{\langle i \rangle}) + \tau(\mathbf{x}^{\langle i \rangle})\mathbf{I} \tag{3.26}$$

has always positive eigenvalues. $\mathbf{I}$ is the identity tensor and τ is defined as:

$$\tau(\mathbf{x}^{\langle i \rangle}) = \max\left\{0, \delta_0 - \lambda_1\left(\widehat{\mathbf{M}}(\mathbf{x}^{\langle i \rangle})\right)\right\} \tag{3.27}$$

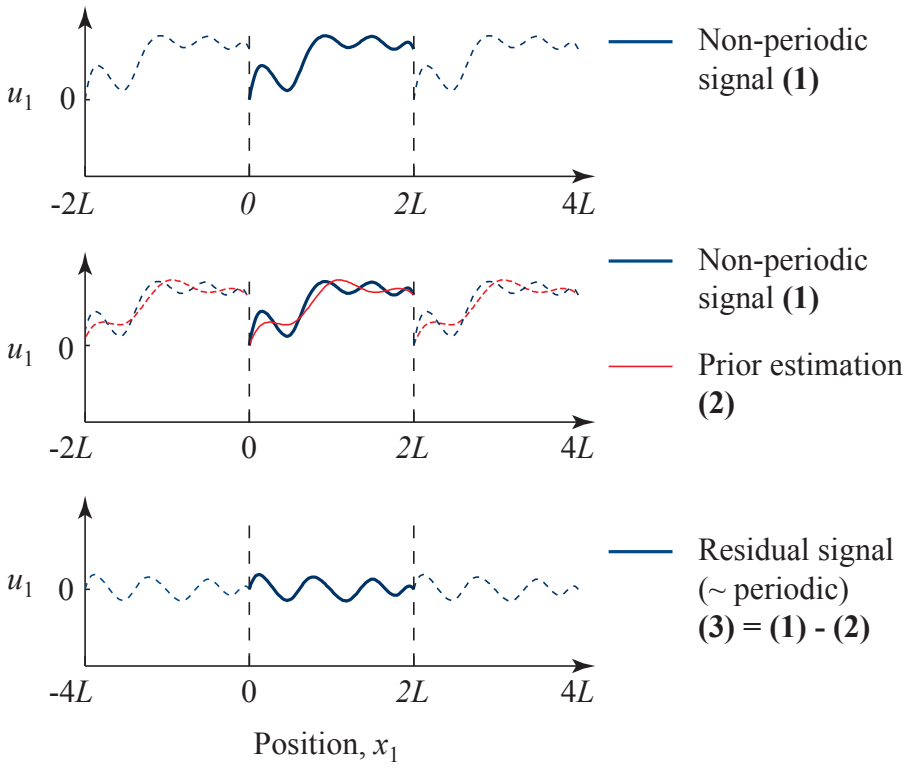

Figure 3.2 Periodization of a non-periodic signal by subtracting a rough estimation of the overall function from the original signal

where δ_0 is a positive real number and λ_1 denotes the smallest eigenvalue of the matrix. Therefore, equation (3.18) is modified into the following equation:

$$(\mathbf{B} \cdot \mathbf{u})\left(\mathbf{x}^{\langle i \rangle}\right) = \left(\widehat{(f-g)\nabla g}\right)\left(\mathbf{x}^{\langle i \rangle}\right) \tag{3.28}$$

Provided that δ_0 is small compared to the average values of λ_1, the resulting displacements are meaningful enough to reduce the objective function (3.6a).

3.5.5 Implementation

The improved spectral approach was implemented in MATLAB software according to the flowchart shown on Figure 3.3. It is worth noting the matrix $\mathbf{M}$ (containing the gradients of g) should be computed at each iteration with the current value of the displacement field. Other alternatives have been proposed in (Besnard *et al.*, 2006; Réthoré *et al.*, 2007) for the evaluation of the image gradients, which were not implemented herein. Two interpolation schemes were used to evaluate g and its derivatives at subpixel locations, namely, bicubic B-spline interpolation (Unser *et al.*, 1993a,b) and bicubic polynomial interpolation (Keys,

1981). The advantage with the latter is the possibility of accelerating the measurements using pre-computed interpolation coefficients look-up table as recommended in (Pan and Li, 2011) for subset-based DIC algorithm.

It should be noted that unlike the original spectral approach (Wagne *et al.*, 2002), no multi-scale iteration scheme is necessary since the major part of the displacements is reconstructed beforehand by the point-wise algorithm. However, to our experience, in order to achieve the best accuracy from the spectral approach, the cutoff wavenumber, κ, should be gradually increased so that it reaches its presumed value at final iterations. In other words, one should first reconstruct the low frequency parts of the displacement prior to finding the high frequency terms. In this regard, it is important to establish a criterion by which the algorithm decides to increase the cutoff wavenumber. The one found to be the most suitable herein is whether the Root Mean Square (RMS) of the change in the residual displacement with respect to the previous iteration gets smaller than a certain threshold, i.e.

$$\text{Criterion C1:} \quad \sqrt{\langle \|\mathbf{u}^{(i)} - \mathbf{u}^{(i-1)}\|^2 \rangle} < \delta_1 \tag{3.29}$$

where $\langle\,\rangle$ denotes averaging over the entire pixels and the superscript (i) corresponds to the iteration number. Using the modification in the previous section, the modified dyadic tensor is always positive definite. However, as the cutoff value increases, equation (3.28) is prone to result in aberrant displacements due to insufficient texture variations with respect to the selected cutoff wavenumber. Therefore, the stopping criterion set in the algorithm to be verified at each iteration is whether the mean value of λ_1 is larger than a positive threshold, i.e.

$$\text{Criterion C2:} \quad \left\langle \lambda_1 \left(\widehat{\mathbf{M}}^{(i)} \right) \right\rangle > \delta_2 \tag{3.30}$$

Also, the reduction of the objective function value at each iteration is controlled. In case where the displacements calculated according to equation (3.28) do not decrease the objective function, the displacements are recalculated using more amplified values for $\tau(\mathbf{x})$ (by increasing δ_0).Therefore, the computed displacements become smaller in magnitude. This process is repeated until either the objective value is reduced with respect to the previous iteration or their relative difference is negligible. The typical values used in the developed algorithm for $\delta_0, \delta_1, \delta_2$ were chosen in the order of 10^{-3} and 10^{-4} and 10^{-2}, respectively.

3.6 Noise sensitivity analysis

Undesirable random oscillations of gray levels are always recorded during image acquisitions due to various experimental reasons, which is referred to as image noise. Consequently,

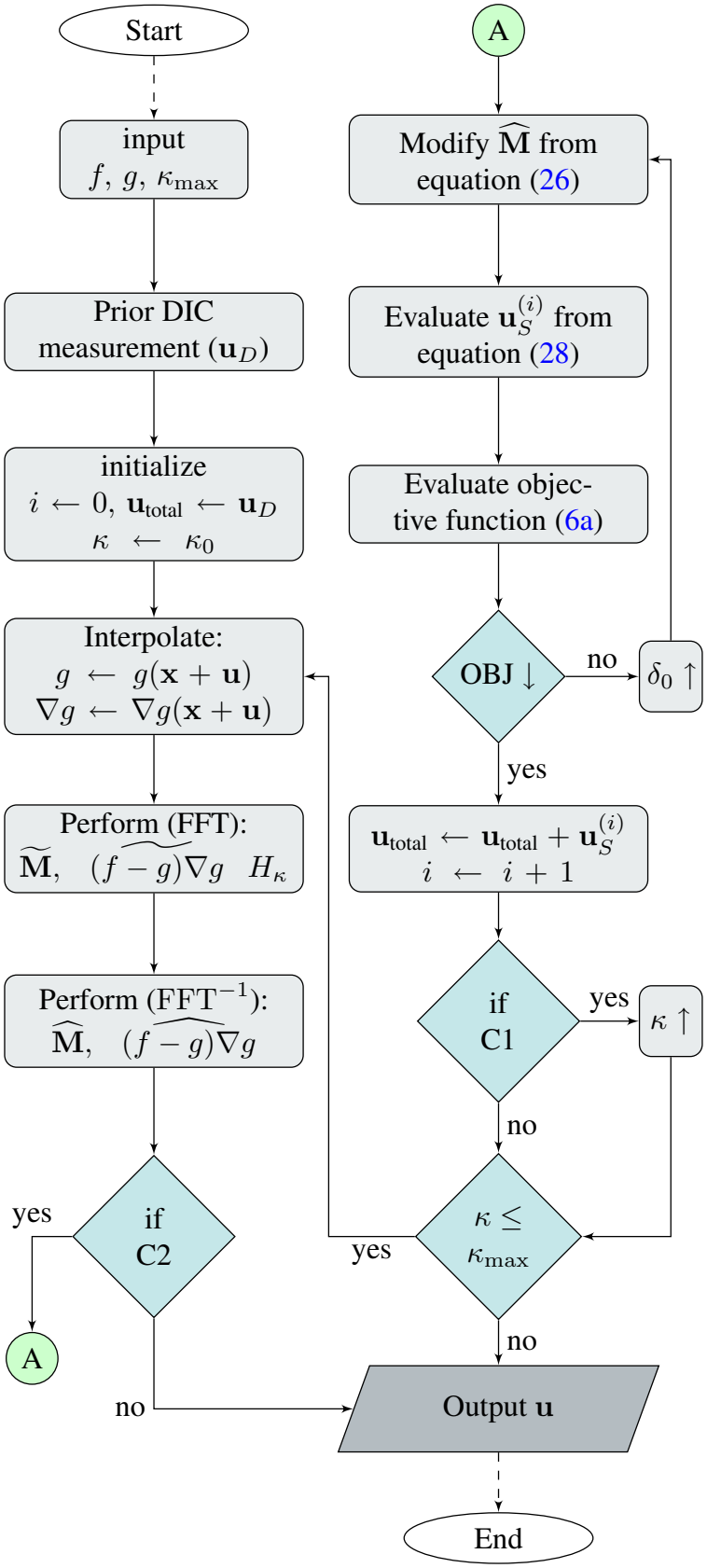

Figure 3.3 The flowchart of improved spectral algorithm implemented in MATLAB software.

uncertainties in the measured data are inevitable. It is therefore necessary to determine the noise sensitivity of the measurement process. Remarkable studies have been done in the past few years to quantify noise-induced errors both in local (Wang *et al.*, 2009) and global approaches (Besnard *et al.*, 2006). Following the same approaches, one may evaluate the sensitivity of the improved spectral approach in response to additive white noise. Let us assume that images f and g are acquired at the same position without the specimen being deformed under load and they are perturbed by a random gaussian white noise with zero mean and a standard deviation σ. As a result, the displacement field measured by the improved spectral approach may be considered as a random process fluctuating around zero (i.e. the true original displacement field). It is possible to relate this deviation to the noise present in the images by following the formulations of error propagation. The mathematical formulations are detailed in Appendix: Derivation of noise sensitivity relation where the RMS of the displacement components is found to be:

$$\mathrm{rms}\,(u_1) \simeq \mathrm{rms}\,(u_2) \simeq \sigma \frac{\kappa}{L} \sqrt{\frac{2\pi}{\langle \|\nabla g\|^2 \rangle}} \tag{3.31}$$

where $\langle \|\nabla g\|^2 \rangle$ is the averaged magnitude of the image gradient over the whole area. Exploring this relation reveals important information about the noise sensitivity of the measurement process. Not surprisingly, the displacement uncertainty is directly proportional to the noise level, that is the higher the noise level, the more noisy the measurements. Moreover, it is understood that the sensitivity of the measurements strongly depends on the texture variations, which is realized by the term in the denominator. Particularly, this means that a higher contrast [1] and an intensity dynamic range provide less noisy measurements. Although the image quantization is not taken into account, the formula shows the effectiveness of a high bit-depth in that clearly more intensity variations could be acquired from the same specimen.

3.7 Evaluations

3.7.1 Simulated experiments

Computer-generated experiments were performed to evaluate the functionality of the algorithm. First, artificial images with random speckle patterns were generated using the

1. It should be noted that the key assumption in deriving all the above formulae is that images are *continuous* functions. Therefore, high contrast images with sharp edges may not necessarily lead to lower uncertainties

following generative function:

$$f(\mathbf{x}) = \sum_{i=1}^{K} \alpha_i \Phi(\mathbf{x} - \mathbf{y}^{\langle i \rangle}; d_i) \tag{3.32}$$

where K is the total number of speckle-like features described by the function $\Phi(\mathbf{x}; d_i)$, d_i is the characteristic size of the i-th speckle and $\mathbf{y}^{\langle i \rangle}$ is the random coordinate vector of the i-th speckle within image area. Two different functions were considered herein for Φ, namely, a Gaussian function and Butterworth function (filter) in 2D producing two artificial images I and II, respectively, as shown on Figure 4.5. The former, produces a smooth variation of intensities while the latter produces more abrupt intensity changes. These functions are explained by the following expressions:

$$\Phi_{\text{Gaussian}}(\mathbf{x}; d) = \exp\left(-\frac{\|\mathbf{x}\|^2}{2d^2}\right) \tag{3.33}$$

$$\Phi_{\text{Butterworth}}(\mathbf{x}; d) = \frac{1}{1 + \left(\frac{\|\mathbf{x}\|}{d}\right)^6} \tag{3.34}$$

The artificial images on Figure 4.5, were generated using $K = 4000$ and $d = 3$ pixels. While the above images are non-periodic, a periodic image III (Figure 4.5c) was also generated using the following function:

$$\widetilde{f}(\boldsymbol{\omega}) = \sum_{i=1}^{K} \alpha_i \exp\left(-\hat{\imath}\boldsymbol{\omega} \cdot \mathbf{y}^{\langle i \rangle}\right) \widetilde{\Phi}_{\text{Gaussian}}(\boldsymbol{\omega}; d_i) \tag{3.35}$$

Where the inverse FFT of the above function creates the periodic image. The intensities have been quantized to 12 bits to minimize uncertainties caused by image quantization. The deformed images were generated by analytically transforming the undeformed image by a preset displacement and hence avoiding the interpolation bias during the image deformation. Finally, the duly provided reference and deformed images were used to measure the displacement field, which was subsequently compared with the accurate preset displacement values to evaluate the measurement uncertainties. Also, full-field strain was calculated from the obtained displacement field and was compared to the exact values. Being highly smooth, the output displacements were not post-processed prior to numerical differentiation while calculating the strains. On this basis, the displacement functions shown on Figure 3.5 were chosen as the preset displacement in x_1 direction. These functions were generated using B-Spline surfaces. The first example, i.e. Figure 3.5(a) is a periodic displacement function with high spatial complexities which was used to deform the periodic image III. This case

was particularly chosen to compare the original and improved spectral approaches. For this example, the displacement magnitude was deliberately reduced to within 1 pixel to avoid the necessity of multi-scale iterations in the original spectral approach. For the same reason, no prior displacement estimation was needed using point-wise DIC in the improved spectral approach. The second example, ie. Figure 3.5(b) is a non-periodic displacement with a complicated strain field ranging up to 7% in the zone of study according to which images I and II were deformed. To eliminate the effects of boundary errors in the evaluations, an 80-pixel bound around the image was excluded from the results.

3.7.2 Subset-based DIC

To compare the improved spectral approach with the subset-based DIC, both first-order (Vendroux and Knauss, 1998) and second-order (Lu and Cary, 2000) DIC approaches were implemented in MATLAB. The normalized similarity criterion being invariant to linear change of illumination was minimized using Levenberg-Marquardt algorithm. A reliability-guided displacement scanning scheme (Pan, 2009) was implemented to provide initial solutions for the measurement of individual subsets. As for the sub-pixel registration algorithms, the same interpolation schemes as in the improved spectral approach were used in the evaluations, namely, bicubic B-splines and bicubic polynomial interpolations. Pre-computed interpolation coefficient look-up table was used in the case of bicubic polynomial interpolation as recommended in (Pan and Li, 2011). For the bicubic B-spline algorithm, however, the authors did not find a way to make the interpolation scheme faster.

3.8 Results

3.8.1 Comparison with the original spectral approach

Case of periodic image with periodic displacement

The pair of image III and its corresponding deformed image transformed according the periodic displacement field, Figure 3.5(a), was used in this section as the periodic example.Figure 3.6(a) shows the decreasing trend of RMS error of the measured displacement as a function of iterations for both approaches. Same criteria were used in both cases to increase the cutoff wavenumber as well as to stop the iterations. Obviously, the improved spectral approach with Gaussian filtering has revealed a significantly superior convergence trend when compared to the original spectral approach with ideal filtering. This is due to the fact that a wider range of Fourier terms are incorporated in the measurement when the Gaussian function is used. It is worth mentioning that modifying the dyadic matrix $\widehat{\mathbf{M}}$ de-

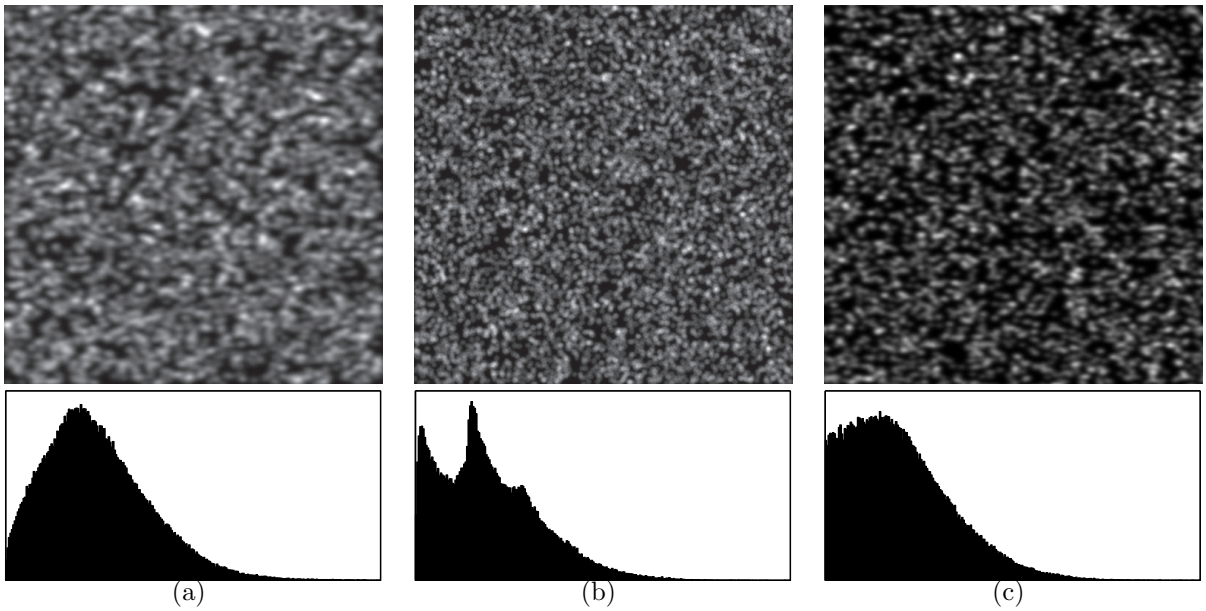

Figure 3.4 Artificially-generated images for evaluation purposes and their histograms denoted in the text by (a) Image I, (b) Image II and (c) Image III (all images are 512×512 pixel 12-bit gray-scale). Image III is periodic.

vised in section Further comments turned out to be essential in the case of original spectral approach with ideal filter. Without such a modification, increasing the ideal cutoff beyond certain low limits would have led to the indefiniteness of the dyadic product at some points making iterations impossible to continue. Table 3.1 shows the final uncertainties of both cases calculated for displacement components as well as the normal strain ε_{xx}. As seen from the table, both approaches led to close estimations of the displacements/strain. The reduced number of iterations (by $\approx 50\%$) in the improved approach exemplifies its rapid convergence when compared to its forerunner. The slight superiority of the original approach in u_2 and ε_{xx} is due to the "lossless" performance of the ideal filter in passing the entirety of the amplitudes within the cutoff frequency in contrast with the smoothing Gaussian filter (Gonzalez and Woods, 2007). However, this ideal characteristic does not operate in practical situations as explained in the next results.

Case of non-periodic image with non-periodic displacement

The pair of image I and its corresponding deformed image transformed according the non-periodic displacement field, Figure 3.5(b), was used in this section as a non-periodic example. It should be mentioned that the original spectral approach as such was not used herein since it could not deal with non-periodic displacements. Therefore, the prior displacement rough

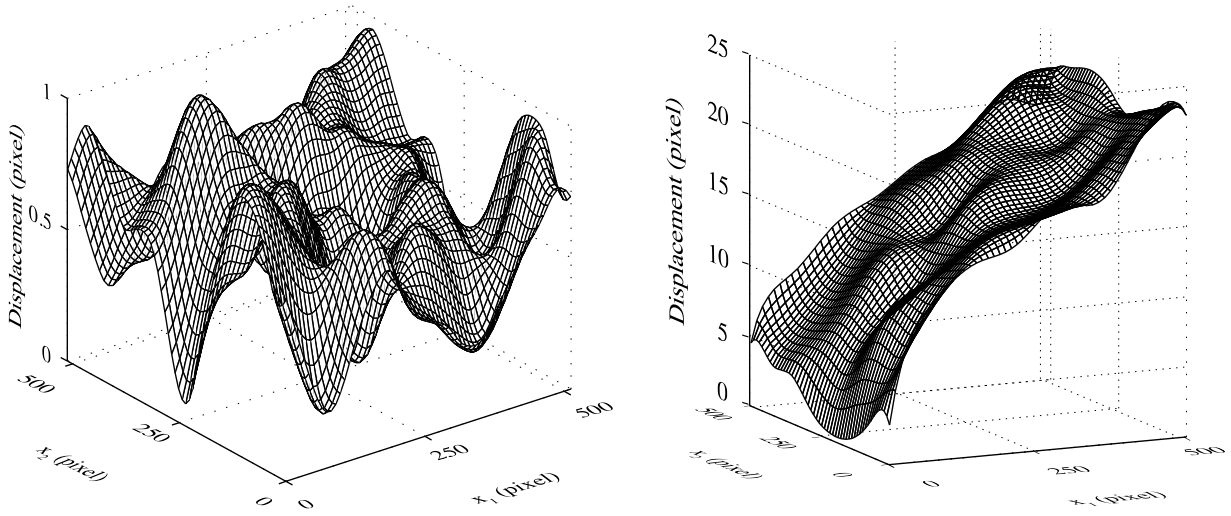

(a) (b)

Figure 3.5 Preset horizontal displacements for the evaluated examples; (a) periodic and (b) non-periodic displacements.

Table 3.1 Measurement uncertainties for the case with periodic image III and periodic displacement. Comparison between the improved and the original spectral approaches (abbreviated as ISA and SA, respectively.).

	RMS error			No. iterations	κ_{Final}
	u_1 (px)	u_2 (px)	ε_{xx} (px/px)		
ISA	1.5×10^{-4}	1.1×10^{-4}	5.3×10^{-5}	71	45
SA	1.6×10^{-4}	9.6×10^{-5}	3.4×10^{-5}	140	60

Table 3.2 Measurement uncertainties for the case with non-periodic image I and non-periodic displacement. Comparison between the improved and the original spectral approaches (abbreviated as ISA and SA, respectively.).

	RMS error			No. iterations	κ_{Final}
	u_1 (px)	u_2 (px)	ε_{xx} (px/px)		
ISA	5.1×10^{-4}	3.0×10^{-4}	9.1×10^{-5}	56	19
SA	7.6×10^{-3}	4.1×10^{-3}	9.9×10^{-4}	98	20

estimation as in the improved approach was also implemented in this algorithm and hence no more multi-scale iterations scheme was used. As shown on Figure 3.6(b), a similar trend to

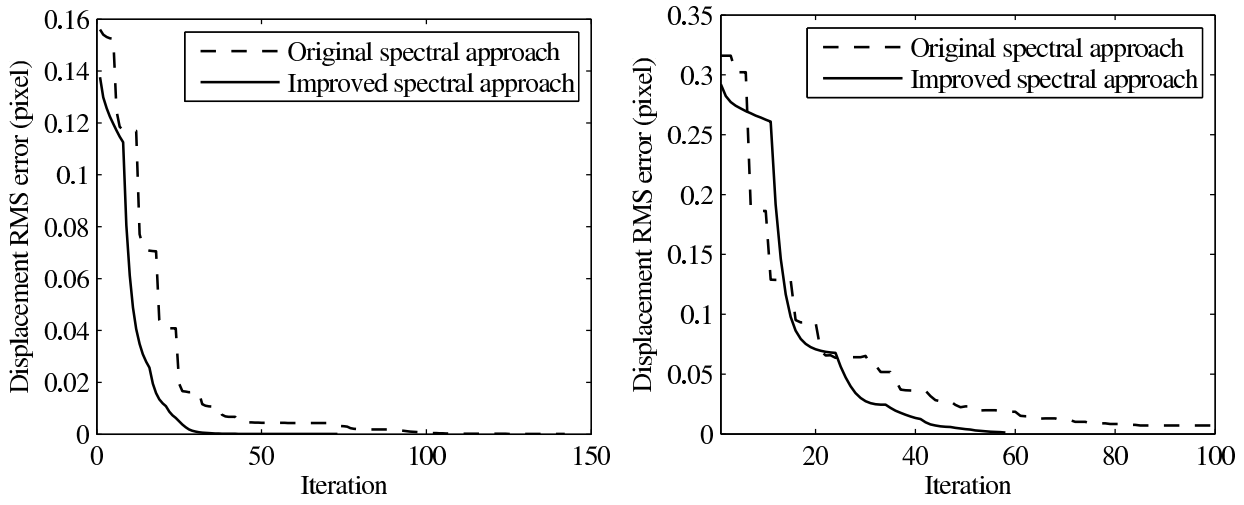

(a) (b)

Figure 3.6 RMS error of the measurement as a function of iterations for the case of (a) periodic image-periodic displacement and (b) non-periodic image-non-periodic displacement.

the previous case was observed for the non-periodic example. However, the continuation of iterations for the original spectral approach beyond the limit shown on the figure turned out to have detrimental effects on the accuracy of the measurements as well as the minimization of the objective function as evaluated by the algorithm. This effect is due the presence of "ringing artifacts" near the borders of the non-periodic image and its gradients when filtered using the ideal filter, which propagate and turn into measurement errors in the ZOI as the iterations progress. In contrast, no such effect was observed in the improved spectral approach since the Gaussian filter eliminates ringing artifacts. Therefore, the measurement uncertainties in the improved spectral approach were much lower for non-periodic example as shown in Table 3.2

3.8.2 Comparison with subset-based DIC

For subset-based measurements, one of the key factors in achieving the maximum accuracy is determining the optimum subset size, which is a function of several parameters such as image characteristics, order of subset transform function, displacement complexities as well as sub-pixel interpolation scheme. For the four combinations studied herein, i.e. first- and second-order subsets with two different interpolation schemes, a priori studies were performed first on images I and II to obtain the optimum subset size. Figure 3.7 shows the results of different evaluations as a function of subset size. A step size (i.e. the distance between adjacent subsets) of 4 pixels was used to measure the discrete displacement data. Based

on the obtained subset sizes, DIC measurements were performed, the results of which are summarized in Table 3.3. The table presents also the results obtained from the improved spectral approach using two different interpolation schemes. As seen from the table, the ISA provided considerably better results for both images as compared to the first-order subset-based DIC. The second order DIC, however, showed comparable performance to the improved spectral approach, which was far better than the first-order DIC. This means that special care should be taken when choosing the first-order DIC algorithm for applications with high spatial complexities in displacement field. Figure 3.8 illustrates the resulting error maps of the three approaches. The continuous error map in the improved spectral approach partly explains its superiority to the discrete DIC method. Another advantage is its high flexibility in fittig to displacement fields with high complexities.

3.8.3 Effect of noise

In the first experiment, image II was duplicated to account for its corresponding deformed image (zero deformation). The created image pair was then polluted with two random white gaussian noises with the same level before 12-bit quantization. This experiment is usually performed in laboratories (Smith *et al.*, 1998) by acquiring images twice from a specimen in the unloaded state. Figure 3.9 shows the RMS of the calculated displacement using the improved spectral approach as a function of additive noise level and the gaussian cutoff wavenumber. The results are also compared to the theoretical prediction of the noise sensitivity presented in equation (3.31). As shown on the figure, the results from the theoretical formula are in good agreement with the simulated measurements.

In the second experiment, the pair of image II and its corresponding deformed image used in the previous section was polluted with two random noises before quantization. The experimental input data were analyzed with ISACS and SO2CS algorithms while varying the noise level in different runs. These results are presented in Figure 3.10. The same trend is observed as in the previous section while comparing the accuracies of both algorithms. The theoretical predictions are also plotted in the same figure to validate the functionality of the mathematical relation in the studied example. It should be noted that the theoretical results are shifted up so as to match to the uncertainties by ISACS at zero noise level. This was because the theoretical prediction does not take into account the interpolation bias being present even in the absence of noise. The comparison reveals that the theoretical relation performs relatively well as an a priori measure at low noise levels. At higher noise levels, however, the uncertainties caused by interpolation bias make the noise-induced uncertainties diverge from the theoretical predictions as can be seen for the noise level of 8.

Table 3.3 Comparison of the performances of the improved spectral approach and the subset-based DIC for images I and II.

Algorithm	cutoff wavenumber	subset size (pixels)	RMS error		
			u_1 (10^{-3} pixel)	u_2 (10^{-3} pixel)	ε_{xx} (10^{-4} $\frac{\text{pixel}}{\text{pixel}}$)
		Image I			
ISACP	14	29-35†	0.78	0.35	1.2
ISACS	19	21-25†	0.51	0.3	0.91
SO1CP	N.A.	9	3.7	2.4	6.8
SO1CS	N.A.	9	3.3	2.3	5.9
SO2CP	N.A.	21	1.3	0.6	2.7
SO2CS	N.A.	21	0.84	0.46	2.2
		Image II			
ISACP	6	65-79†	3.2	0.54	3.1
ISACS	10	41-49†	0.68	0.23	0.93
SO1CP	N.A.	13	7.5	2.6	10
SO1CS	N.A.	9	3.4	2.1	5.5
SO2CP	N.A.	37	4.0	1.3	4.9
SO2CS	N.A.	25	1.2	0.6	2.5

LEGEND: † Characteristic subset size calculated by equations (3.22) and (3.24)

ISAXX: Improved Spectral Approach (XX interpolation) SOxXX: Subset-based DIC of Order x (XX interpolation)

CS: Cubic B-Spline interpolation (Unser *et al.*, 1993a,b) CP: Cubic Polynomial interpolation (Keys, 1981)

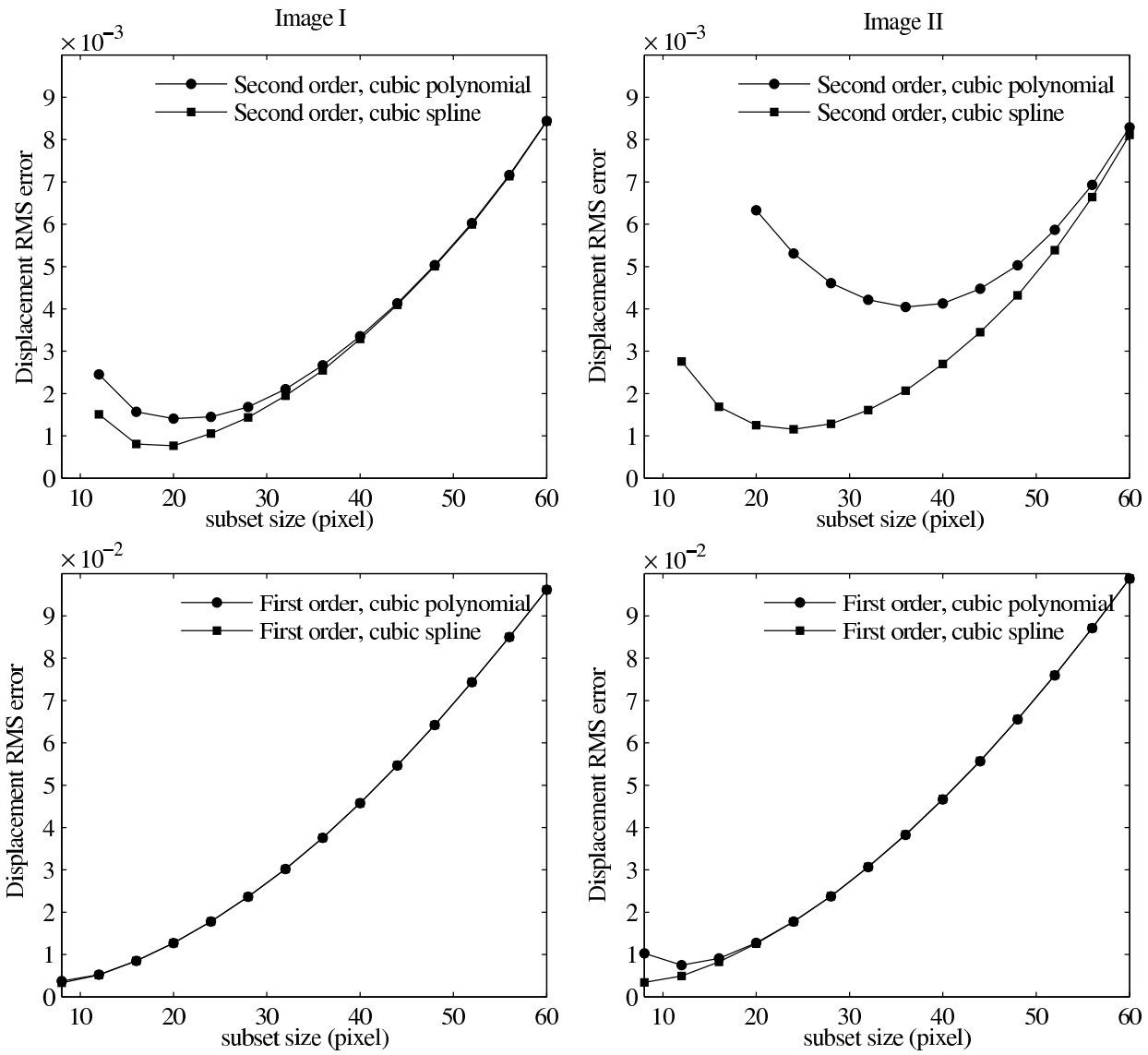

Figure 3.7 A priori study on the selection of optimum subset size in the subset-based method. Four combinations were considered for each image as shown above.

3.9 Discussion

Figs. 3.6 and 3.9 recall two divergent trends in measurement error with respect to the cutoff wavenumber. In the former, the measurement RMS error decreases with κ increasing, whereas increasing κ is shown in the latter to have detrimental effects on the noise-induced uncertainty of the measurements. These effects, which have been also observed by other authors (Bornert *et al.*, 2009) (for the interpolation bias instead of noise), are the results of two different uncertainty sources, namely, under-estimation of displacement heterogeneities

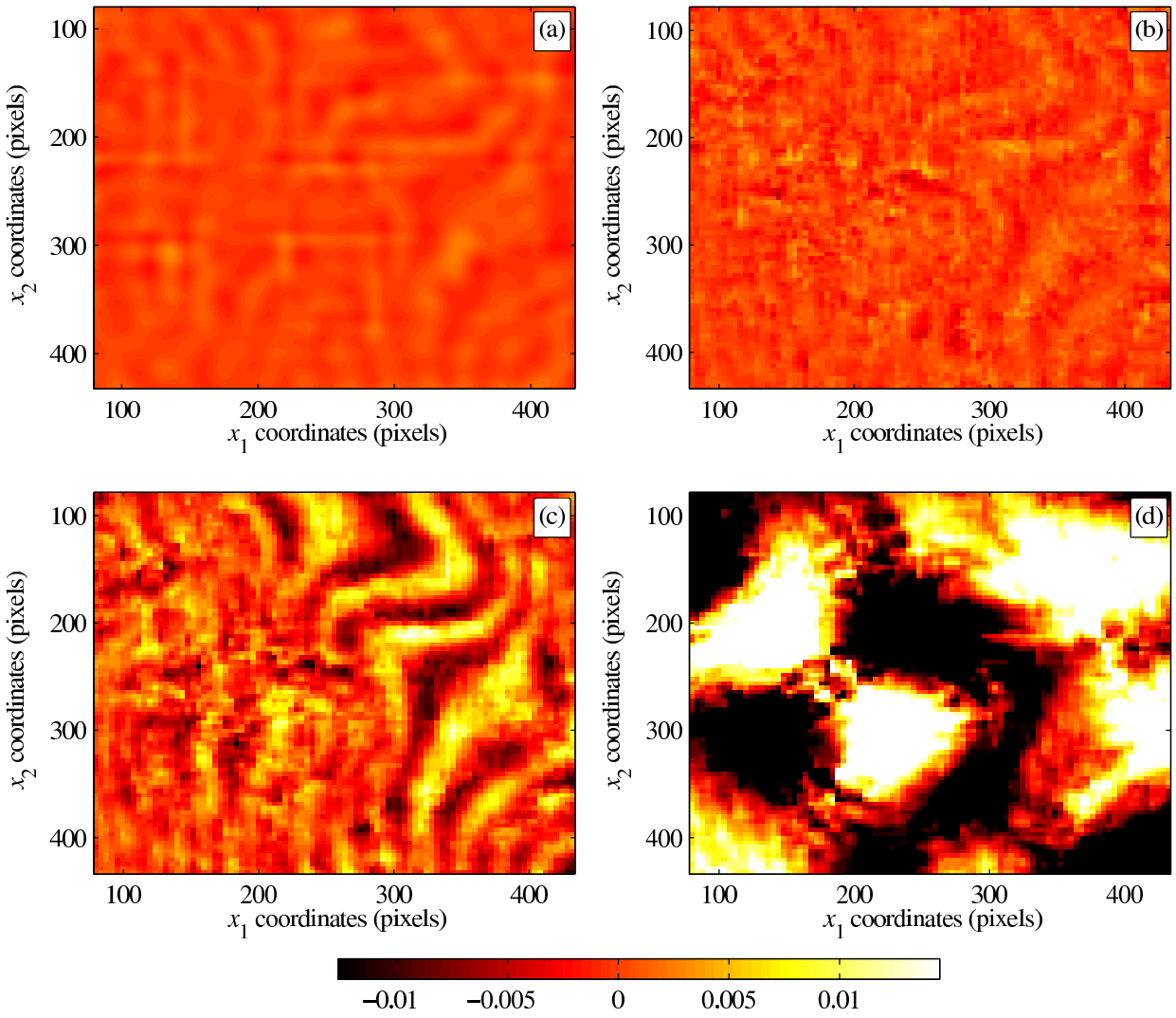

Figure 3.8 Error map of the u_1 displacement measured from pair of image II for (a) ISACS, (b) SO2CS, (c) SO2CP and (d) SO1CP

and intensity fluctuations. In practice, it is at the discretion of the operator to determine an optimum value of κ for which a compromise is achieved between estimating a displacement field rich in details and keeping the noise-induced uncertainties (as well as interpolation bias) at low levels. Such decisions, besides the information about the noise level, would also require some a priori knowledge about the overall complexity of the displacement field (e.g. through finite element analysis). In that case, it is possible to determine the optimal parameters by performing simulated experiments similar to those presented in this paper.

Comparing the results presented in Table 3.3 for images I and II, one notices smaller uncertainties in measurements obtained from image I. This is justified by the smooth intensity

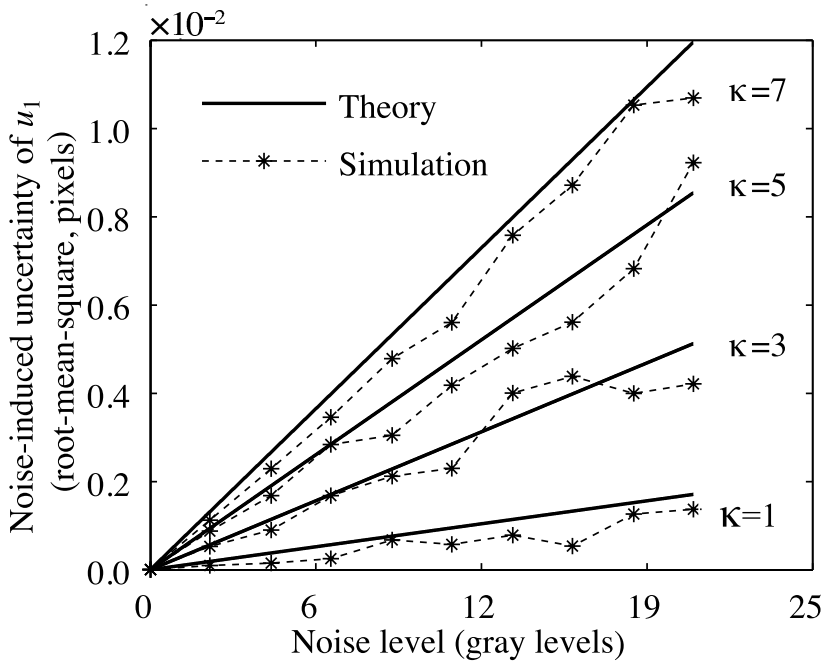

Figure 3.9 Sensitivity of the ISACS algorithm in response to additive Gaussian white noise

variations in this case, which leads to smaller interpolation bias (Schreier *et al.*, 2000). It is also that the results by the improved spectral approach are less affected by the non-smooth intensity changes in Image II as compared to the subset-based DIC. This is due to the global framework of the approach as opposed to the subset-based DIC where the deformation of each subset is treated individually from other regions. One last observation to be made in this table is the effect of sub-pixel interpolation. As observed by other researchers (Schreier *et al.*, 2000), the errors produced by the cubic B-Spline interpolation are generally less than those from cubic polynomial interpolation. Moreover, as the image roughness increases, this difference becomes even more important. It would then be recommended to use cubic B-Spline interpolation for reliable measurements despite its additional computational burden when compared to bicubic polynomial interpolation. However, the subset-based DIC algorithm with B-Spline interpolation takes much longer time than the one developed in (Pan and Li, 2011) due to impossibility of setting pre-computed coefficients lookup table. From this point of view, the use of improved spectral approach is more efficient in the sense that the sub-pixel interpolation is performed globally on the whole image area and once per iteration whereas in the subset-based DIC, interpolation is repeatedly performed on the overlapping areas in adjacent subsets making the measurement time unavoidably long.

Table 3.3 lists also the characteristic subset sizes for the ISAXX algorithms using the analogy presented in section Analogy to subset-based DIC. As seen from these values, the

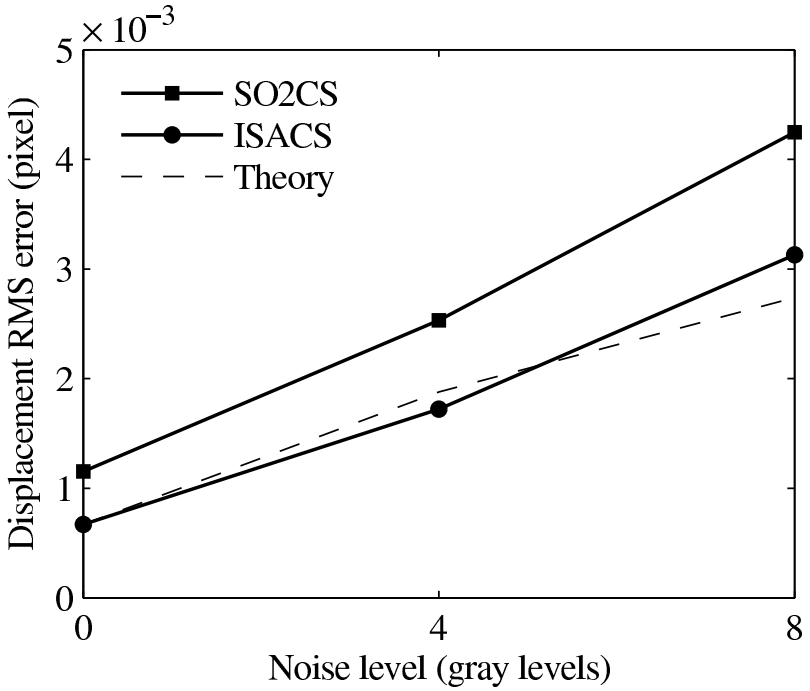

Figure 3.10 Comparison of noise-induced uncertainties of ISACS and SO2CS as functions of noise level. Note that the theoretical sensitivity relation perform relatively well compared to the ISACS algorithm.

characteristic subset sizes are larger than those of the subset-based algorithms, which implies that the improved spectral approach is capable of incorporating a wider area of variating intensities from the surrounding regions (at least partially) during a matching process, while having more flexibility than the subset-based DIC. Hence, the resulting error map (Figure 3.8a) is spatially correlated to a large extent with lower interpolation bias than those shown on Figure 3.8(b)-(d). These observations highlight the advantage of a global framework for solving a DIC problem. The same analogy could also be employed to define a rough estimation of the width of the zone near the borders within which the spectral algorithm returns unreliable measurements. In the spatial domain, this corresponds to the region where the equivalent spatial filtering yields inaccurate results due to the non-periodicity of the image, namely, the half-width of the characteristic subset (Gonzalez and Woods, 2007). For a cutoff wavenumber κ, this value is $L/1.05\kappa$.

Comparing the curves corresponding to SO2CS and ISACS on Figure 3.10, one notices almost the same line slopes with a shift in SO2CS with respect to ISACS. This is due to the fact that the noise sensitivity is inversely proportional to the image gradients in all gradient-based image correlation approaches (Wang *et al.*, 2009; Hild and Roux, 2012), which was verified again herein by equation (3.31). Finally, the theoretical noise-induced uncertainty,

could also be used to estimate the inherent level of uncertainty in the measured data, which is not reduced by enriching the displacement field. Particularly, such an a priori measure can be used to modify the algorithm decision criteria, such that for an experiment with higher estimated noise level, the algorithm automatically ends the reconstruction process at a lower cutoff wavenumber in order to avoid detrimental effects of increasing κ on the accuracy of noise-sensitive measurements.

3.10 Conclusion

An improved approach was presented to estimate continuous displacement fields from digital images based on the Fourier decomposition of displacement field. The improvements dealt particularly with cases with non-periodic images and non-periodic displacement fields in contrast with the original spectral approach. The developed algorithm was tested using computer-generated experiments. The evaluations showed that the improved spectral approach was capable of reconstructing spatially heterogeneous displacement fields while being computationally efficient. Particularly, comparisons with the original approach revealed that the improvements reduced the measurement errors by one order of magnitude in the non-periodic example. In the periodic example, the uncertainties of both approaches were very close. However, the improved spectral approach resulted in a more rapid convergence rate ($\approx$twice as fast) thanks to the partial incorporation of high frequency terms as a result of using the Gaussian mask. Furthermore, the implementation of the displacement rough estimation prior to reconstruction by the improved spectral approach was shown to make the whole approach operational for non-periodic displacements, which would not have been achieved had the spectral approach been merely used. In the second step of experiments, the improved spectral approach was compared with both first- and second-order subset-based DIC approaches with algorithms adopted from the recent literature. A priori studies were performed first to obtain the optimum parameters such as subset size providing the least possible displacement uncertainties. Comparisons showed that the uncertainties of the second-order DIC were much closer, though higher in general, to the improved spectral approach than the first-order DIC. The latter led to measurement errors 6-9 times larger than the improved spectral approach due to the complexity of the displacement field considered in this study. Furthermore, the effect of image smoothness on the performance of approaches was studied using two types of synthetic images with different levels of intensity variations. The evaluation showed that in the case of smooth image, the uncertainties of second-order DIC and the spectral approach were very close whereas for the non-smooth image, the uncertainties in the second-order subset-based algorithm were twice larger. This superiority of the improved

spectral approach is due to the global framework as well as the high capacity of the method in estimating complex displacements. Furthermore, thanks to the FFT-based iterations, the computations become less cumbersome and easy to handle by a regular PC.

Finally, a theoretical framework was presented to quantify the sensitivity of the improved spectral approach to image noise. The theoretical formula showed that the displacement uncertainty (standard deviation) was linearly related to the noise level as well as the cutoff wavenumber (for the specific assumptions made herein). Also, the theoretical analysis suggested that a high contrast image would lead to less noise in the measured displacements. These results were also verified by comparing the theoretical sensitivity predictions with the measurements from duly provided images from a simulated experiment.

The results obtained in this study suggest new applications of the improved spectral approach to more challenging problems such as composite materials at micro scale. This is one of the ongoing works by the authors and will be addressed in another publication.

3.11 Acknowledgements

This research was funded by Fonds Québécois de la Recherche sur la Nature et les Technologies (FQRNT)-projets de recherche en équipe and the Canada Research Chair program (M. Lévesque and I. Villemure).

3.12 Appendix: Derivation of noise sensitivity relation

Let $\mathbf{v}(\mathbf{x}^{\langle m \rangle})$ be a discrete vector field whose values at each point are random variables. The covariance between vector values at different points may be expressed as a multi-dimensional array whose elements, are covariance matrices of two corresponding vectors. Let the matrix $\mathbf{\Gamma}^{\mathbf{v}}_{mn}$ be the (m, n) entry of this array, which is calculated as:

$$\mathbf{\Gamma}^{\mathbf{v}}_{m,n} = \mathbf{E}\left[\mathbf{v}(\mathbf{x}^{\langle m \rangle}) \cdot \mathbf{v}^{\intercal}(\mathbf{x}^{\langle n \rangle})\right] - \mathbf{E}\left[\mathbf{v}(\mathbf{x}^{\langle m \rangle})\right] \cdot \mathbf{E}\left[\mathbf{v}(\mathbf{x}^{\langle n \rangle})\right]^{\intercal} \tag{3.36}$$

where $\mathbf{E}[\,]$ denotes the mathematical expectation (should not be confused with spatial average which is denoted by $\langle\,\rangle$ herein). Now, if that random vector is involved in a linear field equation such as:

$$\sum_{m} \left[\mathbf{A}(\mathbf{x}^{\langle i \rangle}, \mathbf{x}^{\langle m \rangle}) \cdot \mathbf{v}(\mathbf{x}^{\langle m \rangle})\right] = \mathbf{b}(\mathbf{x}^{\langle i \rangle}) \tag{3.37}$$

then it is possible to evaluate the propagation of uncertainties of $\mathbf{v}$ into $\mathbf{b}$ by calculating the aforementioned covariance matrices of both sides, which leads to the following relation:

$$\sum_{m,n} \mathbf{A}(\mathbf{x}^{\langle i\rangle}, \mathbf{x}^{\langle m\rangle}) \cdot \mathbf{\Gamma}^{\mathbf{v}}_{m,n} \cdot \mathbf{A}^{\intercal}(\mathbf{x}^{\langle j\rangle}, \mathbf{x}^{\langle n\rangle}) = \mathbf{\Gamma}^{\mathbf{b}}_{i,j} \tag{3.38}$$

where it is supposed that entries of $\mathbf{A}$ are not random variables. The above equations are applicable in both spatial and Fourier domains (in which case $\mathbf{x}^{\langle i\rangle}$ is replaced with $\boldsymbol{\omega}^{\langle i\rangle}$). Also, using the definition in equation (3.36) as well as that of the DFT, the covariance matrices in the spatial domain can be related to those of Fourier domain as follows:

$$\mathbf{\Gamma}^{\widetilde{\mathbf{v}}}_{m,n} = \sum_{i=1}^{N}\sum_{j=1}^{N} \mathbf{\Gamma}^{\mathbf{v}}_{i,j} \exp\left(-\hat{\imath}(\boldsymbol{\omega}^{\langle m\rangle} \cdot \mathbf{x}^{\langle i\rangle} + \boldsymbol{\omega}^{\langle n\rangle} \cdot \mathbf{x}^{\langle j\rangle})\right) \tag{3.39}$$

$$\mathbf{\Gamma}^{\mathbf{v}}_{i,j} = \frac{1}{N^2} \times \sum_{m=1}^{N}\sum_{n=1}^{N} \mathbf{\Gamma}^{\widetilde{\mathbf{v}}}_{m,n} \exp\left(\hat{\imath}(\boldsymbol{\omega}^{\langle m\rangle} \cdot \mathbf{x}^{\langle i\rangle} + \boldsymbol{\omega}^{\langle n\rangle} \cdot \mathbf{x}^{\langle j\rangle})\right) \tag{3.40}$$

Now assume that the random vector field $\mathbf{v}(\mathbf{x}^{\langle i\rangle})$ is a result of scaling a deterministic vector field $\mathbf{w}(\mathbf{x}^{\langle i\rangle})$ by a random distribution $\epsilon(\mathbf{x}^{\langle i\rangle})$, i.e. $\mathbf{v}(\mathbf{x}^{\langle i\rangle}) = (\epsilon\mathbf{w})(\mathbf{x}^{\langle i\rangle})$. If the random distribution is an uncorrelated stationary random process with a mean value μ and a covariance

$$\mathbf{\Gamma}^{\epsilon}_{i,j} = \sigma^2 \delta_{ij}, \tag{3.41}$$

where δ_{ij} denotes the kronecker delta and σ^2 is the variance of the random variables, the expression for $\mathbf{\Gamma}^{\widetilde{\mathbf{v}}}_{m,n}$ simplifies to

$$\begin{aligned}\mathbf{\Gamma}^{\widetilde{\mathbf{v}}}_{m,n} &= \sigma^2 \sum_{i=1}^{N} \Big(\mathbf{w} \cdot \mathbf{w}^{\intercal}\Big)(\mathbf{x}^{\langle i\rangle}) \exp\left(-\hat{\imath}(\boldsymbol{\omega}^{\langle m\rangle} + \boldsymbol{\omega}^{\langle n\rangle}) \cdot \mathbf{x}^{\langle i\rangle}\right) \\ &= \sigma^2 \Big(\widetilde{\mathbf{w} \cdot \mathbf{w}^{\intercal}}\Big)(\boldsymbol{\omega}^{\langle m\rangle} + \boldsymbol{\omega}^{\langle n\rangle})\end{aligned} \tag{3.42}$$

Also it simply follows that

$$\mathbf{E}[\widetilde{\mathbf{v}}(\boldsymbol{\omega}^{\langle m\rangle})] = \mu\widetilde{\mathbf{w}}(\boldsymbol{\omega}^{\langle m\rangle}) \tag{3.43}$$

Based on the above information, it is possible to evaluate the propagation of the image noise into the measured displacement field. Assume that images f and g are corrupted by two different random uncorrelated white noises both with zero mean and variance σ^2. Consequently, one may consider $(f - g)$ to be corrupted by a random white noise with zero mean and variance $2\sigma^2$. Also, image gradient ∇g is corrupted by a random noise that results from interpolating the additive noise of deformed image g. However, perturbations induced

by the image derivatives may be neglected as compared to those resulted from the noise on $(f-g)$, especially, when the displacements are close to zero (see (Wang *et al.*, 2009) for more details). Therefore, one may rewrite equation (3.15) taking into account the stochastic term in the right-hand side as:

$$\begin{aligned}\frac{1}{N}\sum_{m=1}^{N}\left(H_\kappa\widetilde{\mathbf{M}}\right)(\boldsymbol{\omega}^{\langle n\rangle}-\boldsymbol{\omega}^{\langle m\rangle})\cdot\widetilde{\mathbf{u}}(\boldsymbol{\omega}^{\langle m\rangle}) &= \left(H_\kappa\widetilde{(f-g)\nabla g}\right)(\boldsymbol{\omega}^{\langle n\rangle})+\left(H_\kappa(\widetilde{\epsilon\nabla g})\right)(\boldsymbol{\omega}^{\langle n\rangle})\\ &= \left(H_\kappa(\widetilde{\epsilon\nabla g})\right)(\boldsymbol{\omega}^{\langle n\rangle}) \qquad (3.44)\end{aligned}$$

where ϵ is the additive noise on $(f-g)$, whose variance is $2\sigma^2$, and the last line follows from the fact that f and g are identical. By calculating the covariance matrices on the left and right sides while making use of equations (3.38) and (3.42), respectively, one obtains the following equation:

$$\begin{aligned}&\frac{1}{N^2}\sum_{m=1}^{N}\sum_{n=1}^{N}\left(H_\kappa\widetilde{\mathbf{M}}\right)(\boldsymbol{\omega}^{\langle k\rangle}-\boldsymbol{\omega}^{\langle m\rangle})\cdot\boldsymbol{\Gamma}^{\tilde{\mathbf{u}}}_{m,n}\cdot\left(H_\kappa\widetilde{\mathbf{M}}\right)(\boldsymbol{\omega}^{\langle l\rangle}-\boldsymbol{\omega}^{\langle n\rangle})\\ &\qquad= 2\sigma^2 H_\kappa(\boldsymbol{\omega}^{\langle k\rangle})H_\kappa(\boldsymbol{\omega}^{\langle l\rangle})\widetilde{\mathbf{M}}(\boldsymbol{\omega}^{\langle k\rangle}+\boldsymbol{\omega}^{\langle l\rangle})\\ &\qquad\simeq 2\sigma^2 H_\kappa(\boldsymbol{\omega}^{\langle k\rangle})\left(H_\kappa\widetilde{\mathbf{M}}\right)(\boldsymbol{\omega}^{\langle k\rangle}+\boldsymbol{\omega}^{\langle l\rangle}) \qquad (3.45)\end{aligned}$$

where $H_\kappa(\boldsymbol{\omega}^{\langle l\rangle})$ is replaced with $H_\kappa(\boldsymbol{\omega}^{\langle k\rangle}+\boldsymbol{\omega}^{\langle l\rangle})$ in the last line assuming $\kappa \ll L$. The left-hand side of the above equation contains two convolution products. Performing two inverse DFTs over $\boldsymbol{\omega}^{\langle k\rangle}$ and $\boldsymbol{\omega}^{\langle l\rangle}$ on both sides leads to:

$$\begin{aligned}&\frac{1}{N^4}\sum_{k=1}^{N}\sum_{l=1}^{N}\sum_{m=1}^{N}\sum_{n=1}^{N}\left[\exp\left(\hat{\imath}(\boldsymbol{\omega}^{\langle k\rangle}+\boldsymbol{\omega}^{\langle l\rangle})\cdot\mathbf{x}^{\langle i\rangle}\right)\left(H_\kappa\widetilde{\mathbf{M}}\right)(\boldsymbol{\omega}^{\langle k\rangle}-\boldsymbol{\omega}^{\langle m\rangle})\cdot\boldsymbol{\Gamma}^{\tilde{\mathbf{u}}}_{m,n}\cdot\left(H_\kappa\widetilde{\mathbf{M}}\right)(\boldsymbol{\omega}^{\langle l\rangle}-\boldsymbol{\omega}^{\langle n\rangle})\right]\\ &\qquad=\frac{2\sigma^2}{N^2}\sum_{k=1}^{N}\sum_{l=1}^{N}\left[\exp\left(\hat{\imath}(\boldsymbol{\omega}^{\langle k\rangle}+\boldsymbol{\omega}^{\langle l\rangle})\cdot\mathbf{x}^{\langle i\rangle}\right)H_\kappa(\boldsymbol{\omega}^{\langle k\rangle})\left(H_\kappa\widetilde{\mathbf{M}}\right)(\boldsymbol{\omega}^{\langle k\rangle}+\boldsymbol{\omega}^{\langle l\rangle})\right] \qquad (3.46)\end{aligned}$$

which simplifies to:

$$\begin{aligned}&\frac{1}{N^2}\sum_{m=1}^{N}\sum_{n=1}^{N}\widehat{\mathbf{M}}(\mathbf{x}^{\langle i\rangle})\cdot\boldsymbol{\Gamma}^{\tilde{\mathbf{u}}}_{m,n}\cdot\widehat{\mathbf{M}}(\mathbf{x}^{\langle i\rangle})\exp\left(\hat{\imath}(\boldsymbol{\omega}^{\langle m\rangle}+\boldsymbol{\omega}^{\langle n\rangle})\cdot\mathbf{x}^{\langle i\rangle}\right)\\ &\qquad=\frac{2\sigma^2}{N}\widehat{\mathbf{M}}(\mathbf{x}^{\langle i\rangle})\sum_{k=1}^{N}H_\kappa(\boldsymbol{\omega}^{\langle k\rangle})\exp\left(\hat{\imath}(\boldsymbol{\omega}^{\langle k\rangle}-\boldsymbol{\omega}^{\langle k\rangle})\cdot\mathbf{x}^{\langle i\rangle}\right) \qquad (3.47)\end{aligned}$$

using equation (3.1b). The summation over m and n in the left-hand side of the above equation can be simplified using (3.40) with $i = j$, which leads to the following equation in the spatial domain:

$$\widehat{\mathbf{M}}(\mathbf{x}^{\langle i\rangle}) \cdot \mathbf{\Gamma}^{\mathbf{u}}_{i,i} \cdot \widehat{\mathbf{M}}(\mathbf{x}^{\langle i\rangle}) = 2\sigma^2 \langle H_\kappa \rangle \ \widehat{\mathbf{M}}(\mathbf{x}^{\langle i\rangle}) \tag{3.48}$$

Therefore the relation for $\mathbf{\Gamma}^{\mathbf{u}}_{i,i}$ reads:

$$\mathbf{\Gamma}^{\mathbf{u}}_{i,i} = 2\sigma^2 \times \frac{2\pi\kappa^2}{4L^2} \widehat{\mathbf{M}}^{-1}(\mathbf{x}^{\langle i\rangle}) \tag{3.49}$$

where $N = 4L^2$ was used to calculate the value for $\langle H_\kappa \rangle$. The variance of the displacement components at the i-th pixel is the diagonal elements of $\mathbf{\Gamma}^{\mathbf{u}}_{i,i}$, which is:

$$\begin{aligned}
\left(\mathbf{\Gamma}^{\mathbf{u}}_{i,i}\right)_{nn} &= \mathbf{E}\left[u_n^2(\mathbf{x}^{\langle i\rangle})\right] - \mathbf{E}\left[u_n(\mathbf{x}^{\langle i\rangle})\right]^2 \\
&= \mathbf{E}\left[u_n^2(\mathbf{x}^{\langle i\rangle})\right] \\
&= \pi\sigma^2 \left(\frac{\kappa}{L}\right)^2 \widehat{M}^{-1}_{nn}(\mathbf{x}^{\langle i\rangle}) \quad (n = 1, 2)
\end{aligned} \tag{3.50}$$

where $\left(\mathbf{\Gamma}^{\mathbf{u}}_{i,i}\right)_{nn}$ denotes the diagonal elements of $\mathbf{\Gamma}^{\mathbf{u}}_{i,i}$ and $\mathbf{E}\left[u_n(\mathbf{x}^{\langle i\rangle})\right] = 0$ follows from (3.43) and (3.44) as well as the fact $\mu = 0$ for the white noise. One may use the above result to approximately calculate the RMS of u_n as follows:

$$\begin{aligned}
\mathrm{rms}(u_n) &= \sqrt{\langle u_n^2(\mathbf{x}^{\langle i\rangle})\rangle} \\
&\simeq \sqrt{\langle \mathbf{E}\left[u_n^2(\mathbf{x}^{\langle i\rangle})\right]\rangle} \\
&\simeq \sigma \frac{\kappa}{L} \sqrt{\pi \left\langle \widehat{M}^{-1}_{nn} \right\rangle} \quad (n = 1, 2)
\end{aligned} \tag{3.51}$$

Provided the texture variations are isotropic, the RMS values of both displacement components are close to each other. Moreover, instead of calculating the mean value $\left\langle \widehat{M}^{-1}_{nn} \right\rangle$, one may approximate it with $\left\langle \widehat{M}_{nn} \right\rangle^{-1}$. The latter is unified for both components by averaging it over $n = 1, 2$ which gives $\dfrac{2}{\langle \|\nabla g\|^2 \rangle}$. Therefore, the theoretical RMS value simplifies to:

$$\mathrm{rms}\,(u_1) \simeq \mathrm{rms}\,(u_2) \simeq \sigma \frac{\kappa}{L} \sqrt{\frac{2\pi}{\langle \|\nabla g\|^2 \rangle}} \tag{3.52}$$

3.13 REFERENCES

BAY, B. K. (1995). Texture correlation: A method for the measurement of detailed strain distributions within trabecular bone. *Journal of Orthopaedic Research*, 13, 258–267.

BESNARD, G., HILD, F. and ROUX, S. (2006). "finite-element" displacement fields analysis from digital images: Application to portevin-le châtelier bands. *Experimental Mechanics*, 46, 789 – 803.

BORNERT, M., BRÉMAND, F., DOUMALIN, P., DUPRÉ, J., FAZZINI, M., GRÉDIAC, M., HILD, F., MISTOU, S., MOLIMARD, J., ORTEU, J. J., ROBERT, L., SURREL, Y., VACHER, P. and WATTRISSE, B. (2009). Assessment of digital image correlation measurement errors: Methodology and results. *Experimental Mechanics*, 49, 353–370.

CHENG, P., SUTTON, M., SCHREIER, H. and MCNEILL, S. (2002). Full-field speckle pattern image correlation with B-Spline deformation function. *Experimental Mechanics*, 42, 344–352.

CLAIRE, D., HILD, F. and ROUX, S. (2004). A finite element formulation to identify damage fields: the equilibrium gap method. *International Journal for Numerical Methods in Engineering*, 61, 189–208.

D'ERRICO, J. (2005). Surface fitting using gridfit. Matlab Central Files (url:http://www.mathworks.com/matlabcentral/fileexchange/8998), Retrieved 10 May, 2011.

FONSECA, J. Q. D., MUMMERY, P. M. and WITHERS, P. J. (2005). Full-field strain mapping by optical correlation of micrographs acquired during deformation. *Journal of Microscopy*, 218, 9–21.

GEYMONAT, G. and PAGANO, S. (2003). Identification of mechanical properties by displacement field measurement: A variational approach. *Meccanica*, 38, 535–545.

GONZALEZ, R. C. and WOODS, R. E. (2007). *Digital Image Processing (3rd Edition)*. Prentice Hall.

GRÉDIAC, M. (2004). The use of full-field measurement methods in composite material characterization: interest and limitations. *Composites Part A: Applied Science and Manufacturing*, 35, 751 – 761.

HARDISTY, M. R. and WHYNE, C. M. (2009). Whole bone strain quantification by image registration: A validation study. *Journal of Biomechanical Engineering-Transactions of the ASME*, 131.

HILD, F., PÉRIÉ, J.-N. and CORET, M. (1999). Mesure de champs de déplacements 2D par corrélation d'images numériques : Correli^{2d}, LMT-Cachan.

HILD, F. and ROUX, S. (2012). Comparison of local and global approaches to digital image correlation. *Experimental Mechanics*, 52, 1503–1519.

KEYS, R. (1981). Cubic convolution interpolation for digital image processing. *Acoustics, Speech and Signal Processing, IEEE Transactions on*, 29, 1153 – 1160.

LECLERC, H., PÉRIÉ, J.-N., ROUX, S. and HILD, F. C. (2009). Integrated digital image correlation for the identification of mechanical properties. *Proceedings of the 4th International Conference on Computer Vision/Computer Graphics CollaborationTechniques*. Springer-Verlag, Berlin, Heidelberg, MIRAGE '09, 161–171.

LU, H. and CARY, P. (2000). Deformation measurements by digital image correlation: Implementation of a second-order displacement gradient. *Experimental Mechanics*, 40, 393 – 400.

MENG, L., JIN, G. and YAO, X. (2007). Application of iteration and finite element smoothing technique for displacement and strain measurement of digital speckle correlation. *Optics and Lasers in Engineering*, 45, 57 – 63.

NOCEDAL, J. and WRIGHT, S. J. (2000). *Numerical Optimization*. Springer.

PAN, B. (2009). Reliability-guided digital image correlation for image deformation measurement. *Appl. Opt.*, 48, 1535–1542.

PAN, B., HUIMIN, X., TAO, H., WEINING, W. and YAN, F. (2006). Displacement smoothing and strain estimation using savitaky-golay filters in digital image correlation. *Key Engineering Materials*, 326-328 I, 135 – 138.

PAN, B. and LI, K. (2011). A fast digital image correlation method for deformation measurement. *Optics and Lasers in Engineering*, 49, 841 – 847.

PASSIEUX, J.-C. and PÉRIÉ, J.-N. (2012). High resolution digital image correlation using proper generalized decomposition: Pgd-dic. *International Journal for Numerical Methods in Engineering*, 92, 531–550.

PÉRIÉ, J.-N., LECLERC, H., ROUX, S. and HILD, F. (2009). Digital image correlation and biaxial test on composite material for anisotropic damage law identification. *International Journal of Solids and Structures*, 46, 2388–2396.

QIU, H., YAN, J., KWON, O.-H. and SUTTON, M. A. (2008). Crack detection by digital image correlation. *11th International Congress and Exhibition on Experimental and Applied Mechanics 2008*. Society for Experimental Mechanics, Orlando, FL, United states, vol. 2, 927 – 933.

RÉTHORÉ, J., ELGUEDJ, T., SIMON, P. and CORET, M. (2010). On the use of nurbs functions for displacement derivatives measurement by digital image correlation. *Experimental Mechanics*, 50, 1099–1116.

RÉTHORÉ, J., HILD, F. and ROUX, S. (2007). Shear-band capturing using a multiscale extended digital image correlation technique. *Computer Methods in Applied Mechanics and Engineering*, 196, 5016 – 5030.

ROUX, S., HILD, F. and BERTHAUD, Y. (2002). Correlation image velocimetry: A spectral approach. *Applied Optics*, 41, 108–115.

SCHREIER, H. W., BRAASCH, J. R. and SUTTON, M. A. (2000). Systematic errors in digital image correlation caused by intensity interpolation. *Optical Engineering*, 39, 2915–2921.

SMITH, B., LI, X. and TONG, W. (1998). Error assessment for strain mapping by digital image correlation. *Experimental Techniques*, 22, 19 – 21.

SUN, Y., PANG, J. H. L., WONG, C. K. and SU, F. (2005). Finite element formulation for a digital image correlation method. *Applied Optics*, 44, 7357 – 7363.

SUTTON, M., WOLTERS, W., PETERS, W., RANSON, W. and MCNEILL, S. (1983). Determination of displacements using an improved digital correlation method. *Image and Vision Computing*, 1, 133 – 139.

UNSER, M., ALDROUBI, A. and EDEN, M. (1993a). B-spline signal processing. i. theory. *Signal Processing, IEEE Transactions on*, 41, 821 –833.

UNSER, M., ALDROUBI, A. and EDEN, M. (1993b). B-spline signal processing. ii. efficiency design and applications. *Signal Processing, IEEE Transactions on*, 41, 834 –848.

VENDROUX, G. and KNAUSS, W. (1998). Submicron deformation field measurements: Part 2. improved digital image correlation. *Experimental Mechanics*, 38, 86–92.

WAGNE, B., ROUX, S. and HILD, F. (2002). Spectral approach to displacement evaluation from image analysis. *Eur. Phys. J. AP*, 17, 247–252.

WANG, Y., SUTTON, M., BRUCK, H. and SCHREIER, H. (2009). Quantitative error assessment in pattern matching: Effects of intensity pattern noise, interpolation, strain and image contrast on motion measurements. *Strain*, 45, 160 – 178.

WATTRISSE, B., CHRYSOCHOOS, A., MURACCIOLE, J.-M. and NÉMOZ-GAILLARD, M. (2001). Analysis of strain localization during tensile tests by digital image correlation. *Experimental Mechanics*, 41, 29 – 39.

CHAPTER 4

ARTICLE 2: A GLOBAL DIGITAL IMAGE CORRELATION APPROACH TO HIGH-RESOLUTION FULL-FIELD STRAIN MEASUREMENTS: APPLICATIONS TO COMPOSITES AT MICRO-SCALE

F. Mortazavi, L.P. Canal, C. González, J. Llorca, M. Lévesque, I. Villemure (2013). submitted to *Composites Part A* on February 2, 2013.

4.1 Abstract

This paper deals with high-resolution reconstruction of full-field displacements/strains in composite materials. A global image correlation approach has been developed in which displacement fields are retrieved based on Fourier decomposition for the sought displacement field. Application of the approach in composites is studied using simulated as well as real experimental SEM images of a fiber-reinforced composite. Performance evaluations by simulated experiments show that this method has significantly high capabilities in measuring high-resolution strains. The simulated experiments also reveal that the existing image noise was significantly detrimental to the accuracy of the real measurement inasmuch as it may have reduced the reconstruction capacity to 23%. Finally, the real measurements have been performed using the measurement parameters identified from the simulated experiments. The analysis of the simulated and real measurements and their comparison with previous studies demonstrate the high performance of the developed approach in dealing with composites at micro-scale.

4.2 Introduction

Along with the increasing theoretical advances in the mechanical modeling of multi-length-scale composites, there has been a growing urge for obtaining experimental benchmarks that relate the microstructure to its micro-scale deformations. Providing such information not only serves to validate numerical simulations (Lomov *et al.*, 2008), but also could be used to develop efficient representative models and assumptions, which help to improve design tools for composites (Guillebaud-Bonnafous *et al.*, 2012; Anzelotti *et al.*, 2008). A typical example is polymer composites in which the interphase model plays a significant role in the accurate prediction of composite response at different length scales. Particularly, it is often sought

how the micro-scale interphase transfers the stress between phases. Similar studies on different composites can be found in the literature (Guillebaud-Bonnafous *et al.*, 2012; Moutrille *et al.*, 2009). From this perspective, techniques providing full-field displacements/strains measurements become very appealing, especially when coupled with inverse identification of mechanical properties, for bridging the gap between theoretical interphase modeling and the real characteristics of composites. Among various existing techniques, Digital Image Correlation (DIC) has been widely used in experimental mechanics. DIC is based on establishing spatial correspondences between two images acquired from the same test specimen in its unloaded state and in its deformed state. The technique has been used for different purposes from strain mapping in materials science applications (Fonseca *et al.*, 2005; Chivers and Clocksin, 2000) to mechanical identification (Makeev *et al.*, 2012; Grédiac, 2004; Geymonat and Pagano, 2003) and damage characterization (Périé *et al.*, 2009; Fouinneteau and Pickett, 2007; Claire *et al.*, 2004) for a variety of composites. As for composites at micro-scale, efforts have been recently made to capture particle-scale strain heterogeneities using DIC technique based on images from optical microscope (Nicoletto *et al.*, 2011) and Scanning Electron Microscope (SEM) (Canal *et al.*, 2012). In both works, DIC approaches relying on point-wise subset-based correlation schemes have been used. Consequently, the correlation results in discrete displacement fields. The reports show that the DIC was capable of estimating the overall strain (i.e. the volume average of the local strain field) with reasonable accuracy. However, due to the lack of inter-subset continuity as well as the small number of Degrees of Freedom (DOF) in the subset displacement for the correlation, the measured strains did not precisely follow the expected inhomogeneous trend at the micro-scale level.

During the past decade, researchers have developed global approaches to retrieve spatially dependent displacement fields within the whole Region of Interest (ROI) based on decomposition of the sought displacement field over some chosen basis functions, e.g. B-Splines (Cheng *et al.*, 2002; Réthoré *et al.*, 2010) or Finite Element (FE) shape functions (Sun *et al.*, 2005; Besnard *et al.*, 2006). Thus, measurement uncertainties became smaller than those of subset-based DIC (Hild and Roux, 2012; Cheng *et al.*, 2002). Enriching the details of displacement fields thus retrieved could be achieved by increasing the number of DOF in the decomposition (e.g. through refining the B-Spline/FE mesh), hence making global approaches suitable for complex displacements. However, as the number of correlation variables increases, the algorithms require larger amounts of memory to deal with the huge correlation problem, which makes the processing times prohibitive. Interesting approaches have been recently proposed to remedy this problem (Leclerc *et al.*, 2009; Passieux and Périé, 2012; Mortazavi *et al.*, 2013). Among them, Mortazavi et al. (Mortazavi *et al.*, 2013) presented an Improved Spectral Approach (ISA) based on spectral decomposition of displacements,

which followed the work of Wagne *et al.* (2002). The presented methodology led to a fast and memory-efficient algorithm thanks to Fast Fourier Transform (FFT) while precisely estimating continuous displacements in a more natural way, i.e. reconstructing the displacement Fourier expansion. With this approach, more spatially complex displacement fields can be determined without significantly increasing the complexity of the correlation procedure. One important issue addressed in (Mortazavi *et al.*, 2013) was dealing with the periodicity problem associated with the Fourier-based decomposition. To this end, a two-fold correlation scheme was implemented in which the overall shape of the displacement function was first roughly estimated by a subset-based DIC followed by the reconstruction of accurate details by the ISA.

In this paper, we explore the potential applications of the ISA to composite materials at the micro-scale level. First, a hybrid approach that improves on the previously developed methodology (Mortazavi *et al.*, 2013) is presented. Particularly, a computationally efficient Multi-scale Non-linear Optimization Scheme (MNOS) is devised in the first step of the algorithm instead of the subset-based DIC. The MNOS uses B-Spline basis functions to reconstruct the approximate continuous displacement field; hence there is no further need to interpolate/extrapolate the measured displacements at all pixel points (as opposed to the previous approach). Finally, the capacity of the developed approach to capture spatial heterogeneities of micro-mechanical strains in composites is investigated using both simulated and real experiments.

4.3 Background

4.3.1 Concept of pattern matching

Let $f(\mathbf{x})$ and $g(\mathbf{x})$ represent the intensity functions of spatial coordinates $\mathbf{x}$, which correspond to the undeformed and deformed images, respectively. In ideal conditions, these two configurations are correlated through a mapping of coordinates, which is expressed by the following relation:

$$f(\mathbf{x}) = g(\breve{\mathbf{x}}) \quad \text{where} \tag{4.1a}$$

$$\breve{\mathbf{x}} = \mathbf{x} + \mathbf{u}_{\text{exact}}(\mathbf{x}) \tag{4.1b}$$

where $\mathbf{u}_{\text{exact}}(\mathbf{x})$ is the displacement vector field as resulting from the applied loads. The exact displacement should be estimated by a mathematical function with specified Degrees of Freedom (DOF), i.e.:

$$\mathbf{u}_{\text{exact}}(\mathbf{x}) \approx \mathbf{u}(\mathbf{x}; \mathbf{p}) \tag{4.2}$$

where $\mathbf{p}$ is the set of parameters that should be determined from pattern matching. The pattern matching consists in finding the parameters that minimize the gap between $f(\mathbf{x})$ and $g(\check{\mathbf{x}})$. This can be expressed as follows:

$$\mathbf{p}_{\text{opt}} = \underset{\mathbf{p}\in\mathcal{A}}{\arg\min} \left\{ \sum_{i=1}^{N} r_i^2(\mathbf{p}) \right\} \quad \text{where} \tag{4.3a}$$

$$r_i(\mathbf{p}) := f(\mathbf{x}^{\langle i\rangle}) - g\left(\mathbf{x}^{\langle i\rangle} + \mathbf{u}\big(\mathbf{x}^{\langle i\rangle};\mathbf{p}\big)\right) \tag{4.3b}$$

where N is the total number of image pixels, $\mathcal{A}$ denotes the set of admissible choices for $\mathbf{p}$ and i is the pixel index.

4.3.2 B-Spline-based pattern matching

B-Spline functions are piece-wise polynomials that unlike FE shape functions may possess specified degrees of continuity making them very powerful and efficient in constructing smooth curves and surfaces. In B-Spline-based pattern matching (Cheng *et al.*, 2002), the displacement field is expressed as a continuous function made with such basis functions, i.e.:

$$\mathbf{u}(\boldsymbol{\xi}) = \sum_{i=1}^{m_1}\sum_{j=1}^{m_2} B_{i,p}(\xi_1)B_{j,p}(\xi_2)\mathbf{d}^{\langle i,j\rangle} \tag{4.4}$$

where $B_{i,p}(\xi)$ is the i-th univariate B-Spline basis function (of p-degree), $\boldsymbol{\xi} = (\xi_1, \xi_2)$ is the pair of normalized coordinates within the parametric space $[0,1]\times[0,1]$ associated to the image zone of interest, m_1 and m_2 are the total numbers of basis functions in each direction and $\mathbf{d}^{\langle i,j\rangle}$ are the vector amplitudes associated to the 2D basis functions. To define a univariate B-Spline function, a knot sequence in the parametric space is needed, say $\{\xi^{\langle 1\rangle}, \xi^{\langle 2\rangle}, \cdots, \xi^{\langle m+p+1\rangle}\}$, which is analogous to FE nodes except that B-Splines may include knots with multiplicities. Knowing the knot sequence, the B-Spline basis function is defined using the following recursive formula:

$$B_{i,0}(\xi) = \begin{cases} 1 & \xi^{\langle i\rangle} \le \xi < \xi^{\langle i+1\rangle} \\ 0 & \text{otherwise} \end{cases} \tag{4.5a}$$

$$B_{i,p}(\xi) = \frac{\xi - \xi^{\langle i\rangle}}{\xi^{\langle i+p\rangle} - \xi^{\langle i\rangle}} B_{i,p-1}(\xi) + \frac{\xi^{\langle i+p+1\rangle} - \xi}{\xi^{\langle i+p+1\rangle} - \xi^{\langle i+1\rangle}} B_{i+1,p-1}(\xi) \tag{4.5b}$$

As a visual example, Figure 4.1 illustrates the deformation mechanism defined by cubic B-Spline functions ($p = 3$) for a chosen knot sequence. As seen from the figure, the coefficients $\mathbf{d}^{\langle i,j \rangle}$ convey a geometrical insight about the shape of the deformed area, which is similar to nodal displacements in FE method. However, unlike in FE-based transformation, the deformed shape does not necessarily coincide with the deformed *control net* generated from the chosen knot array (except for the corners). This is due to the fact that the B-Spline basis functions are not *interpolatory* (at least at interior knots), which leads to curves and surfaces of maximum C^{p-1} continuity. This advantage improves the versatility of the transformation without significantly increasing the number of DOF in contrast with FE. This leads to more adaptable correlations with relatively lower uncertainties caused by DOF of the inverse problem (Réthoré *et al.*, 2010).

Finally, the unknown parameters for the displacement field thus defined (using cubic B-Splines) are determined through solving equation (4.3) using non-linear least-squares Levenberg-Marquardt (LM) minimization algorithm. Thanks to the compact support of basis functions, the Jacobian matrix contains remarkably large number of zero elements, which enables a sparse implementation of the least-square algorithm leading to a quite time-efficient algorithm.

4.3.3 Improved spectral approach

As its name implies, the method relies on the spectral decomposition of the displacement field using the following Fourier basis functions (Hild *et al.*, 2002; Roux *et al.*, 2002):

$$\psi_n(\mathbf{x}) = \exp\left(\hat{\imath}\boldsymbol{\omega}_n \cdot \mathbf{x}\right) \quad (n = 1, 2, \cdots, N) \tag{4.6}$$

where $\mathbf{x} = (x_1, x_2)$ is the pair of coordinates (in pixel units) of points in the Euclidean space, $\mathbf{x}^{\langle i \rangle}$ refers to the coordiantes of the i-th pixel in the image, $\boldsymbol{\omega} = (\omega_1, \omega_2)$ denotes the pair of radian frequencies (rad/pixel) in the Fourier domain within the square $[-\pi, \pi) \times [-\pi, \pi)$, which are uniformly discretized so that $\boldsymbol{\omega}_n$ refers to the n-th frequency sample and N is the total number of frequency samples (or equivalently, total number of pixels). Due to the ill-posed nature of the correlation problem, one may not use the entire N frequency terms to estimate the displacements. Therefore, the following filtered decomposition of the displacement field is used in the improved spectral approach:

$$\mathbf{u}(\mathbf{x}) = \sum_{n=1}^{N} \big(H_\kappa \mathbf{v}\big)(\boldsymbol{\omega}_n) \exp\left(\hat{\imath}\boldsymbol{\omega}_n \cdot \mathbf{x}\right) \tag{4.7}$$

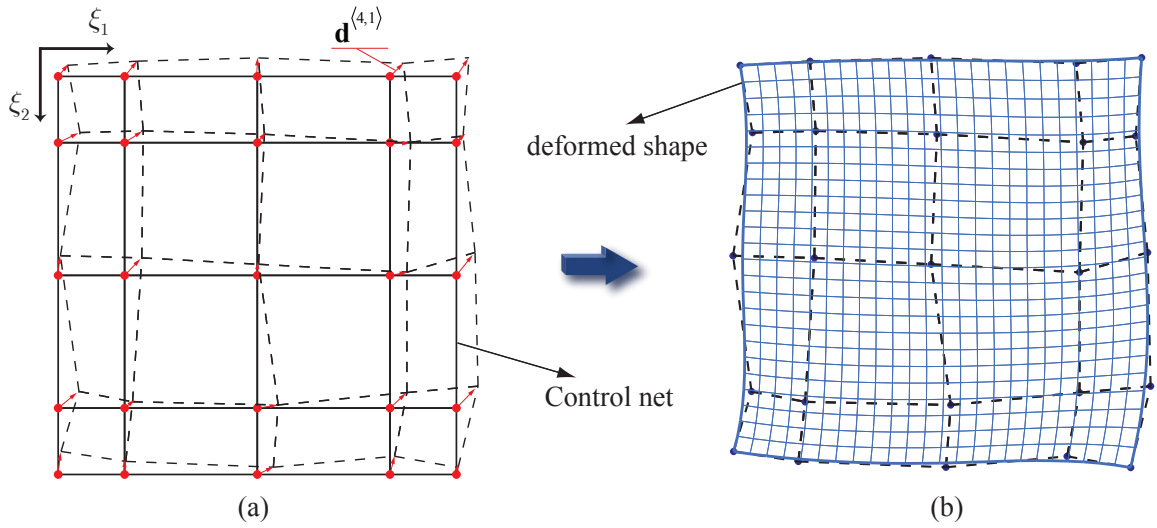

Figure 4.1 (a) Deformation of the control net generated according to the chosen knot spacing. The displacements of the control points are the parameters that control the final shape of the body. (b) The deformed shape produced by the displacements of the control points. Note that unlike the FE-based transformations, the deformed shape does not pass through the control points except for the four corner points.

where $\mathbf{v}(\boldsymbol{\omega}_n)$ is the amplitude of the basis function corresponding to $\boldsymbol{\omega}_n$ for the decomposition of the displacement vector $\mathbf{u}(\mathbf{x})$ and the multiplied mask function $H_\kappa(\boldsymbol{\omega}_n)$ has the following Gaussian distribution:

$$H_\kappa(\boldsymbol{\omega}) = \exp\left(-\frac{L^2\|\boldsymbol{\omega}\|^2}{2\pi^2\kappa^2}\right) \tag{4.8}$$

where κ is the cutoff wavenumber corresponding to this filter and L refers to the image half-width. The Gaussian mask enables gradual attenuation of high-frequency basis functions. Thus, one expects to enrich the displacement estimation by partially involving high-frequency terms. The above mask was shown in the previous study (Mortazavi *et al.*, 2013) to significantly improve the accuracy of the correlation algorithm, when compared to the ideal mask originally proposed (Wagne *et al.*, 2002). To estimate the displacement field according to the above decomposition, the amplitudes $\mathbf{v}(\boldsymbol{\omega}_n)$ should be determined through pattern matching, i.e. minimization of the correlation error defined in equation (4.3b). A common way to do this is to linearize the mentioned residuals with respect to the amplitudes and subsequently establish the first-order optimality condition, the solution of which leads to an estimate of the unknown coefficients (Besnard *et al.*, 2006). These steps were thoroughly explained in a previous paper by the authors (Mortazavi *et al.*, 2013), to which the reader is referred for details. In doing so and after simplifications, the governing equation for the improved

spectral approach is obtained:

$$\sum_{m=1}^{N} \Big(H_\kappa \widetilde{\nabla g \nabla g^\intercal}\Big)(\boldsymbol{\omega}_n - \boldsymbol{\omega}_m) \cdot \Big(H_\kappa \mathbf{v}\Big)(\boldsymbol{\omega}_m) = \Big(H_\kappa \widetilde{(f-g)\nabla g}\Big)(\boldsymbol{\omega}_n) \tag{4.9}$$

where $\widetilde{\square}$ denotes the Discrete Fourier Transform (DFT) of a function. As can be seen from the above equation, the series in the left-hand-side is a discrete convolution product. By applying the inverse DFT on the above equation, the convolution operation turns into a simple matrix product in the real space, i.e.:

$$\Big((\widehat{\nabla g \otimes \nabla g}) \cdot \mathbf{u}\Big)(\mathbf{x}^{\langle i \rangle}) = \Big(\widehat{(f-g)\nabla g}\Big)(\mathbf{x}^{\langle i \rangle}) \tag{4.10}$$

where $\widehat{(\,)}$ denotes low-pass filtering in the frequency domain using the mask H_κ. The above equation leads to two explicit expressions for the displacement components that can be evaluated for all the pixels simultaneously, e.g. using array operations of MATLAB. The main computational burden is performing a forward and a backward DFT to apply the filtering. However, thanks to FFT algorithm, these operations are carried out quite efficiently, leading to a fast and memory-efficient algorithm.

In the implemented algorithm, the displacements are progressively reconstructed using equation (3.18) in an iterative process. In this regard, stopping criteria play important roles in the robustness of the results. This has been addressed in (Mortazavi *et al.*, 2013) where several criteria were introduced. In order to reach subpixel-level accuracy, bicubic spline interpolation was used to interpolate the deformed image at sub-pixel positions.

4.4 Hybrid spectral approach

The major utility of a hybrid (two-step) algorithm, while using a spectral approach, is to remove the limitation imposed by the Fourier-based decomposition of the displacement field in the spectral approach, i.e. the periodicity of the resulted measurements. This was shown by Mortazavi et al. (Mortazavi *et al.*, 2013) to efficiently operate for non-periodic images and displacement fields. The main difference herein is the use of the B-Spline-based pattern matching (section 4.3.2) instead of the local approach used in the mentioned study. The advantage is that the resulting displacement field is continuous and therefore no further interpolation/extrapolation is required to generate a continuous displacement field prior to applying the improved spectral approach. Furthermore, thanks to the efficiency and flexibility of the B-Spline basis functions, the prior estimation of the displacement field is more representative of the actual state to be measured, hence adding to the accuracy of the whole

algorithm.

4.4.1 Multi-scale non-linear optimization scheme

In order to solve the minimization problem 4.3 using the B-Spline approach, initial estimates of the displacement parameters are required. According to a previous report (Cheng *et al.*, 2002), the initial estimate of the displacement should be within ±3 pixels from the accurate solution in order for the LM algorithm not to fall in local minima. To circumvent this problem, a multi-scale iteration scheme is devised herein, inspired by those implemented in several previous approaches (Besnard *et al.*, 2006; Réthoré *et al.*, 2010, 2007). However, unlike in the mentioned studies, the present multi-scale scheme is coupled to a non-linear optimization algorithm leading to a Multi-scale Non-linear Optimization Scheme (MNOS). The idea is to derive coarse-grained pair of images by proper down-scaling of the original ones so that the sought displacement magnitudes decrease down to around 3 units of coarse pixels. Thus, an initial estimate of zero values for the parameters would lead to a good estimation of the displacements at low magnification using LM algorithm. The next sequence of iterations is performed at a higher image resolution using the initial estimate found from the previous solution. This procedure continues until reaching the original scale of images. Figure 4.2 illustrates the idea behind the MNOS algorithm.

A few important points about MNOS are worth considering. First, it should be noted that at low resolutions, a small number of knot divisions (hence a few variables) are required to estimate the coarse displacements, which makes the LM iterations quite fast (around a few seconds on a normal PC). The knot spacings are then successively refined as the resolution level is increased. Furthermore, thanks to the use of non-linear least-square algorithm, a few resolution levels (1 to 5) are often enough to have a suitable initial estimate for solving the correlation problem at the original scale. This advantage, along with the sparse implementation of the LM algorithm, makes the whole MNOS algorithm fast enough to be coupled with the next step, i.e. the improved spectral approach.

4.5 Experimental and numerical evaluations

Artificial and real experiments were conducted to evaluate the potential application of the hybrid spectral approach to composites at microscale. For the artificial experiments, pre-imposed displacement fields representative of the microscale mechanical behavior of composites were required. To this end, FE analysis was used, which is explained in the sequel.

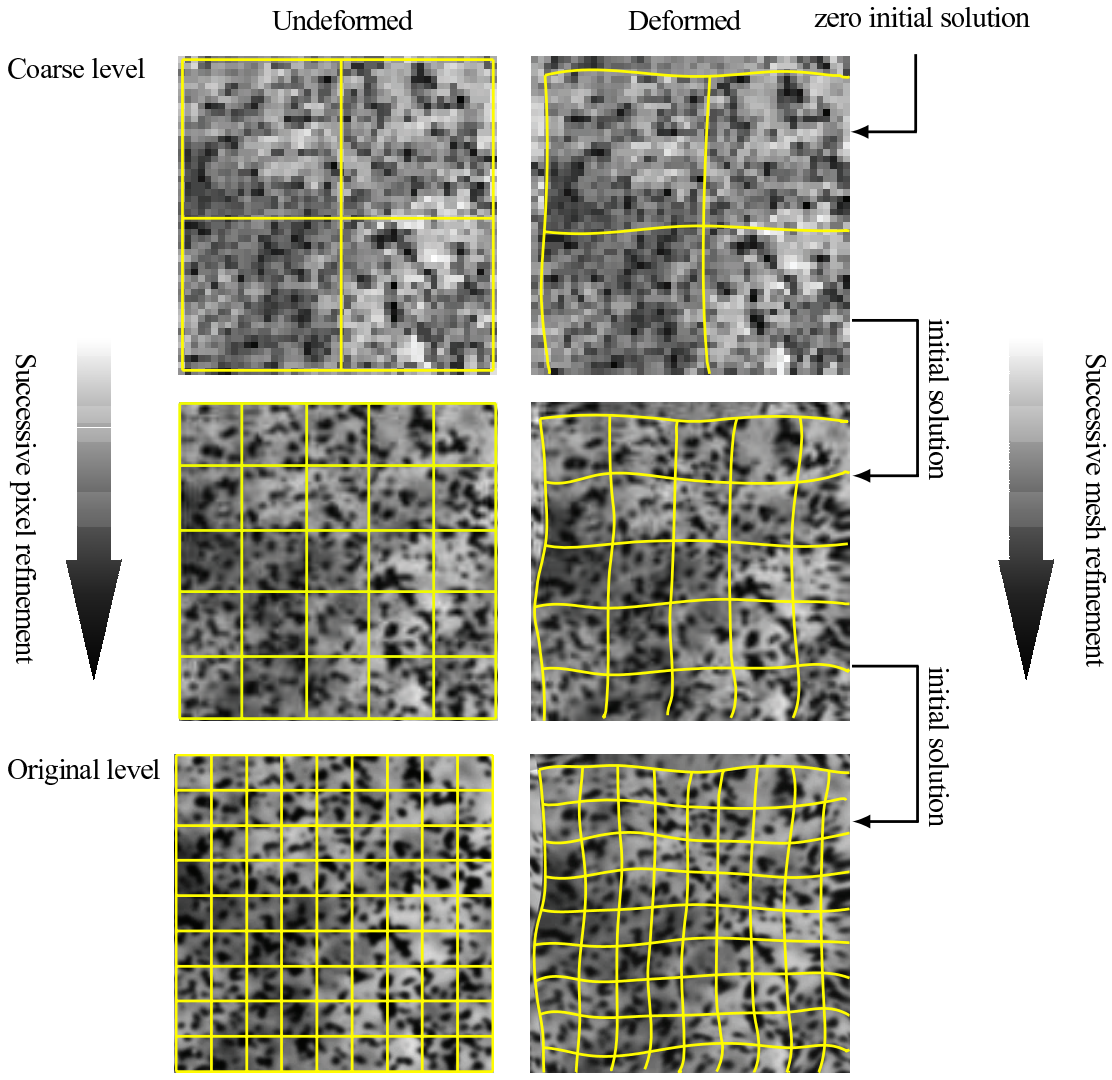

Figure 4.2 Schematics of the multi-scale correlation using non-linear least-squares minimization, which is carried out prior to applying the improved spectral algorithm. The B-Spline mesh is successively refined as the scale increases.

4.5.1 SEM images

SEM images from the surface of a fiber-reinforced sample at micro-scale were taken from the work of Canal *et al.* (2012) who evaluated strain fields using a subset-based DIC commercial software. Details of the experimental techniques used to prepare samples and the SEM images can be found in the mentioned study. Two sets of experimental data (undeformed/deformed images) were selected herein (Figure 4.3), namely, images at 2000× and 6000× magnifications. The deformed images correspond to sample subjected to a vertical

load perpendicular to the fiber longitudinal directions. All images were 768 × 1024 pixels with 8-bit grey levels and histograms shown on Figure 4.3-(e) and (f).

4.5.2 Numerical model

FE analysis was employed to simulate the full-field strain on the real micro-structure. The same mechanical properties and assumptions as in (Canal *et al.*, 2012) were used in order to be consistent with the previous results. Both fiber and matrix were considered as linear elastic isotropic solids whose properties are listed in Table 5.1. In this model, the exact microstructure shown in Figure 4.3 (at both scales) was reproduced and subsequently meshed with 6-node isoparametric modified triangular elements (CPE6M) in ABAQUS Standard. The experimental data considered herein correspond to loading where no fiber decohesion was observed in the SEM images. Therefore, the matrix/fiber interfaces were assumed to be perfect and damage by decohesion was not included in the model.The analysis was carried out under applied displacements condition at the boundaries using actual displacement values measured by the Hybrid Approach, hence imposing identical overall strains for both measured and simulated strains. The computed vertical displacement and the vertical normal strain for 2000× magnification are shown in Figure 4.4 for illustration purposes.

Table 4.1 Elastic properties of the matrix and fiber used in the FE analysis. The values were taken from (Canal *et al.*, 2012) for consistency with the mentioned study.

	E (GPa)	ν
MTM57 epoxy matrix	3.35	0.35
E-glass fiber	74	0.20

4.5.3 Artificial experiments

Artificial experiments were first performed to assess the potential of the developed algorithm under a-priori-known conditions, i.e. induced displacement fields and noise level. Four sets of simulated experiments were considered for evaluation. In all experiments, the mapping of the reference images to the deformed configuration was performed analytically, thus avoiding interpolation errors during the generation of the deformed image.The first set consisted in artificially deforming a synthetic textured-image using the displacement fields calculated by the FE analyses. Figure 4.5 shows the used synthetic image, which was generated according to specifications explained in (Mortazavi *et al.*, 2013). The intensities were quantized to 12 bits to minimize uncertainties caused by image quantization. Both 2000×

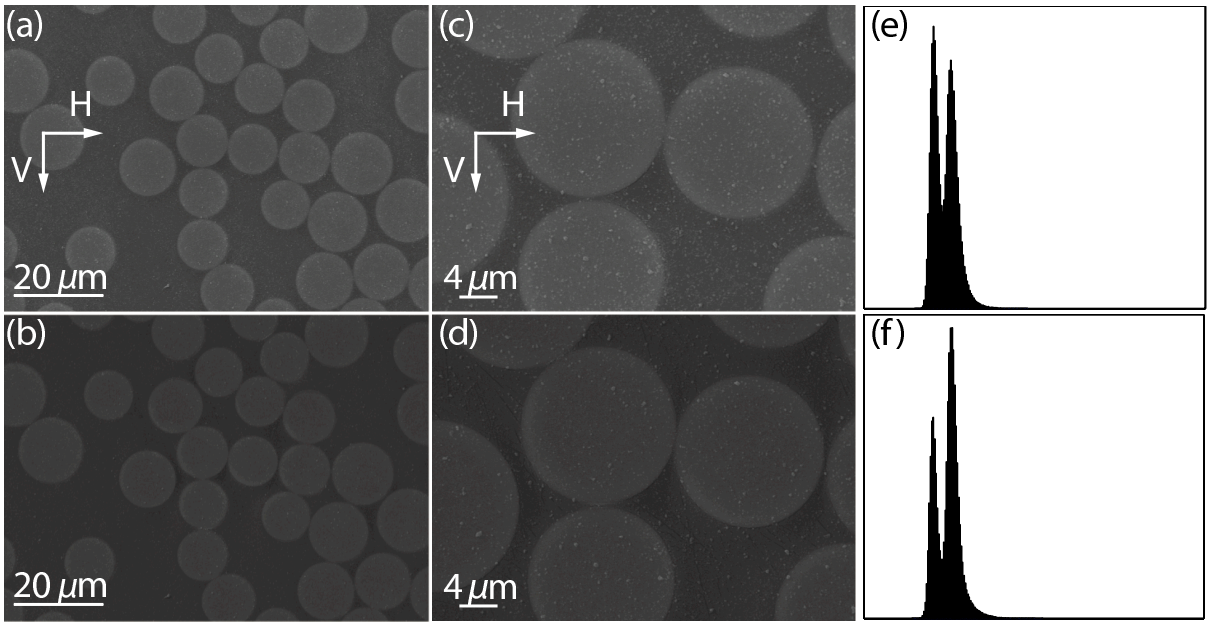

Figure 4.3 SEM images of the composite sample taken from the work of Canal *et al.* (2012). (a) and (c) undeformed sample, (b) and (d) deformed sample and (e) and (f) image histograms (for the undeformed images) at 2000× and 6000× magnifications, respectively.

and 6000× magnifications were considered. The second set of experimental data was generated by artificially deforming the SEM images according to the FE displacement fields. Since there was no analytical function defining the SEM images, image mapping to the deformed configuration was carried out by transforming the Fourier series expansion of the image function. This simulated experiment served to evaluate the maximum attainable accuracy for the specific texture under study. To this end, noise-induced intensity variations were effectively eliminated from the SEM images using image smoothing prior to the artificial transformation. Thus, the image texture better represented the characteristics of the real surface. The third and the forth sets of experiments were generated by corrupting the first two sets of input images (synthetic and SEM) by random white noises. The corresponding noise levels were obtained from the analysis of the original SEM images. A reliable way to do this was proposed in (Hild and Roux, 2012), which involved correlating successive images from the undeformed state of the sample. This approach was not followed herein due to insufficient experimental data. Instead, the noise level in the SEM images was roughly estimated by subtracting the smoothed and original images, i.e.

$$\sigma_n \approx \mathrm{STD}\left[f_{SEM}(\mathbf{x}) - f^{\star}_{SEM}(\mathbf{x})\right] \tag{4.11}$$

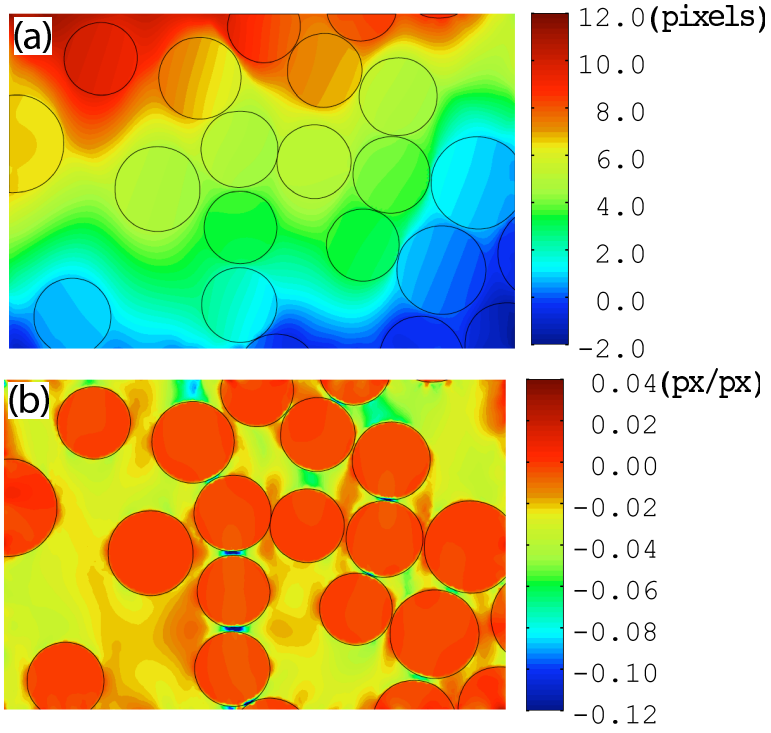

Figure 4.4 FE-calculated vertical displacement and strain fields for 2000× magnification (a) vertical displacement field (b) vertical normal strain field

where σ_n is the noise level, f_{SEM} and $f^{\star}_{SEM}$ denote the original and smooth SEM images, respectively, and STD[] operator calculates the standard deviation of the data over the Region Of Interest (ROI).

Root Mean Square (RMS) of the difference between the measured and FE-calculated values over the ROI was used to evaluate the uncertainty of the measurements in the artificial experiments. For all four cases, parametric studies were performed to identify the largest possible cutoff frequency value leading to the maximum attainable accuracy in the strain.

4.6 Results

4.6.1 Performance evaluation

Results of the parametric studies are listed in Table 4.2, where the strain uncertainties and the corresponding optimum cutoff values are specified. The optimum parameters correspond to points where a compromise is achieved between two divergent error trends, namely, the displacement reconstruction error (decreasing as κ increases) and the systematic/noise-induced errors (increasing with κ) (Mortazavi *et al.*, 2013). As an example, the standard deviation of error in the measured vertical strain is plotted in Figure 4.6 as function of κ/L

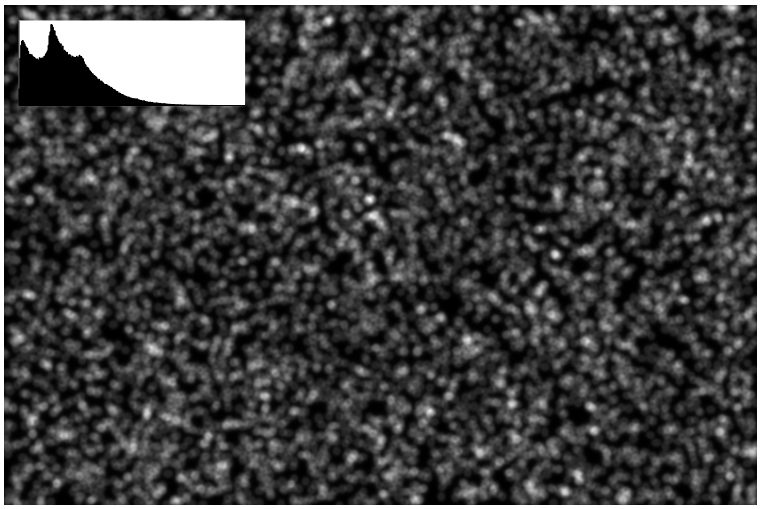

Figure 4.5 Synthetic textured image (1024×768 pixel; 12-bit gray-scale) and its histogram used for evaluation purposes.

for the synthetic and SEM images in the absence of noise at 6000× magnification. As can be seen from the curves, at $\kappa/L = 11\%$, the error from the SEM image reaches a minimum while the error from the synthetic image maintains its reducing trend. This higher performance is associated to the more enriched spectrum of the synthetic image that allows the increasing of κ without deteriorating the convergence of the reconstruction process. However, when noise is added to the images, the optimum cutoff values drop off considerably for both images leading to less accurate results that are smoothed out at the interfaces (see Figure 4.7).

Table 4.2 Parametric study on the selection of the optimum cutoff value for the artificial experiments

Artificial Test Case	κ/L (%)	strain RMS
2000× magnification		
Synthetic image	19	-0.0040
Simulated SEM image	10	-0.0067
Synthetic image (noisy)	3.5	-0.0101
Simulated SEM image (noisy)	2.5	-0.0121
6000× magnification		
Synthetic image	19	-0.0023
Simulated SEM image	11	-0.0032
Synthetic image (noisy)	3.5	-0.0058
Simulated SEM image (noisy)	2.5	-0.0074

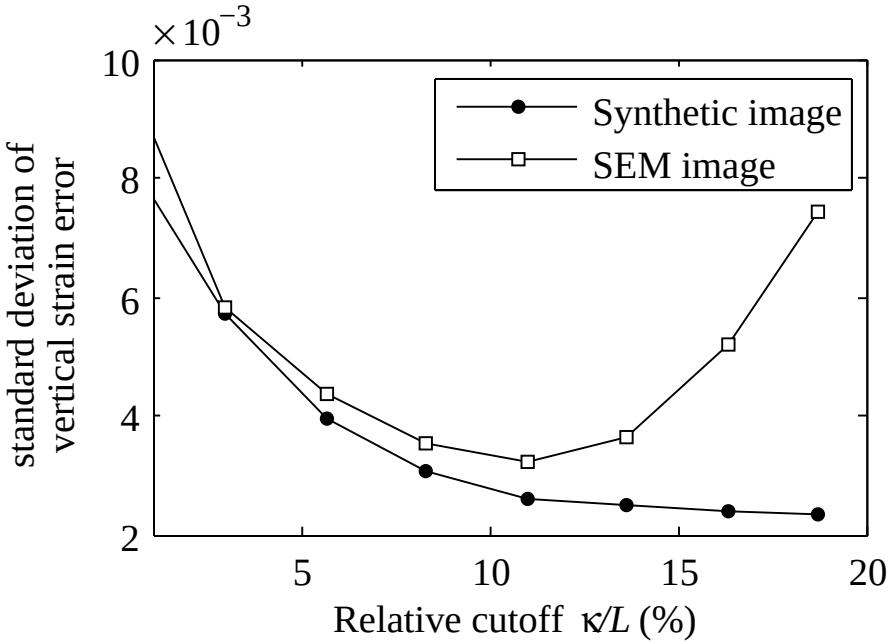

Figure 4.6 Measurement uncertainties for the vertical strain as function of κ/L for the synthetic and simulated SEM images at 6000× magnification in the absence of noise.

4.6.2 Measurements on the real composite

Measurements for the real experiments were carried out using $\kappa/L = 2.5\%$ ratio identified in the simulated experiments (see Table 4.2). The measured vertical displacement and strain fields for 2000× and 6000× magnifications are shown in Figure 4.8. Unlike in the simulated experiments, it is not possible to assess the accuracy of the real measurements on a point-by-point basis since there is no a priori known benchmark that completely represents the exact behavior of the material under loading. However, comparison of average strain values within individual phases reveals certain information about the certainty level of the measurements as well as the mechanical behavior of the composite (Table 4.3). Besides average values, standard deviations of strain fields within each phase are listed in Table 4.3 to measure the strain spatial variation levels in fiber and matrix (not to be confused with the strain uncertainty in Table 4.2). These values, when compared to the variation levels of FE strains particularly in the fiber region, signify that the performed measurements contain large oscillations that do not necessarily correspond to the mechanical response of the material in the ROI. Also, the results reported in (Canal *et al.*, 2012) are listed in Table 4.3 for comparison purposes.

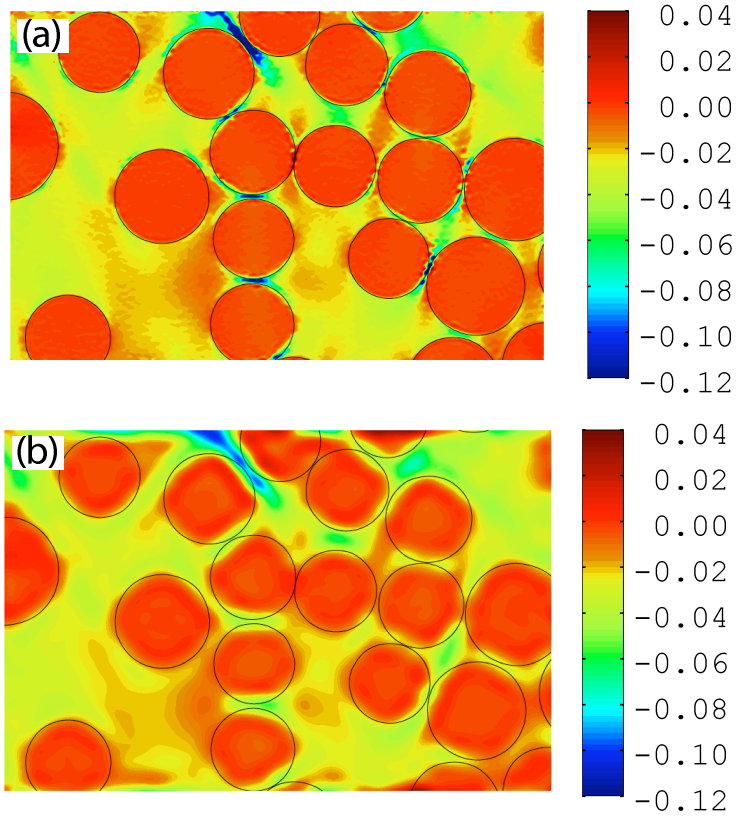

Figure 4.7 Vertical strain fields for the simulated measurements at 2000× magnification on two extreme cases, i.e. (a) the synthetic image without noise and (b) the SEM image with noise.

4.7 Discussion

Comparison of the resulted strain contours (Figure 4.8-b and -d) by the developed algorithm with those of the FE analyses (Figure 4.4-b, for example) reveals close similarities in the form of strain non-homogeneites in both fiber and matrix. The displacement iso-value bands in the measurements (Figure 4.8-a and -c) being curled around the fibers illustrate the reinforcing role of this constituent in the composite. This effect is better perceived from Figure 4.9, where the results from the FE analysis are compared with the experimental measurements along the section line sepecified in the figure. As seen from the plots, measurements present less concordance with FE results in some regions, which might be due to the 3D nature of the problem, inhomogeneities in mechanical properties of constituents or possible defects. As shown in Figure 4.9-c, this nonconformity between FE and measurements is almost reproduced in the same regions in the 6000× magnification, hence verifying the certainty level of the experimental measurements. The strain variations (Figure 4.9-b and d) are more amplified compared to those of displacement due to the differentiation. Considering

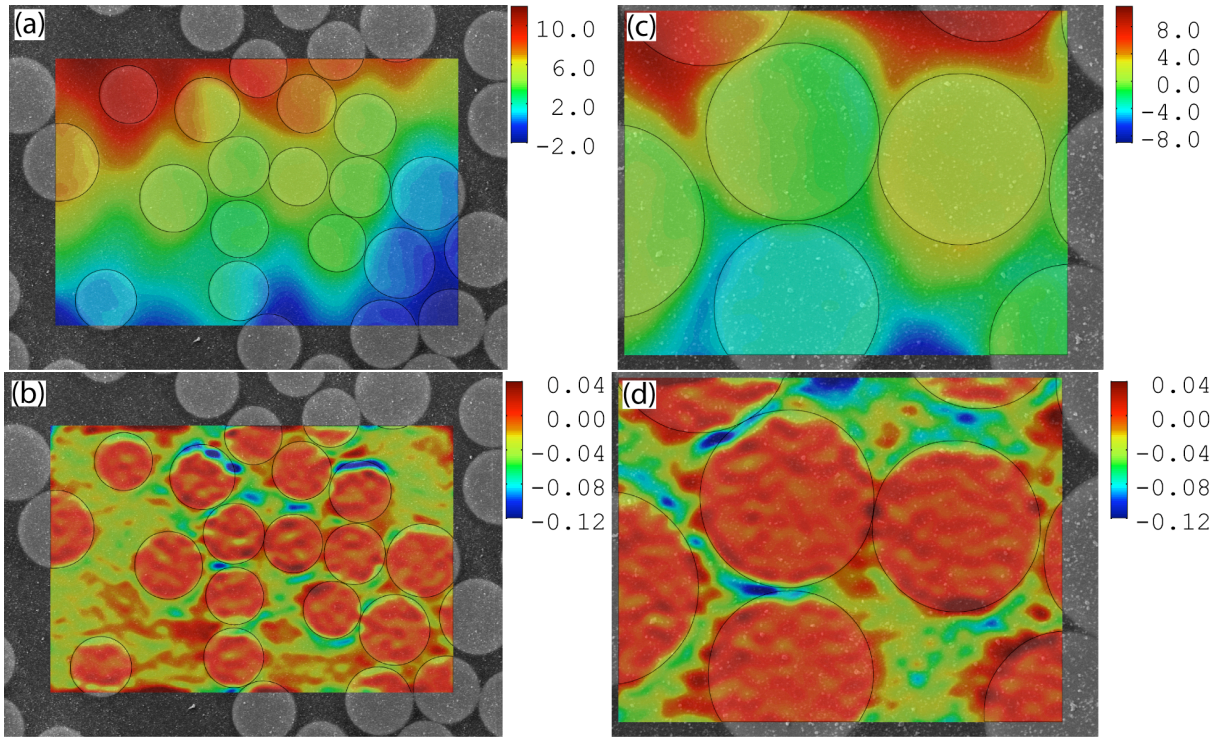

Figure 4.8 Measurement results for the real experiments. (a) and (c), the vertical displacement field (pixels) and (b) and (d), the vertical strain contours for 2000× and 6000× magnifications, respectively.

Table 4.3 Average values of strain at individual phases (comparison of real and artificial measurements with FE results). $\bar{\varepsilon}_m$ and $\bar{\varepsilon}_f$ denote the average strain values in the matrix and the fiber, respectively. STD[ ] operator calculates the standard deviation of the strain field within the individual phase specified in the operand.

	κ/L (%)	$\bar{\varepsilon}_m$	$STD[\varepsilon_m]$	$\bar{\varepsilon}_f$	$STD[\varepsilon_f]$
2000× magnification					
Simulated SEM image (noisy)	2.5	-0.0282	0.0139	-0.0057	0.0099
Real experiment	2.5	-0.0280	0.0121	-0.0065	0.0107
Results of Canal *et al.* (2012)	NA	-0.0237	-	-0.0094	-
FE	NA	-0.0306	0.0111	-0.0030	0.0047
6000× magnification					
Simulated SEM image (noisy)	2.5	-0.0306	0.0177	-0.0046	0.0074
Real experiment	2.5	-0.0353	0.0236	-0.0012	0.0131
Results of Canal *et al.* (2012)	NA	-0.0237	-	-0.0089	-
FE	NA	-0.0320	0.0191	-0.0037	0.0038

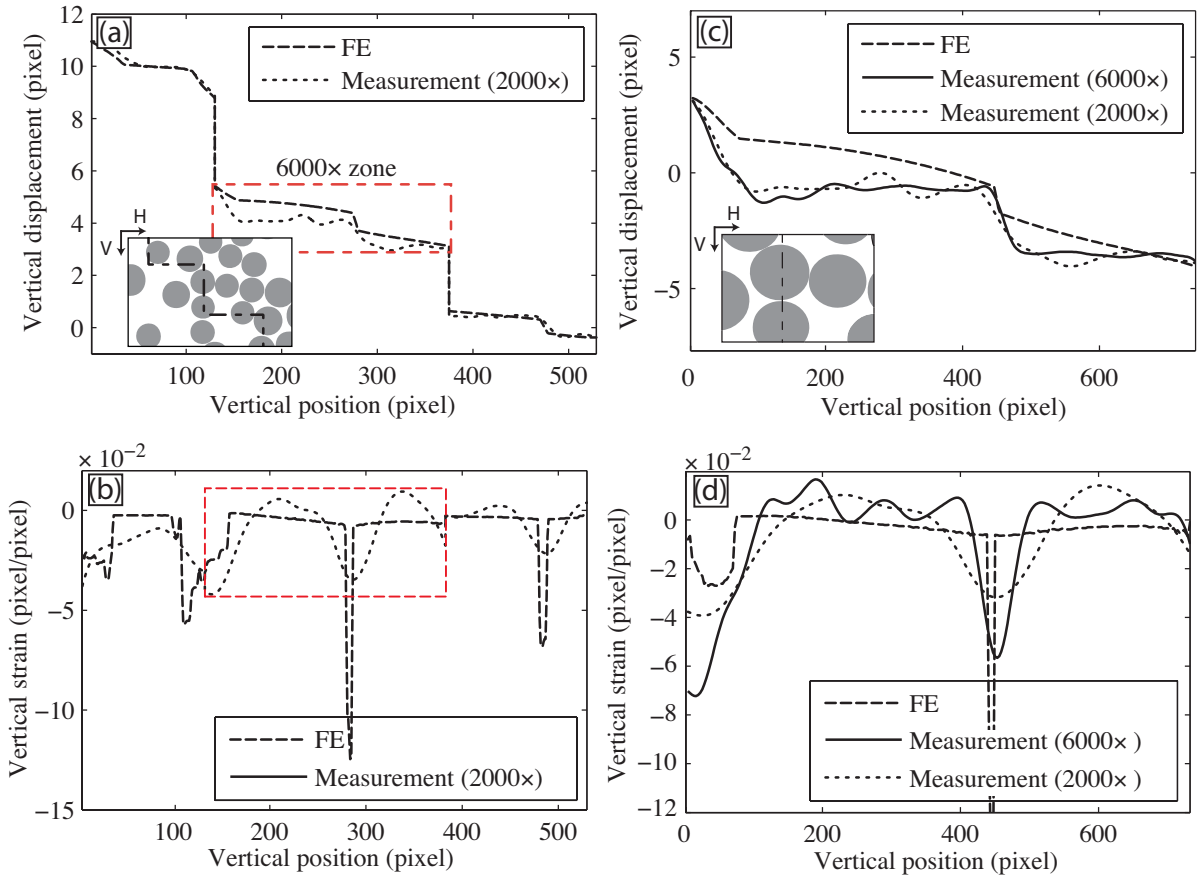

Figure 4.9 Measurement results plotted along the illustrated section line at 2000× (a and b) and 6000× magnifications (c and d). Note that the displacement plot at (c) for 2000× is rescaled to 6000× so as to compare the measurements between two scales.

the strain uncertainty values in artificial measurements (Table 4.2), one finds smaller errors in 6000× magnification when compared to the 2000× scale thanks to the higher resolution of the sampled surface (larger number of pixels), which led to a higher reconstruction accuracy for the same cutoff ratio (κ/L). Comparing the optimum cutoff ratios in the presence of noise between the synthetic and SEM images, one finds higher values for the synthetic image. This is explained by the higher intensity variations in the synthetic image that makes it less sensitive to the noise and hence allows for a higher cutoff wavenumber (Mortazavi *et al.*, 2013). The resulting strains from the synthetic image are therefore more accurate than those of the SEM images, which highlights the importance of texture quality (variations) in best exploiting the correlation algorithm for micro-scale measurements. As shown in Table 4.3, both the real and the artificial experiments with noise produced similar levels of uncertainties with respect to the FE strains (as far as average values are concerned). This identifies the noise effect, unsurprisingly (see (Hild and Roux, 2012), for example), as the main detrimental

factor on the accuracy of the measurements based on the SEM images. Comparing the average strains in 2000× magnification, one observes overestimation and underestimation of the average strain in fiber and matrix, respectively. These deviations are due to the fact that the measured displacements were not sufficiently rich in frequency contents and therefore unable to reconstruct the abrupt changes of the displacement gradients at the interfaces. Hence, displacement smoothing occurred that led to larger strains in the fiber and consequently lower values for the matrix. In contrast, one observes a significant reduction in the fiber strain at 6000× magnification and consequently larger average strain in the matrix. This variation is partly thanks to the higher magnification during the imaging, which led to more accurate strain measurements as demonstrated in the artificial experiments. Moreover, it would also imply that probably the fibers did not carry as much load as what was predicted by the FE analysis. Although the quality of the real strain measurements are not comparable to those obtained from the noiseless simulated experiments, one finds the current measurements more coherent with FE results when compared to the previous study (Canal *et al.*, 2012). For instance, the lower average strain in fiber is indicative of the higher reconstruction capability of the Fourier-based displacement field which further improved the accuracy of the strain near interface. This effect is even more noticeable in the 6000× magnification where the average fiber strain is reduced to -0.0012 compared to -0.0089 in the mentioned study.

4.8 Conclusion

Potential applications of a global image correlation approach to full-field measurements of microscale displacements and strains in composites were studied herein. The method consisted in retrieving displacement fields by a prior multiscale pattern matching based on B-Spline basis functions followed by a final estimation using an improved spectral approach. Thanks to the Fourier-based decomposition of the displacement field devised in the spectral approach, the algorithm showed a high potential for performing accurate measurements with high spatial non-homogoeneities in displacement/strain fields. Artificial and real experiments based on SEM images of composites at microscale were studied. The performance evaluations proved the high capability of the approach in reconstructing displacement/strain fields in the fiber/matrix scale. Furthermore, a priori assessment of the real measurements revealed that the existing noise in the SEM images was highly detrimental to the accuracy of the measured data. Indeed, the noise effect was estimated to reduce the reconstruction capacity of the approach to 23%, hence hindering the full use of the inherent potentials in the approach. Comparison of the measured strains within the real composite with the results of FE analysis as well as the measurements obtained in a previous related study revealed that the performed

measurements by the hybrid approach were more representative of the real mechanical state of the microstructure tested although they still contained significant deviations due to the high noise effects.

4.9 Acknowledgements

This research was funded by Fonds Québécois de la Recherche sur la Nature et les Technologies (FQRNT)-projets de recherche en équipe and the Canada Research Chair program (M. Lévesque and I. Villemure).

4.10 REFERENCES

ANZELOTTI, G., NICOLETTO, G. and RIVA, E. (2008). Mesomechanic strain analysis of twill-weave composite lamina under unidirectional in-plane tension. *Composites Part A: Applied Science and Manufacturing*, 39, 1294 – 1301.

BESNARD, G., HILD, F. and ROUX, S. (2006). "finite-element" displacement fields analysis from digital images: Application to portevin-le châtelier bands. *Experimental Mechanics*, 46, 789 – 803.

CANAL, L., GONZALEZ, C., MOLINA-ALDAREGUIA, J., SEGURADO, J. and LLORCA, J. (2012). Application of digital image correlation at the microscale in fiber-reinforced composites. *Composites Part A: Applied Science and Manufacturing*, 43, 1630–1638.

CHENG, P., SUTTON, M., SCHREIER, H. and MCNEILL, S. (2002). Full-field speckle pattern image correlation with B-Spline deformation function. *Experimental Mechanics*, 42, 344–352.

CHIVERS, K. F. and CLOCKSIN, W. F. (2000). Inspection of surface strain in materials using optical flow. *11 British Machine Vision Conference*. 392–401.

CLAIRE, D., HILD, F. and ROUX, S. (2004). A finite element formulation to identify damage fields: the equilibrium gap method. *International Journal for Numerical Methods in Engineering*, 61, 189–208.

FONSECA, J. Q. D., MUMMERY, P. M. and WITHERS, P. J. (2005). Full-field strain mapping by optical correlation of micrographs acquired during deformation. *Journal of Microscopy*, 218, 9–21.

FOUINNETEAU, M. and PICKETT, A. (2007). Shear mechanism modelling of heavy tow braided composites using a meso-mechanical damage model. *Composites Part A: Applied Science and Manufacturing*, 38, 2294 – 2306.

GEYMONAT, G. and PAGANO, S. (2003). Identification of mechanical properties by displacement field measurement: A variational approach. *Meccanica*, 38, 535–545.

GRÉDIAC, M. (2004). The use of full-field measurement methods in composite material characterization: interest and limitations. *Composites Part A: Applied Science and Manufacturing*, 35, 751 – 761.

GUILLEBAUD-BONNAFOUS, C., VASCONCELLOS, D., TOUCHARD, F. and CHOCINSKI-ARNAULT, L. (2012). Experimental and numerical investigation of the interface between epoxy matrix and hemp yarn. *Composites Part A: Applied Science and Manufacturing*, 43, 2046 – 2058.

HILD, F., RAKA, B., BAUDEQUIN, M., ROUX, S. and CANTELAUBE, F. (2002). Multi-scale displacement field measurements of compressed mineral-wool samples by digital image correlation. *Applied Optics*, 41, 6815–6828.

HILD, F. and ROUX, S. (2012). Comparison of local and global approaches to digital image correlation. *Experimental Mechanics*, 52, 1503–1519.

LECLERC, H., PÉRIÉ, J.-N., ROUX, S. and HILD, F. C. (2009). Integrated digital image correlation for the identification of mechanical properties. *Proceedings of the 4th International Conference on Computer Vision/Computer Graphics CollaborationTechniques*. Springer-Verlag, Berlin, Heidelberg, MIRAGE '09, 161–171.

LOMOV, S. V., IVANOV, D. S., VERPOEST, I., ZAKO, M., KURASHIKI, T., NAKAI, H., MOLIMARD, J. and VAUTRIN, A. (2008). Full-field strain measurements for validation of meso-fe analysis of textile composites. *Composites Part A: Applied Science and Manufacturing*, 39, 1218 – 1231.

MAKEEV, A., HE, Y., CARPENTIER, P. and SHONKWILER, B. (2012). A method for measurement of multiple constitutive properties for composite materials. *Composites Part A: Applied Science and Manufacturing*, 43, 2199 – 2210.

MORTAZAVI, F., LÉVESQUE, M. and VILLEMURE, I. (2013). Image-based continuous displacement measurements using an improved spectral approach. Manuscript accepted for publication on Jan. 29, 2013 in Strain.

MOUTRILLE, M.-P., DERRIEN, K., BAPTISTE, D., BALANDRAUD, X. and GÉDIAC, M. (2009). Through-thickness strain field measurement in a composite/aluminium adhesive joint. *Composites Part A: Applied Science and Manufacturing*, 40, 985–996.

NICOLETTO, G., MARIN, T., ANZELOTTI, G. and RONCELLA, R. (2011). Application of high magnification digital image correlation technique to micromechanical strain analysis. *Strain*, 47, e66–e73.

PASSIEUX, J.-C. and PÉRIÉ, J.-N. (2012). High resolution digital image correlation using proper generalized decomposition: Pgd-dic. *International Journal for Numerical Methods in Engineering*, 92, 531–550.

PÉRIÉ, J.-N., LECLERC, H., ROUX, S. and HILD, F. (2009). Digital image correlation and biaxial test on composite material for anisotropic damage law identification. *International Journal of Solids and Structures*, 46, 2388–2396.

RÉTHORÉ, J., ELGUEDJ, T., SIMON, P. and CORET, M. (2010). On the use of nurbs functions for displacement derivatives measurement by digital image correlation. *Experimental Mechanics*, 50, 1099–1116.

RÉTHORÉ, J., HILD, F. and ROUX, S. (2007). Shear-band capturing using a multiscale extended digital image correlation technique. *Computer Methods in Applied Mechanics and Engineering*, 196, 5016 – 5030.

ROUX, S., HILD, F. and BERTHAUD, Y. (2002). Correlation image velocimetry: A spectral approach. *Applied Optics*, 41, 108–115.

SUN, Y., PANG, J. H. L., WONG, C. K. and SU, F. (2005). Finite element formulation for a digital image correlation method. *Applied Optics*, 44, 7357 – 7363.

WAGNE, B., ROUX, S. and HILD, F. (2002). Spectral approach to displacement evaluation from image analysis. *Eur. Phys. J. AP*, 17, 247–252.

CHAPTER 5

ARTICLE 3: HIGH RESOLUTION MEASUREMENT OF INTERNAL FULL-FIELD DISPLACEMENTS AND STRAINS USING GLOBAL SPECTRAL DIGITAL VOLUME CORRELATION

F. Mortazavi, E. Ghossein, M. Lévesque, I. Villemure (2013). Submitted to *Optics and Lasers in Engineering* on February 19, 2013.

5.1 Abstract

Thanks to its ability to non-destructively access internal strains in materials, Digital Volume Correlation (DVC) is gaining growing interest from both experimental and theoretical mechanics communities. One important issue in the implementation of DVC is the considerable computational costs associated with the huge amount of data, which hinders the applications of the technique, especially for high-resolution displacement and strain measurements. In this paper, we propose an accurate global DVC approach based on a Fourier decomposition for the kinematic basis of the sought displacement field. The approach, referred to as IS-DVC, leads to an algorithm whose computational complexity is not considerably increased by increasing the number of Degrees of Freedom (DOF) of the kinematic basis, thus being computationally efficient using the Fast Fourier Transform (FFT). Artificial experiments have been used to evaluate the uncertainties of IS-DVC at high resolutions. Especially, displacement fields of 3D composites with spherical and non-aligned ellipsoidal particles at small scales were reconstructed. Resulting measurements revealed close similarities in terms of strain heterogeneities throughout the volume with the benchmark strains. Furthermore, it was shown that, in the presence of a discontinuity, the measurement uncertainties are not significantly affected, except for regions surrounding the discontinuity, hence validating the robustness of the reconstructed displacement field at large number of DOF.

5.2 Introduction

The Digital Image Correlation (DIC) technique has established itself as an important tool in the area of experimental mechanics for more than three decades (Sutton *et al.*, 1983). The valuable knowledge on the full-field displacements and strains that the technique provides in 2D has paved the way for interesting applications, such as mechanical properties (Grédiac, 2004; Geymonat and Pagano, 2003) and damage law (Périé *et al.*, 2009; Claire *et al.*, 2004)

identification, strain mapping (Bay, 1995; Hardisty and Whyne, 2009; Fonseca *et al.*, 2005), etc. The theoretical framework of DIC can be expanded into three dimensions, in which case it is called Digital Volume Correlation (DVC) (Bay *et al.*, 1999). DVC has found emerging applications in the past decade (Bay *et al.*, 1999; Zauel *et al.*, 2006; Lenoir *et al.*, 2007; Brémand *et al.*, 2008; Forsberg *et al.*, 2008; Forsberg and Siviour, 2009; Roux *et al.*, 2009; Barranger *et al.*, 2010; Hall *et al.*, 2010; Réthoré *et al.*, 2011) concurrently with the advances made in 3D imaging technologies, such as X-ray tomography and confocal microscopy. DVC allows for non-destructively evaluating displacements and strains *inside* materials. However, practical issues related to image acquisition and calculation have not only limited the applications of DVC, but also hindered the full exploitation of DIC's accuracy. Some of these issues are briefly discussed in the sequel:

• *Material limitation:* The choice of material for DVC is often dictated by the limitations of the employed imaging modality in revealing sufficient features for a reliable correlation. For example, in X-ray tomography, these features should stem from the difference between the capacity of the constituent phases in attenuating the emitted X-ray energy. Materials with cellular or granular structures have shown to be suitable for this purpose (Bay *et al.*, 1999; Roux *et al.*, 2008; Forsberg *et al.*, 2008; Forsberg and Siviour, 2009; Hall *et al.*, 2010). Metal matrix composites, such as nodular graphite cast iron (Réthoré *et al.*, 2011) or man-made composites (Bornert *et al.*, 2004), have also been studied. In the latter, small particles can be added during the elaboration process in order to create the required texture. These particles should be chosen so as not to significantly alter the overall mechanical properties (Bornert *et al.*, 2004).

• *Imaging artifacts:* Spurious features are inevitably introduced into volume images during the acquisition process. Such phenomena lead to perturbations in the measured displacements. Although image pre-processing partly alleviates the problem (Forsberg, 2008; Germaneau *et al.*, 2008), further regularization of the inverse problem might be required for high-resolution DVC (Leclerc *et al.*, 2011).

• *Algorithm implementations:* The first developments of DVC were based on local approaches (Bay *et al.*, 1999; Smith *et al.*, 2002; Verhulp *et al.*, 2004; Franck *et al.*, 2007). Later, global approaches were developed based on trilinear Finite Element (FE) shape functions (Roux *et al.*, 2008), as well as enriched FE shape functions for specimens containing cracks (Réthoré *et al.*, 2008b). However, as a result of the extension from 2D to 3D, the amount of data as well as the number of Degrees of Freedom (DOF) for DVC is significantly increased in both local and global approaches, when compared to their 2D counterparts. Consequently, DVC algorithms are highly demanding in terms of computer resources. This limitation has hindered the practical application of high-resolution DVC.

The present paper deals with the numerical aspects of DVC, specifically as far as high-resolution DVC [1] is concerned. We propose a global approach based on Fourier basis functions referred to as Improved Spectral DVC (IS-DVC) hereinafter. Being an extension to 3D of the Improved Spectral Approach (ISA) (Mortazavi *et al.*, 2013; Wagne *et al.*, 2002; Roux *et al.*, 2002), IS-DVC makes use of Fast Fourier Transform (FFT) to convert the computationally cumbersome system of equations in Fourier domain to an explicit equation for the displacement field in the spatial domain. The expression thus found can be evaluated quite efficiently. The interesting feature of the approach lies in the fact that the complexity of the correlation procedure does not significantly increase for larger number of DOF.

The theoretical framework of the IS-DVC is explained in Section 5.4 and 5.4.1. The approach is then evaluated on a series of artificial experiments. Simulated experiments requiring high resolution DVC, such as composite materials at micro-scale were considered, details of which are explained in Section 5.5. Finally, the results and discussion are presented in Section 5.6.

5.3 Background

5.3.1 Concept of pattern matching

Let $f(\mathbf{x})$ and $g(\mathbf{x})$ represent the intensity functions of spatial coordinates $\mathbf{x} = (x, y, z)$ corresponding to the undeformed and deformed images, respectively. In ideal conditions, these two configurations are correlated through a mapping of coordinates expressed by the following relation:

$$f(\mathbf{x}) = g(\breve{\mathbf{x}}) \quad \text{where} \tag{5.1a}$$

$$\breve{\mathbf{x}} = \mathbf{x} + \mathbf{u}_{\text{exact}}(\mathbf{x}) \tag{5.1b}$$

where $\mathbf{u}_{\text{exact}}(\mathbf{x})$ is the displacement vector field resulting from the applied loads. The exact displacement, in the Volume of Interest (VOI), is estimated by a mathematical function with specified Degrees of Freedom (DOF), i.e.:

$$\mathbf{u}_{\text{exact}}(\mathbf{x}) \approx \mathbf{u}(\mathbf{x}; \mathbf{p}) \tag{5.2}$$

where $\mathbf{p}$ is the set of parameters representing the DOF that should be determined from pattern matching. The pattern matching consists in finding the parameters that minimize

1. Throughout this paper, the resolution of a DVC algorithm refers to that of displacement and strain measurements. In this sense, the resolution is defined as "the smallest change in a quantity being measured that causes a perceptible change in the corresponding indication." (ISO/IEC guide (ISO/IEC guide 99, 2007))

the gap between $f(\mathbf{x})$ and $g(\check{\mathbf{x}})$. This can be expressed as follows:

$$\mathbf{p_{opt}} = \arg\min_{\mathbf{p}\in\mathcal{A}}\{\int_{\mathrm{VOI}} [f(\mathbf{x}) - g(\mathbf{x}+\mathbf{u}(\mathbf{x};\mathbf{p}))]^2\,\mathbf{dx}\} \tag{5.3}$$

where $\mathcal{A}$ denotes the set of admissible choices for $\mathbf{p}$ and the integrand is called the *squared correlation residuals* that should be minimized. For the sake of simplicity, the above formulation is written assuming the intensity functions are continuous, hence the use of integral operators. In practice, the discrete image functions are interpolated using proper interpolation methods (Lehmann *et al.*, 1999; Unser *et al.*, 1993a,b) in order to perform the optimization at sub-pixel positions.

5.3.2 Resolution strategy

Different approaches of DIC depend, in the first place, on how the sought displacement field is formulated. Nevertheless, no matter how it is formulated, the displacement fields for different approaches can be expressed as the linear combination of several chosen basis functions (Hild and Roux, 2012), which can be expressed in the form of the following vector product:

$$\mathbf{u}(\mathbf{x};\mathbf{p}) = \begin{bmatrix} \psi_1(\mathbf{x}) & \psi_2(\mathbf{x}) & \cdots & \psi_K(\mathbf{x}) \end{bmatrix} \begin{bmatrix} \boldsymbol{\upsilon}_1 \\ \boldsymbol{\upsilon}_2 \\ \vdots \\ \boldsymbol{\upsilon}_K \end{bmatrix} \tag{5.4a}$$

$$\text{where} \quad \mathbf{p} \equiv \{\boldsymbol{\upsilon}_n | n = 1, 2, \cdots, K\} \tag{5.4b}$$

$\boldsymbol{\upsilon}_n$ are the sequence of unknown 3×1 (or 2×1 in DIC) vectors associated with basis functions $\psi_n(\mathbf{x})$ and K is the total number of basis functions. Except for some approaches (for example in (Franck *et al.*, 2007)), a Newton iterative strategy is often used to solve the problem (5.3). The iterations start with an initial solution $\mathbf{p}^{(0)}$ (leading to $\mathbf{u}^{(0)}$), at iteration i, $g(\mathbf{x}+\mathbf{u})$ is corrected for $\mathbf{u}^{(i-1)}$ and the new solution lies in finding the increment $\delta\mathbf{u}^{(i)} = \mathbf{u}^{(i)} - \mathbf{u}^{(i-1)}$. It is assumed that the sought increment, $\delta\mathbf{u}^{(i)}$, is small enough so that one can linearize $g\left(\mathbf{x}+\mathbf{u}^{(i-1)}(\mathbf{x}) + \delta\mathbf{u}(\mathbf{x})\right)$ as:

$$g\left(\mathbf{x}+\mathbf{u}^{(i-1)}(\mathbf{x}) + \delta\mathbf{u}(\mathbf{x})\right) \approx g\left(\mathbf{x}+\mathbf{u}^{(i-1)}(\mathbf{x})\right) + \nabla_{\mathbf{x}}^T g\left(\mathbf{x}+\mathbf{u}^{(i-1)}(\mathbf{x})\right)\delta\mathbf{u}(\mathbf{x}) \tag{5.5a}$$

$$\text{provided that } \forall\mathbf{x},\ \|\delta\mathbf{u}(\mathbf{x})\| < \|\boldsymbol{\eta}\|. \tag{5.5b}$$

where $\boldsymbol{\eta}$ is a small real vector, $\nabla_{\mathbf{x}}$ denotes the gradient operator with respect to vector $\mathbf{x}$, and $\square^T$ indicates the vector transpose. Therefore, the First-order Optimality for the problem (5.3) is written as:

$$\nabla_{\boldsymbol{v}_n}\left[\int_{\text{VOI}}\left[f(\mathbf{x})-\breve{g}^{(i-1)}(\mathbf{x})-\nabla_{\mathbf{x}}^T\breve{g}^{(i-1)}(\mathbf{x})\delta\mathbf{u}(\mathbf{x};\mathbf{p})\right]^2\mathbf{dx}\right]=\mathbf{0}\quad n=1,2,\cdots,K \tag{5.6}$$

and

$$\breve{g}^{(i)}(\mathbf{x})=g\left(\mathbf{x}+\mathbf{u}^{(i)}(\mathbf{x})\right) \tag{5.7}$$

By applying the differentiation and after simplifications, equation (5.6), is turned into:

$$\int_{\text{VOI}}\left(\nabla_{\mathbf{x}}^T\breve{g}^{(i-1)}(\mathbf{x})\begin{bmatrix}\psi_1(\mathbf{x}) & \psi_2(\mathbf{x}) & \cdots & \psi_K(\mathbf{x})\end{bmatrix}\begin{bmatrix}\boldsymbol{v}_1\\ \boldsymbol{v}_2\\ \vdots\\ \boldsymbol{v}_K\end{bmatrix}\psi_n(\mathbf{x})\nabla_{\mathbf{x}}\breve{g}^{(i-1)}(\mathbf{x})\right)\mathbf{dx}$$
$$=\int_{\text{VOI}}\Big(\left(f(\mathbf{x})-\breve{g}^{(i-1)}(\mathbf{x})\right)\psi_n(\mathbf{x})\nabla_{\mathbf{x}}\breve{g}^{(i-1)}(\mathbf{x})\Big)\mathbf{dx}\qquad n=1,2,\cdots,K \tag{5.8}$$

The above equation can be reorganized into a system of linear equations, i.e.

$$\begin{bmatrix}\mathbf{J}_{11} & \mathbf{J}_{12} & \cdots & \mathbf{J}_{1K}\\ \mathbf{J}_{21} & \ddots & & \vdots\\ \vdots & & \ddots & \vdots\\ \mathbf{J}_{K1} & \cdots & \cdots & \mathbf{J}_{KK}\end{bmatrix}\begin{bmatrix}\boldsymbol{v}_1\\ \boldsymbol{v}_2\\ \vdots\\ \boldsymbol{v}_K\end{bmatrix}=\begin{bmatrix}\boldsymbol{\rho}_1\\ \boldsymbol{\rho}_2\\ \vdots\\ \boldsymbol{\rho}_K\end{bmatrix} \tag{5.9a}$$

where $\mathbf{J}_{mn}$ and $\boldsymbol{\rho}_m$ are 3×3 (or 2×2) and 3×1 (or 2×1) matrices calculated from the following equations:

$$\mathbf{J}_{mn}=\int_{\text{VOI}}\Big(\left(\nabla_{\mathbf{x}}\breve{g}^{(i-1)}\otimes\nabla_{\mathbf{x}}\breve{g}^{(i-1)}\right)(\mathbf{x})\psi_m(\mathbf{x})\psi_n(\mathbf{x})\Big)\mathbf{dx} \tag{5.9b}$$

$$\boldsymbol{\rho}_m=\int_{\text{VOI}}\Big(\left(f(\mathbf{x})-\breve{g}^{(i-1)}(\mathbf{x})\right)\psi_m(\mathbf{x})\nabla_{\mathbf{x}}\breve{g}^{(i-1)}(\mathbf{x})\Big)\mathbf{dx} \tag{5.9c}$$

respectively, and $\otimes$ denotes the dyadic product. Equation (5.9a) is considered as the governing equation for the gradient-based pattern matching.

5.3.3 Spectral approach

Roux *et al.* (2002) and Wagne *et al.* (2002) introduced a very appealing approach based on the Fourier decomposition of the sought displacement field in 1D and 2D, respectively. In this framework, the displacement field was expressed as:

$$\mathbf{u}(\mathbf{x}) = \sum_n \boldsymbol{\upsilon}_n \exp(\hat{\imath}\boldsymbol{\omega}_n \cdot \mathbf{x}) \tag{5.10a}$$

where

$$\boldsymbol{\omega}_n \in \left\{ \left(\frac{p\pi}{L}, \frac{q\pi}{L}\right) \middle| \begin{array}{c} n = 2Mq + p \\ p, q \in \mathbb{Z} \\ -M \leq p, q \leq M-1 \end{array} \right\}, \tag{5.10b}$$

L denotes the half-width of the Region of Interest (ROI) and $M \leq L$ implies that only Fourier coefficients within a square of size $2M \times 2M$ were used to estimate the displacement field (i.e. $K = 4M^2$). In the extreme case where this square extends over the whole ROI size (i.e. $M = L$), the displacement field is aimed to be exactly reconstructed. However, this is not possible due to the ill-posed nature of the inverse problem. In their study, Wagne *et al.* (2002) showed that $M \ll L$ in order for the approach to lead to meaningful results. It is easy to show that with the chosen formulation, matrix elements of the governing equation, i.e. equations (5.9b) and (5.9c), turn into the following Fourier transforms:

$$\mathbf{J}_{mn} = \mathcal{F}\left\{ \left(\nabla_{\mathbf{x}} \breve{g}^{(i-1)} \otimes \nabla_{\mathbf{x}} \breve{g}^{(i-1)} \right) \right\}_{[-m-n]} \qquad := \widetilde{\mathbf{J}}_{[-m-n]} \tag{5.11a}$$

$$\boldsymbol{\rho}_m = \mathcal{F}\left\{ \left(f - \breve{g}^{(i-1)} \right) \nabla_{\mathbf{x}} \breve{g}^{(i-1)} \right\}_{[-m]} \qquad := \widetilde{\boldsymbol{\rho}}_{[-m]} \tag{5.11b}$$

where the Fourier transform of a function $h(\mathbf{x})$ is defined as:

$$\mathcal{F}\{h\}_{[m]} = \int_{\mathrm{ROI}} h(\mathbf{x}) \exp\left(-\hat{\imath}\boldsymbol{\omega}_m \cdot \mathbf{x}\right) \mathbf{dx} \tag{5.12}$$

(note that only the Fourier terms within the $2M \times 2M$ square are calculated in equations (5.11a) and (5.11b)). Therefore, equation (5.9a) can be written in the following form using the Einstein notation:

$$\widetilde{\mathbf{J}}_{[m-n]} \boldsymbol{\upsilon}_n = \widetilde{\boldsymbol{\rho}}_{[m]} \quad \text{summation over } n \tag{5.13}$$

The left-hand side of the above equation is a convolution product. The main interest of the spectral approach lies in the fact that instead of directly solving equation (5.13) in the frequency domain, one may bring the calculations back to the spatial domain. Thus, the

convolution operation turns into a simple matrix product in the real space. In doing so, equation (5.13) is transformed to the following practical form:

$$\left(\widehat{\left(\nabla_{\mathbf{x}}\breve{g}\otimes\nabla_{\mathbf{x}}\breve{g}\right)}^{(i-1)}\cdot\delta\mathbf{u}^{(i)}\right)(\mathbf{x})=\widehat{\left((f-\breve{g})\nabla_{\mathbf{x}}\breve{g}\right)}^{(i-1)}(\mathbf{x}) \tag{5.14}$$

where $\widehat{\square}$ denotes low-pass filtering in the frequency domain by preserving only $2M\times 2M$ coefficients. One faces here a 2×2 linear algebraic system for each point in the space. Such a system is analytically solved giving rise to two explicit expressions for the estimated displacement components. The main computational burden is performing a forward and a backward FFT to apply the Fourier low-pass filtering.

Wagne *et al.* (2002) used multiscale iterations for large displacement magnitudes (Besnard *et al.*, 2006). The developed strategy showed high reconstruction capacities while having drastically low computational costs. However, their approach suffered from a limitation stemming from the periodic nature of the utilized basis functions, i.e. the approach highly relied on periodic displacement fields and periodic images; a condition that is rarely met in real experiments. Meanwhile, this limitation was shown to be alleviated in 1D by using prior displacement correction using measurements based on a linear displacement model (Roux *et al.*, 2002) .

5.4 IS-DVC

In the IS-DVC, the 2D framework of the spectral approach is extended to 3D while improving on the accuracy and the functionality of the approach for practical applications. These improvements were completely elaborated in the ISA (Mortazavi *et al.*, 2013) by the authors and will be briefly formulated here in 3D. The number of DOF of the sought displacement field in the spectral approach, equation (5.10a), was determined by K (total number of basis functions). Alternatively, it can be considered as a box lowpass filter, which passes only $2M\times 2M$ basis functions. In the ISA (Mortazavi *et al.*, 2013), this filter was replaced with a Gaussian filter, which was shown to significantly improve the accuracy of the measurements. Considering the Gaussian filter as:

$$H_n^{(\kappa)}=\exp\left(-\frac{L^2\|\boldsymbol{\omega}_n\|^2}{2\pi^2\kappa^2}\right), \tag{5.15}$$

the sought displacement field is expressed in the following form:

$$\mathbf{u}(\mathbf{x})=\sum_n H_n^{(\kappa)}\boldsymbol{\upsilon}_n\exp\left(\hat{\imath}\boldsymbol{\omega}_n\cdot\mathbf{x}\right) \tag{5.16}$$

$$\boldsymbol{\omega}_n \in \left\{ \left(\frac{p\pi}{L}, \frac{q\pi}{L}, \frac{s\pi}{L} \right) \middle| \begin{array}{c} n = 4L^2 s + 2Lq + p \\ p, q, s \in \mathbb{Z} \\ -L \leq p, q, s \leq L-1 \end{array} \right\}, \tag{5.17}$$

where κ is the cutoff wavenumber corresponding to the Gaussian filter. Since the formulation of IS-DVC is defined in 3D, $\mathbf{u}$, $\boldsymbol{\upsilon}_n$ and $\boldsymbol{\omega}_n$ are all 3×1 vector fields and the VOI contains $2L \times 2L \times 2L$ voxels. Similar to the spectral approach, one should have $\kappa \ll L$ to ensure the accuracy of the results (Mortazavi *et al.*, 2013). Proceeding with the improved formulation, one obtains the same governing equation (5.14) as obtained in the spectral approach. Here, $\widehat{\square}$ denotes low-pass filtering in the frequency domain using the mask $H^{(\kappa)}$. As in the ISA (Mortazavi *et al.*, 2013), the following modification, inspired by the Hessian modification in nonlinear optimization (Nocedal and Wright, 2000), ensures that the modified dyadic tensor is always positive definite:

$$\forall \mathbf{x}, \quad \mathbf{B}^{(i)}(\mathbf{x}) := \left(\widehat{\nabla_{\mathbf{x}} \breve{g} \otimes \nabla_{\mathbf{x}} \breve{g}} \right)^{(i)} (\mathbf{x}) + \tau^{(i)}(\mathbf{x}) \mathbf{I} \tag{5.18}$$

where $\mathbf{I}$ is the identity tensor and τ is defined as:

$$\tau^{(i)}(\mathbf{x}) = \max \left\{ 0, \delta_0 - \lambda_1^{(i)}(\mathbf{x}) \right\} \tag{5.19}$$

where δ_0 is a positive real number (typical value 10^{-2}) and $\lambda_1^{(i)}(\mathbf{x})$ denotes the smallest eigenvalue of the dyadic tensor field at iteration i. Therefore, equation (5.14) is modified into the following equation:

$$\left(\mathbf{B}^{(i-1)} \cdot \delta \mathbf{u}^{(i)} \right) (\mathbf{x}) = \left(\widehat{(f - g) \nabla_{\mathbf{x}} \breve{g}} \right)^{(i-1)} (\mathbf{x}) \tag{5.20}$$

Provided that δ_0 is small compared to the average values of λ_1, the resulting displacements are meaningful enough to reduce the dissimilarity objective, equation (5.3). Equation (5.20) is evaluated in 3D. For example, for the dyadic product one deals with the following tensor field:

$$\left(\widehat{\nabla_{\mathbf{x}} g \otimes \nabla_{\mathbf{x}} g} \right) (\mathbf{x}) = \begin{pmatrix} \widehat{g_{,x}^2} & \widehat{g_{,x} g_{,y}} & \widehat{g_{,x} g_{,z}} \\ \widehat{g_{,y} g_{,x}} & \widehat{g_{,y}^2} & \widehat{g_{,y} g_{,z}} \\ \widehat{g_{,z} g_{,x}} & \widehat{g_{,z} g_{,y}} & \widehat{g_{,z}^2} \end{pmatrix} (\mathbf{x}). \tag{5.21}$$

where $g_{,i\ (i=x,y,z)}$ denotes the partial derivatives of g with respect to direction i. The analytical solution to the 3×3 linear system (5.20) leads to three explicit expressions for the displacement components that can be evaluated for every voxel. Aside from the additional computational burden dictated by the 3D operations (e.g. 3D-DFT, arithmetic operations and sub-pixel

interpolation), the solution to the above 3×3 system involves considerably higher number of operations when compared to the 2×2 version in 2D. However, these operations are performed sequentially and therefore can be carried out efficiently. Moreover, thanks to the FFT advantages, the 3D-DFT operations can be also performed with drastically less computational efforts, thus making the algorithm suitable for 3D applications.

In the iterative procedure, the cutoff wavenumber, κ, was also gradually increased so that it reached its presumed value at final iterations, thus correcting for low-frequency terms in the displacement before proceeding to compute the high-frequency terms. Therefore, at iteration i, the displacement field $\mathbf{u}^{(i)}$ was corrected as:

$$\mathbf{u}^{(i)} = \mathbf{u}^{(i-1)} + \delta\mathbf{u}^{(i,\kappa)} \tag{5.22}$$

where $\delta\mathbf{u}^{(i,\kappa)}$ was calculated from equation (5.20) using te current value of κ. The algorithm decides to augment κ when the Root Mean Square (RMS) of the correction $\delta\mathbf{u}^{(i,\kappa)}$, denoted by $\sigma_{\delta\mathbf{u}}$, becomes inferior to 10^{-3}. This criterion is referred to as the stagnation measure. A slight variation with respect to the ISA was used herein to systematically stop the algorithm. The criterion was based on the observed trend of the reduction in $\sigma_{\delta\mathbf{u}}$ as a function of κ, which is illustrated in Figure 5.1 As seen from the trend, there is a jump in $\sigma_{\delta\mathbf{u}}$ as a result of an increase in κ, which is due to the increased DOF in the sought displacement field allowing for more variations (hence a higher RMS) and probably a more enriched reconstruction. However, this jump decreases with a quasi-logarithmic decay as κ increases, which means that the added DOF have less impact on the accuracy of the measurement. Thus, there is a risk that the κ-induced reduction of the uncertainty is overlaid by noise- and interpolation-induced errors. Therefore, the algorithm was set to stop when $\sigma_{\delta\mathbf{u}}$ at the jump corresponding to κ became inferior to 10^{-3} (see (Mortazavi *et al.*, 2013) for further details on the algorithm).

5.4.1 Other variations with respect to ISA

Prior correction for non-periodic displacements

The major utility of a two-fold correlation, is to remove the limitation imposed by the Fourier-based decomposition of the displacement field in the spectral approach. This was shown by Roux et al. (Roux *et al.*, 2002) and Mortazavi et al. (Mortazavi *et al.*, 2013) to efficiently operate for non-periodic images and displacement fields, in 1D and 2D, respectively. In the ISA (Mortazavi *et al.*, 2013), the authors used a local approach followed by 2D surface fitting to roughly estimate the non-periodic part of the displacement field. However, due to the additional computational burden associated with the surface fitting algorithm, and for the sake of simplicity in the evaluation of the presented examples, a global approach based

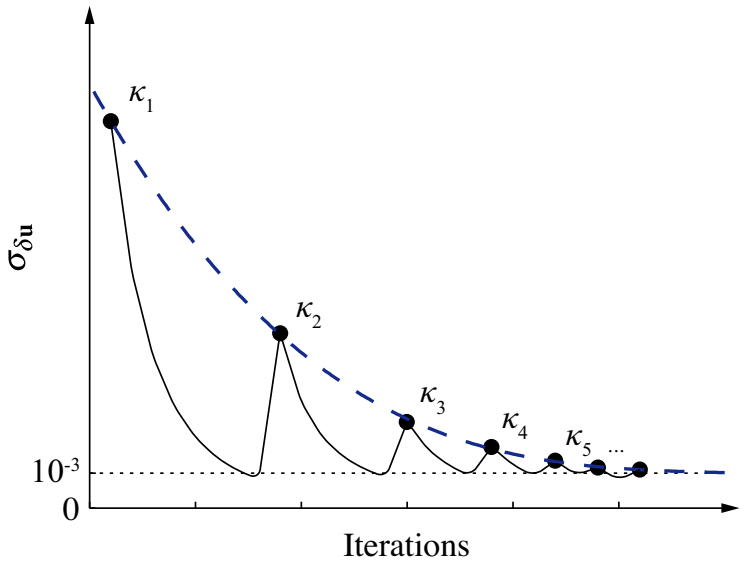

Figure 5.1 Illustration of the general trend of $\sigma_{\delta \mathbf{u}}$ as a function of iterations. The jumps correspond to an increase of κ due to the fulfillment of the stagnation measure. It can be seen that these jumps decrease logarithmically, as illustrated by the dashed line.

on an affine transformation for the formulation of the non-periodic part of the displacement field was considered (as previously done in (Roux *et al.*, 2002) for 1D images). In doing so, the initial solution $\mathbf{u}^{(0)}$ in IS-DVC is of the following form:

$$\mathbf{u}^{(0)} = (\mathbf{R_0} + \mathbf{E_0}) \cdot \mathbf{x} + \mathbf{t_0} \tag{5.23}$$

where $\mathbf{R_0}$ and $\mathbf{E_0}$ are the homogeneous rotation and strain tensors, respectively, and $\mathbf{t_0}$ is the rigid body translation vector. The transform involves 12 DOF, which are found by solving the pattern matching problem (5.3) through nonlinear optimization.

5.5 Simulated experiments

Three complex artificial experiments were performed to evaluate the functionality of IS-DVC. In all experiments, 8-bit 128^3 voxel synthetic volume images were artificially transformed to a priori known deformed states using displacement fields simulated from mechanical analyses (referred to as exact displacement fields hereinafter). The synthetic images were generated using the Fractals theory, namely, "Brownian motion" (Barnsley *et al.*, 1988). This choice allowed for fast generation of 3D images with random but correlated 3D textures. Figure 5.2 shows a typical volume image used in this study. The root mean square of the error between the measured quantities (displacement/strain) and their exact values was calculated

as the measurement uncertainty of the corresponding quantity. To this end, the measured values within 10 voxels near the volume edges were excluded from the calculation to avoid any boundary errors. In the first two examples, two different composite geometries were considered, namely, a matrix reinforced by randomly distributed spherical particles in the first case (example I) and in the second case, by randomly distributed ellipsoidal fibers (example II). To this end, an in-house MATLAB code from another study by the authors (Ghossein and Lévesque, 2012) was used to generate the mentioned random microstructures for any given size and volume fraction. The geometries are illustrated in Figure 5.4(a) and 5.5(a). The elastic response of the obtained microstructures under 2% applied compressive strain in z direction was subsequently calculated using an FFT-based numerical method (Moulinec and Suquet, 1998). Table 5.1 lists the properties used for generating the artificial data (geometry and mechanical properties) for both composites. In the third example, a displacement field with a discontinuity was considered, namely, that of the analytical mode I 2D crack. This example is interesting in the sense that the discontinuous displacement field requires a large number of DOF (high frequency bases) to be approximated with a continuous displacement field expressed as per a Fourier expansion. This example is useful to assess the potentials and limitations of the presented approach. It should be noted that the accurate measurement of discontinuous displacement fields is not within the scope of the present approach as it would require further considerations to deal with such cases. The reader is referred to other approaches specifically tailored for cracked specimens (Fagerholt *et al.*, 2013; Réthoré *et al.*, 2008b,a). We used the following discontinuous function for the z-component of the preset displacement field, w, according to the theory of linear elastic fracture mechanics:

$$w(x, r, \theta) = C_{\mathrm{I}}\sqrt{r}\left[\left(\eta + \frac{1}{2}\right)\sin\frac{\theta}{2} - \frac{1}{2}\sin\frac{3\theta}{2}\right] \tag{5.24}$$

Table 5.1 Properties used for the generation of composites with spherical (example I) and ellipsoidal particles (example II) used in the artificial experiments. Subscripts m and p refer to matrix and particle, respectively. E denotes the elastic modulus and ν is the poisson ratio. The particle volume fraction is denoted by v.f.

	E_m (GPa)	E_p (GPa)	ν_m	ν_p	v.f.(%)	aspect ratio	size ratio ($d^\dagger = L/r$)
Example I	25	5	.2	.3	10	1	2.5
Example II	50	5	.2	.3	5	20	16

$^\dagger d$ is defined as the ratio of image half-length (L) to the smallest particle radius (r), which gives an estimation of the particle voxel-size in the volume image (see section 5.6).

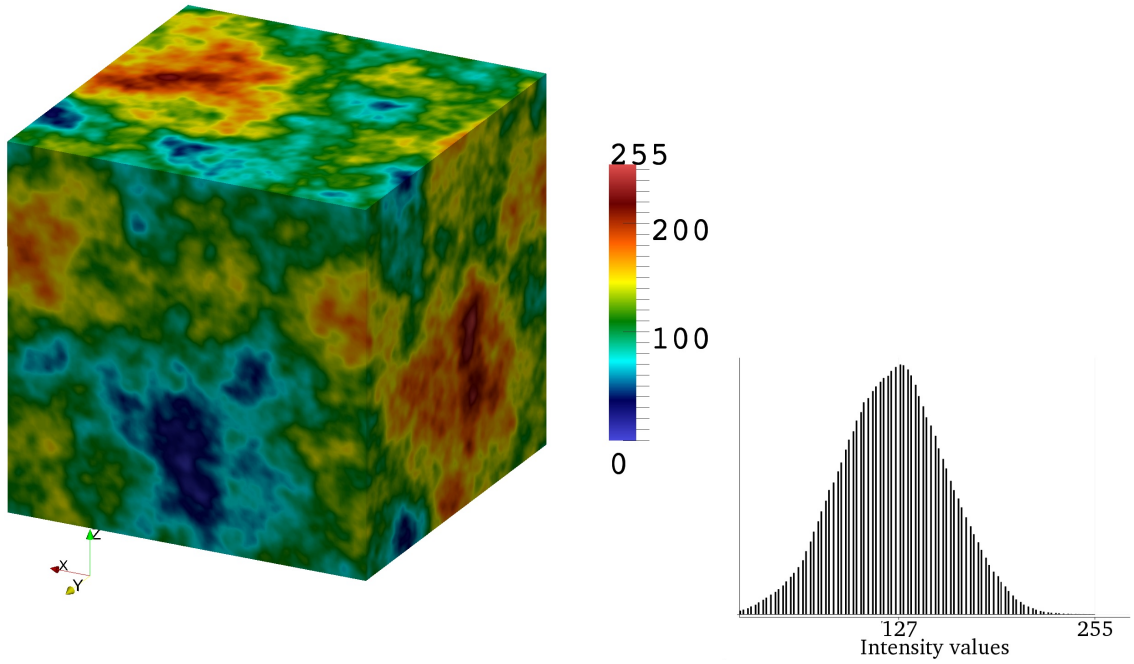

Figure 5.2 Synthetic grayscale volume image ($128 \times 128 \times 128$ voxels, 8-bit) used for the artificial experiments as well as its histogram. A different colormap was used here for illustrative purposes.

where C_{I} and η are mechanical constants and (r, θ) are the polar coordinates centered at the crack tip in the yz plane (crack oriented along $\theta = \pi$).

The artificial transformations of the undeformed volume images were performed using the transformation of their Fourier series, hence avoiding any interpolation bias at this level of experiments. The tricubic B-spline interpolation scheme (Unser *et al.*, 1993b) was used for sub-pixel measurement since it induces relatively small interpolation bias (Mortazavi *et al.*, 2013).

5.6 Results and discussion

5.6.1 Examples I and II: artificial composites

Figure 5.3(a) and 5.3(c) show the evolution of displacement uncertainty as a function of the iterations, for both examples. The measurements stopped at $\kappa = 9$ and $\kappa = 10$ for examples I and II, respectively, according to the criteria of section 5.4. The evolution of these criteria are plotted in Figure 5.3(b) and 5.3(d) as functions of the characteristic subset length

introduced in (Mortazavi *et al.*, 2013) for ISA, i.e.:

$$\ell = \frac{2L}{\alpha\kappa} \tag{5.25}$$

where ℓ is the characteristic subset length and $\alpha \approx 1.05 - 1.25$ ($\alpha = 1.05$ was used for the aforementioned plots). This parameter relates the cutoff wavenumber in the frequency domain to a more tangible measure of resolution in the spatial domain. As shown in these plots, at final iterations, the stopping criterion reached the value 10^{-3}, where the algorithm systematically stops. Also, one notes the power-law fit for the reduction trend of the stopping criterion, which confirms the validity of the notions discussed in section 5.4. It is worth noting that for every image correlation algorithm, successful measurements consist in achieving a balance between two divergent trends, namely, uncertainty reduction thanks to increasing number of DOF (i.e. smaller characteristic lengths) and uncertainty rise due the loss of intensity variations as a result of smaller characteristic lengths. In this sense, decision-making criteria, e.g. the stopping and stagnation measures herein, become key factors in the final accuracy of the measurements. The exact tradeoff point (i.e. the minimum uncertainty as a function of κ) for examples I and II was identified as 0.0034 and 0.0038 voxels, respectively, ocurring at $\kappa = 11$ for both cases. These values were obtained by deactivating the stopping criterion to let the iterations continue for higher values of κ and to see at what point the minimum uncertainty occurs. Comparing these values to the uncertainties at the final iterations shown in Figure 5.3(a) and 5.3(c), one concludes that the iterations stopped very close to the tradeoff point, hence confirming the suitability of the devised criteria.

Figure 5.4 and 5.5 contain volume representations of some measurement results for examples I and II, respectively. The correlation residuals (Figure 5.4(f) and 5.5(f)) ranging between -0.5 and 0.5 (in the dynamic range scale of the original images) imply that satisfactory correlations have been established between the undeformed and deformed states. Figure 5.4 and 5.5(d)-(e) show the calculated ε_{zz} strain (exact and measured) mapped on the deformed state of the volume. The measured strains reveal a significant similarity to the exact simulated strains, which means that IS-DVC was successfully capable of capturing the strain heterogeneities through the volume. This can be better perceived from Figure 5.4 and 5.5(b)-(c) , which represent the thresholded ε_{zz} strains in the particles with threshold values -1.6% and -1.3%, respectively. These values were chosen according to the statistical distribution of the exact strain using "simple thresholding" (e.g. `graythresh` in MATLAB). One recognizes a close estimation of the shape and the orientation of the particles from their thresholded measured strain, when compared to the exact strain as well as the original geometry. Table 5.2 gives the measured strains uncertainties as well as the mean strain values

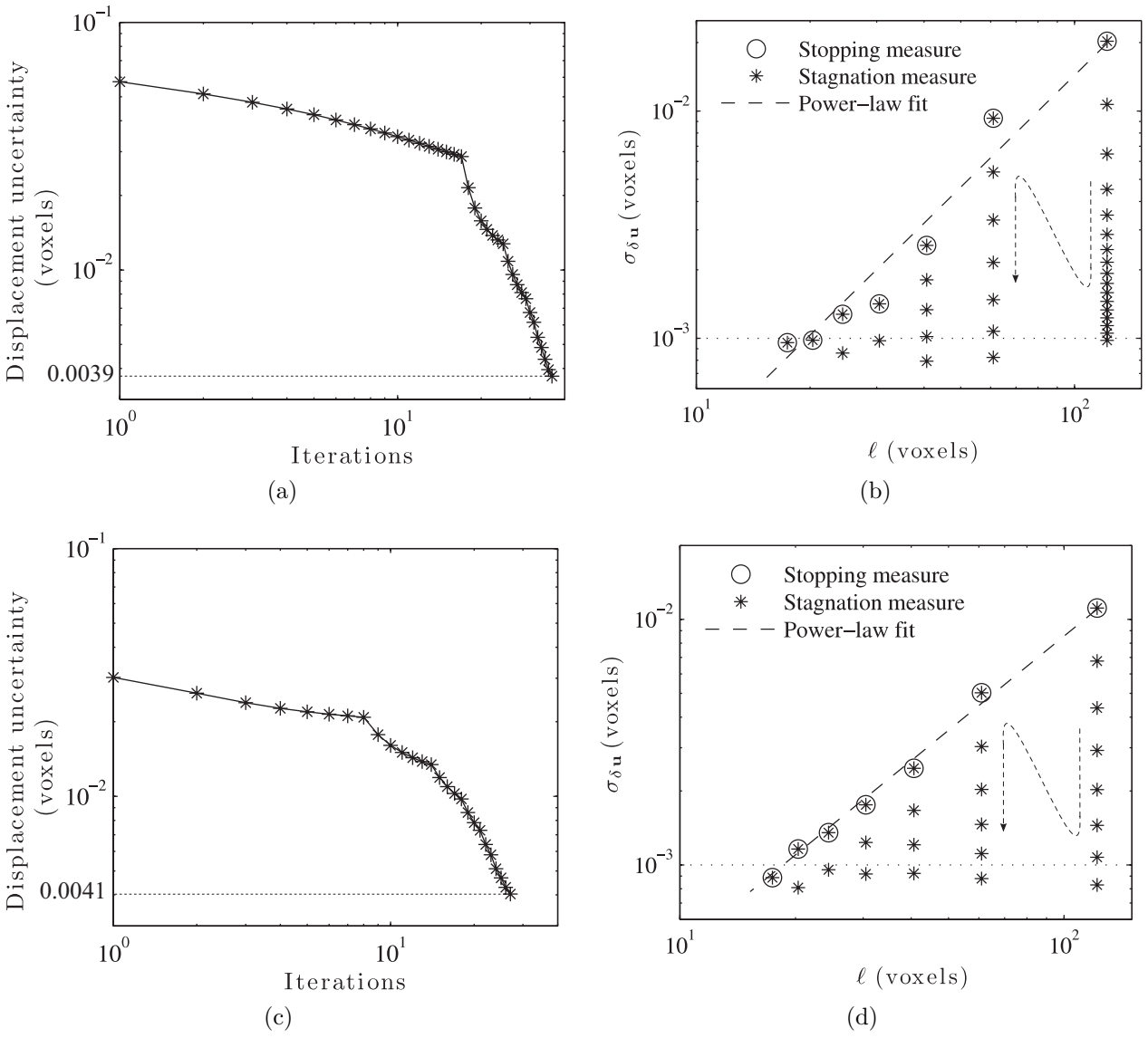

Figure 5.3 Trend of displacement uncertainty as a function of iterations (a and c) and trend of $\sigma_{\delta \mathbf{u}}$ as a function of characteristic subset length ℓ (b and d) for examples I and II, respectively.

(denoted by a bar) within individual phases for the two examples. The uncertainty of the ε_{zz} strain within the particle (p) or matrix (m) is denoted by $\delta\varepsilon_{zz}^{p/m}$ and is calculated as the following:

$$\delta\varepsilon_{zz}^{q} = \sqrt{\frac{\sum_{i\in\Omega_q}\left(\varepsilon_{zz}^{\text{measured}}\left(\mathbf{x}^{\langle i\rangle}\right) - \varepsilon_{zz}^{\text{exact}}\left(\mathbf{x}^{\langle i\rangle}\right)\right)^2}{N_q}} \tag{5.26}$$

where Ω_q denotes the ensemble of the regions containing the voxels of the individual phase q, and N_q is the total number of voxels in that region. One notes higher uncertainties within the particle, which is due to the abrupt changes of the strain in the vicinity of this phase.

Table 5.2 Strain uncertainties as well as strain averages within individual phases for examples I and II: Comparison of averages with the exact strains

	κ	$\bar{\varepsilon}^m_{zz}$	$\delta\varepsilon^m_{zz}$	$\bar{\varepsilon}^p_{zz}$	$\delta\varepsilon^p_{zz}$
Artificial composite with spherical particles					
IS-DVC measurements	9	-0.0230	0.0017	-0.0130	0.002
Simulation results (preset values)	NA	-0.0231		-0.0127	
Artificial composite with non-aligned quasi-cylindrical fibers					
IS-DVC measurements	10	-0.0206	0.0018	-0.0070	0.0035
Simulation results (preset values)	NA	-0.0207		-0.0065	

Nevertheless, this uncertainty is lower in the case of composite with spherical particles. This is mainly due to the lower elastic modulus contrast as well as the larger particle size (lower size ratio) of the spheres, when compared to those of the ellipsoids. The former reduces the heterogeneity of the strain while the latter increases the displacement resolution within the particles.

It is possible to derive a quantitative measure of proper particle size ratio with respect to the cutoff wavenumber κ using the characteristic subset length. In order for IS-DVC to be able to best estimate the strain within the particle, the particle's (smallest) radius, r, should be larger than the characteristic subset length, i.e.

$$r > \frac{2L}{\alpha\kappa} \quad \text{or} \quad \kappa > \beta d \tag{5.27}$$

where $d = L/r$ is the particle size ratio (see Table 5.1) and $\beta = 2/\alpha \approx 1.6-1.9$. On this basis, κ_{min} for the spherical particles turned out to be 5 while this value for the elliptical particles was $25 \sim 30$. Obviously, we did not reach this value for the ellipsoidal particles due to the insufficient intensity variations associated to the 3D texture of the volume image. The above quantitative measure allows one to determine the feasibility of high-resolution measurements for a given composite geometry according to the particle size (in voxels) within the image.

5.6.2 Example III: crack displacement field

For the third example, the algorithm stopped at $\kappa = 13$. This means that higher DOF had larger impact on the uncertainty reduction, when compared to the two previous examples, which is not surprising since a discontinuous displacement field should be estimated. The measurements for $w(\mathbf{x})$ along a vertical line containing the discontinuity is plotted for $\kappa = 3$ and $\kappa = 13$ and compared to the exact plot in Figure 5.7. As seen from the plot, for $\kappa = 13$, the displacement errors were rapidly damped for regions away from the discontinuity.

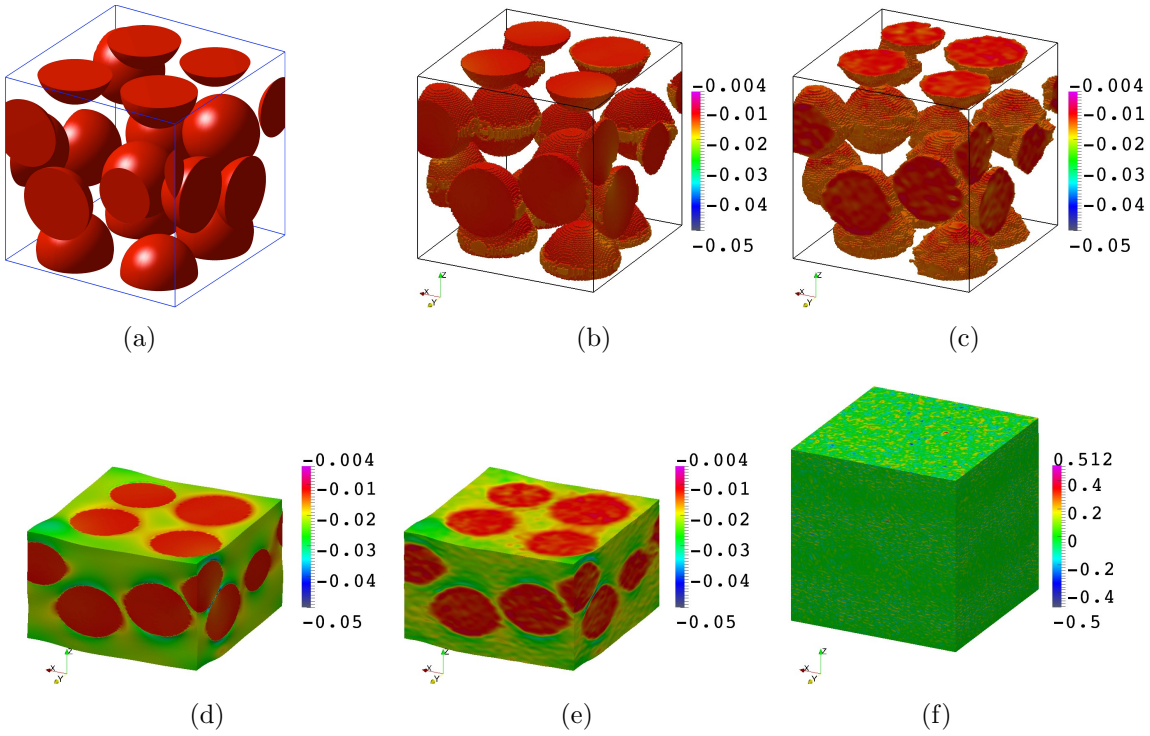

Figure 5.4 (a) Geometry of the artificial composite with spherical particles (b) thresholded exact strain ε_{zz} with threshold value = 1.6% (c) thresholded measured strain ε_{zz} with the same threshold value as that of (b) (d) exact strain ε_{zz} image mapped on the deformed volume (according to the exact displacement field) (e) measured strain ε_{zz} image mapped on the deformed volume (according to the measured displacement field) (f) correlation residuals for the resulted measurements values are in the scale of the image dynamic range.

Figure 5.6 shows the volume image of the displacement field $w(\mathbf{x})$ compared to the exact displacement. A close agreement between the measured and the exact displacements can be observed, especially for regions far from the crack surface. The displacement uncertainty excluding the cracked region (10 voxels all around the crack) was .006 voxels, which is very acceptable, when compared to the other examples (Figure 5.3). The correlation residuals for this examples (Figure 5.6(c)) demonstrates how well the algorithm has succeeded to correlate the undeformed and deformed images. Obviously, there are significant residuals in the crack region, which means that the algorithm underperformed in this area. The presented example reveals that such discontinuities have very little effects on the accuracy of the measurements sufficiently far from the crack.

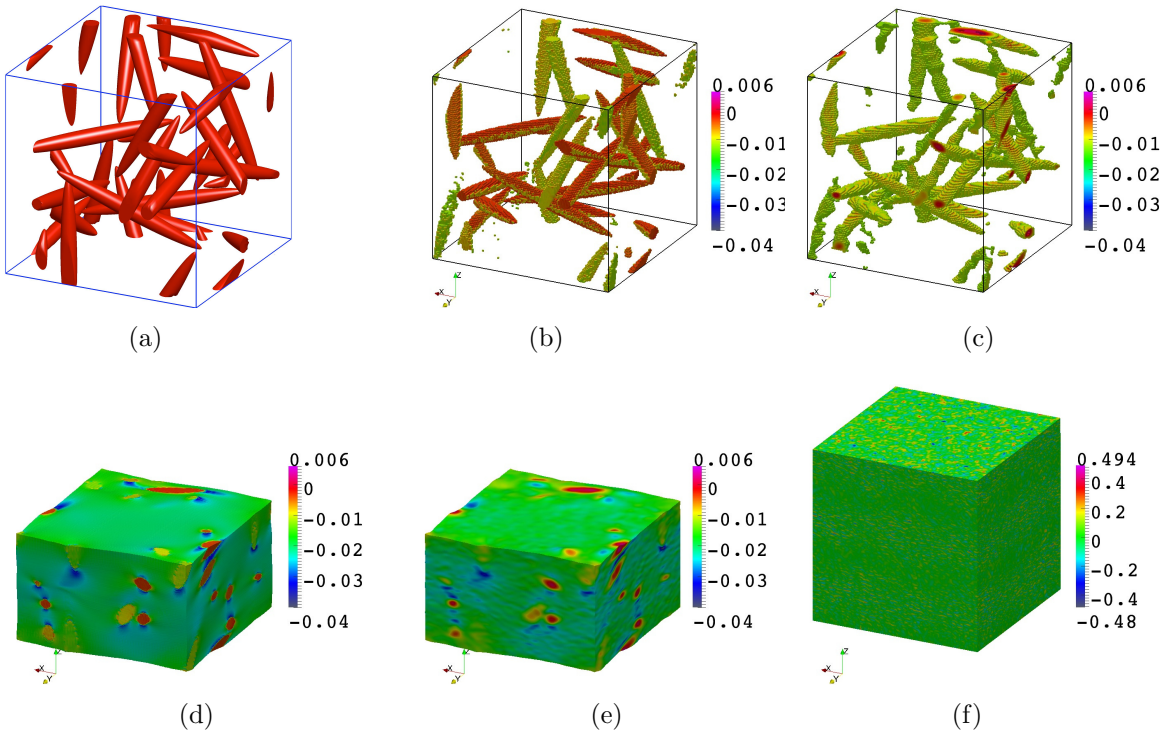

Figure 5.5 (a) Geometry of the artificial composite with elliptical particles (b) thresholded exact strain ε_{zz} with threshold value = 1.3% (c) thresholded measured strain ε_{zz} with the same threshold value as that of (b) (d) exact strain ε_{zz} image mapped on the deformed volume (according to the exact displacement field) (e) measured strain ε_{zz} image mapped on the deformed volume (according to the measured displacement field) (f) correlation residuals for the resulted measurements values are in the scale of the image dynamic range.

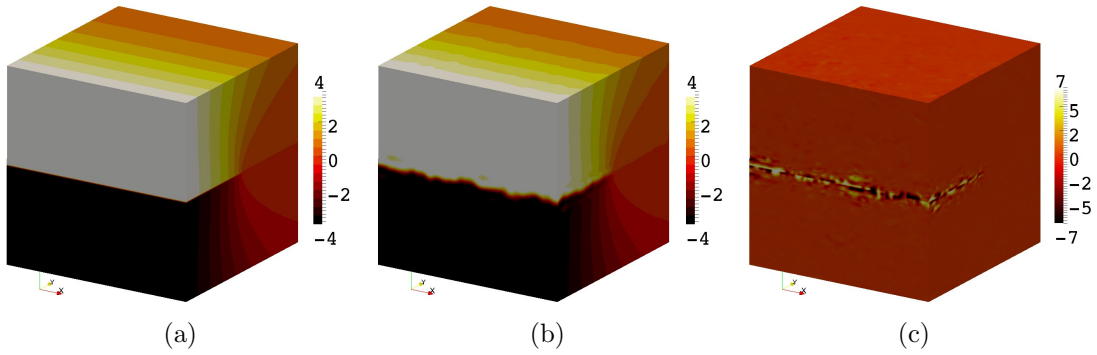

Figure 5.6 (a) Exact displacement field in z direction for the analytical mode I crack (b) measured displacement field (c) correlation residuals, values are in the scale of image dynamic range

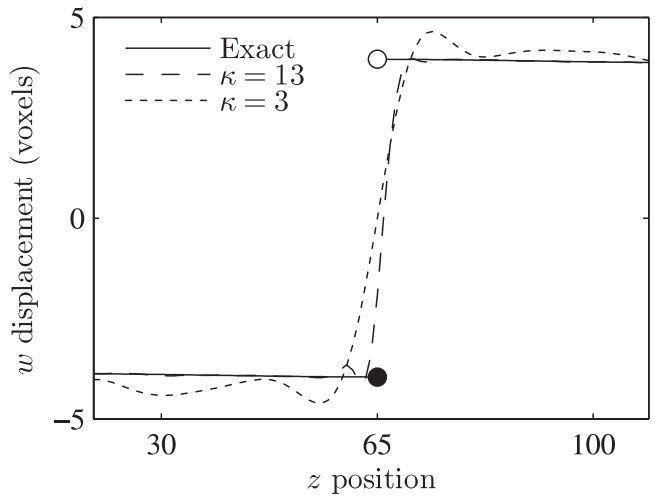

Figure 5.7 Behavior of the measured displacement in the vicinity of the discontinuity for example III

5.7 Conclusion

We proposed a global approach for fast and accurate high-resolution DVC. The approach was an extension to 3D of the 2D ISA based on a Fourier decomposition for the sought displacement field. Several artificial experiments were performed to evaluate the functionality of the IS-DVC for high resolution displacement measurements. Especially, two artificial composites were generated with spherical and quasi-cylindrical non-aligned particles to simulate the artificial experiments using synthetic images. The measurements on the composites were proven to be very successful in capturing strain heterogeneities through the volume with acceptable uncertainties, both in displacements and strains. Stopping and stagnation measures devised in the IS-DVC algorithm were shown to be very efficient in systematically stopping the iterations, hence adding to the robustness of the whole measurement process. Using the notion of characteristic subset length previously introduced in (Mortazavi *et al.*, 2013), a quantitative measure was derived to estimate the proper particle voxel-size for accurate capturing of strain heterogeneities as a function of cutoff wavenumber defining the measurement resolution. This a priori knowledge would help better designing experimental parameters (e.g. magnification, imaging resolution, etc.) to obtain the best results from IS-DVC. Furthermore, a third artificial example dealt with the measurement of a discontinuous displacement field of analytical mode I crack from linear elastic fracture mechanics. The resulted measurement uncertainties, although not very low in the vicinity of the discontinuity, turned out to be fairly acceptable (around 0.006 voxel) for regions further from the crack. This experiment assessed the stability of IS-DVC in dealing with discontinuities.

The results obtained in this study are very promising for high-resolution DVC thanks to the significantly low computational costs associated with IS-DVC. It should be noted, however, that this first step requires further studies to deal with experimental limitations such as noise and artifact effects, which may hinder the full exploitation of the approach if not taken into consideration.

5.8 Acknowledgements

This research was funded by Fonds Québécois de la Recherche sur la Nature et les Technologies (FQRNT)-projets de recherche en équipe and the Canada Research Chair program (M. Lévesque and I. Villemure).

5.9 REFERENCES

BARNSLEY, M. F., DEVANEY, R. L., MANDELBROT, B. B., PEITGEN, D. and VOSS, R. F. (1988). *The Science of Fractal Images*. Springer-Verlag, Berlin.

BARRANGER, Y., DOUMALIN, P., GERMANEAU, A. and VALLE, V. (2010). X-ray computed tomography coupled to digital volume correlation applied to a stationary crack case. *EPJ Web of Conferences*, 6, 42015.

BAY, B., SMITH, T., FYHRIE, D. and SAAD, M. (1999). Digital volume correlation: three-dimensional strain mapping using x-ray tomography. *Experimental Mechanics*, 39, 217 – 26.

BAY, B. K. (1995). Texture correlation: A method for the measurement of detailed strain distributions within trabecular bone. *Journal of Orthopaedic Research*, 13, 258–267.

BESNARD, G., HILD, F. and ROUX, S. (2006). "finite-element" displacement fields analysis from digital images: Application to portevin-le châtelier bands. *Experimental Mechanics*, 46, 789 – 803.

BORNERT, M., CHAIX, J., DOUMALIN, P., DUPRÉ, J., FOURNEL, T., JEULIN, D., MAIRE, E., MOREAUD, M. and MOULINEC, H. (2004). Mesure tridimensionnelle de champs cinématiques par imagerie volumique pour l'analyse des matériaux et des structures. *Photomécanique*, 4/3-4, 43–88.

BRÉMAND, F., GERMANEAU, A., DOUMALIN, P. and DUPRÉ, J. (2008). Study of mechanical behavior of cancellous bone by digital volume correlation and x-ray micro-computed tomography. *Soc. Exp. Mech. - Int. Congr. Exhib. Exp. Appl. Mech.* Orlando, FL, United states, vol. 3, 1527 – 1533.

CLAIRE, D., HILD, F. and ROUX, S. (2004). A finite element formulation to identify damage fields: the equilibrium gap method. *International Journal for Numerical Methods in Engineering*, 61, 189–208.

FAGERHOLT, E., BORVIK, T. and HOPPERSTAD, O. (2013). Measuring discontinuous displacement fields in cracked specimens using digital image correlation with mesh adaptation and crack-path optimization. *Optics and Lasers in Engineering*, 51, 299 – 310.

FONSECA, J. Q. D., MUMMERY, P. M. and WITHERS, P. J. (2005). Full-field strain mapping by optical correlation of micrographs acquired during deformation. *Journal of Microscopy*, 218, 9–21.

FORSBERG, F. (2008). *X-ray Microtomography and Digital Volume Correlation for Internal Deformation and Strain Analysis*, Luleå University of Technology,Department of Applied Physics and Mechanical Engineering.

FORSBERG, F., MOOSER, R., ARNOLD, M., HACK, E. and WYSS, P. (2008). 3d micro-scale deformations of wood in bending: synchrotron radiation mu-ct data analyzed with digital volume correlation. *J. Struct. Biol. (USA)*, 164, 255 – 62.

FORSBERG, F. and SIVIOUR, C. R. (2009). 3d deformation and strain analysis in compacted sugar using x-ray microtomography and digital volume correlation. *Measurement Science and Technology*, 20, 095703 (8pp).

FRANCK, C., HONG, S., MASKARINEC, S., TIRRELL, D. and RAVICHANDRAN, G. (2007). Three-dimensional full-field measurements of large deformations in soft materials using confocal microscopy and digital volume correlation. *Experimental Mechanics*, 47, 427 – 438.

GERMANEAU, A., DOUMALIN, P. and DUPRÉ, J.-C. (2008). Comparison between x-ray micro-computed tomography and optical scanning tomography for full 3d strain measurement by digital volume correlation. *NDT&E International*, 41, 407 – 415.

GEYMONAT, G. and PAGANO, S. (2003). Identification of mechanical properties by displacement field measurement: A variational approach. *Meccanica*, 38, 535–545.

GHOSSEIN, E. and LÉVESQUE, M. (2012). A fully automated numerical tool for a comprehensive validation of homogenization models and its application to spherical particles reinforced composites. *International Journal of Solids and Structures*, 49, 1387 – 1398.

GRÉDIAC, M. (2004). The use of full-field measurement methods in composite material characterization: interest and limitations. *Composites Part A: Applied Science and Manufacturing*, 35, 751 – 761.

HALL, S., BORNERT, M., DESRUES, J., PANNIER, Y., LENOIR, N., VIGGIANI, G. and BESUELLE, P. (2010). Discrete and continuum analysis of localised deformation in sand using x-ray ct and volumetric digital image correlation. *Geotechnique*, 60, 315 – 322.

HARDISTY, M. R. and WHYNE, C. M. (2009). Whole bone strain quantification by image registration: A validation study. *Journal of Biomechanical Engineering-Transactions of the ASME*, 131.

HILD, F. and ROUX, S. (2012). Comparison of local and global approaches to digital image correlation. *Experimental Mechanics*, 52, 1503–1519.

ISO/IEC guide 99 (2007). *International vocabulary of metrology - Basic and general concepts and associated terms (VIM).*

LECLERC, H., PÉRIÉ, J.-N., ROUX, S. and HILD, F. (2011). Voxel-scale digital volume correlation. *Experimental Mechanics*, 51, 479–490.

LEHMANN, T. M., GÖNNER, C. and SPITZER, K. (1999). Survey: Interpolation methods in medical image processing. *IEEE Transactions on Medical Imaging*, 18, 1049–1075.

LENOIR, N., BORNERT, M., DESRUES, J., BESUELLE, P. and VIGGIANI, G. (2007). Volumetric digital image correlation applied to x-ray microtomography images from triaxial compression tests on argillaceous rock. *Strain (UK)*, 43, 193 – 205.

MORTAZAVI, F., LÉVESQUE, M. and VILLEMURE, I. (2013). Image-based continuous displacement measurements using an improved spectral approach. Manuscript accepted for publication on Jan. 29, 2013 in Strain.

MOULINEC, H. and SUQUET, P. (1998). A numerical method for computing the overall response of nonlinear composites with complex microstructure. *Computer Methods in Applied Mechanics and Engineering*, 157, 69 – 94.

NOCEDAL, J. and WRIGHT, S. J. (2000). *Numerical Optimization*. Springer.

PÉRIÉ, J.-N., LECLERC, H., ROUX, S. and HILD, F. (2009). Digital image correlation and biaxial test on composite material for anisotropic damage law identification. *International Journal of Solids and Structures*, 46, 2388–2396.

RÉTHORÉ, J., HILD, F. and ROUX, S. (2008a). Extended digital image correlation with crack shape optimization. *International journal for numerical methods in engineering*, 73, 248–272.

RÉTHORÉ, J., LIMODIN, N., BUFFIÈRE, J.-Y., HILD, F., LUDWIG, W. and ROUX, S. (2011). Digital volume correlation analyses of synchrotron tomographic images. *The Journal of Strain Analysis for Engineering Design*, 46, 683–695.

RÉTHORÉ, J., TINNES, J.-P., ROUX, S., BUFFIÈRE, J.-Y. and HILD, F. (2008b). Extended three-dimensional digital image correlation (x3d-dic). *C.R. Mecanique*, 336, 643–9.

ROUX, S., HILD, F. and BERTHAUD, Y. (2002). Correlation image velocimetry: A spectral approach. *Applied Optics*, 41, 108–115.

ROUX, S., HILD, F., VIOT, P. and BERNARD, D. (2008). Three-dimensional image correlation from x-ray computed tomography of solid foam. *Composites Part A: Applied Science and Manufacturing*, 39, 1253 – 1265.

ROUX, S., RETHORE, J. and HILD, F. (2009). Digital image correlation and fracture: an advanced technique for estimating stress intensity factors of 2d and 3d cracks. *Journal of Physics D: Applied Physics*, 42, 214004 (21pp).

SMITH, T., BAY, B. and RASHID, M. (2002). Digital volume correlation including rotational degrees of freedom during minimization. *Proc. Soc. Exp. Mech. (USA)*, 49, 272 – 278.

SUTTON, M., WOLTERS, W., PETERS, W., RANSON, W. and MCNEILL, S. (1983). Determination of displacements using an improved digital correlation method. *Image and Vision Computing*, 1, 133 – 139.

UNSER, M., ALDROUBI, A. and EDEN, M. (1993a). B-spline signal processing. i. theory. *Signal Processing, IEEE Transactions on*, 41, 821 –833.

UNSER, M., ALDROUBI, A. and EDEN, M. (1993b). B-spline signal processing. ii. efficiency design and applications. *Signal Processing, IEEE Transactions on*, 41, 834 –848.

VERHULP, E., RIETBERGEN, B. V. and HUISKES, R. (2004). A three-dimensional digital image correlation technique for strain measurements in microstructures. *Journal of Biomechanics*, 37, 1313 – 1320.

WAGNE, B., ROUX, S. and HILD, F. (2002). Spectral approach to displacement evaluation from image analysis. *Eur. Phys. J. AP*, 17, 247–252.

ZAUEL, R., YENI, Y., BAY, B., DONG, X. and FYHRIE, D. (2006). Comparison of the linear finite element prediction of deformation and strain of human cancellous bone to 3d digital volume correlation measurements. *Journal of Biomechanical Engineering*, 128, 1 – 6.

CHAPTER 6

GENERAL DISCUSSION

In the following, certain important advantages and limitations of the improved spectral approach with respect to the reviewed literature are discussed.

6.1 General remarks

A remarkable reconstruction capability for the improved spectral approach is inferred from the demonstrated results, which can be related to the weighted contribution of high-frequency basis functions provided by the Gaussian mask. For example, consider the cutoff ratio $\kappa/L = 10$ used for the simulated experiment on the SEM image (Table 4.2), which corresponds to $\kappa = 25$. Assume that the effective width size of the Gaussian mask $\approx \sqrt{2\pi}\kappa \approx 62$. It means that 62 DOF were considered for each direction, which corresponds to a characteristic length of ≈ 8 pixels. This spatial resolution may be difficult to achieve (with low uncertainty) for DIC approaches with low degrees of continuity unless regularized DIC is used (Réthoré, 2010). Nevertheless, in most of these approaches (based in the spatial domain), mesh refinement possibility allows for selectively decreasing the spatial resolution where it is a priori known to be needed. Thus, the measurement uncertainties, in contrast with the spectral approach, may be smartly controlled over the region. In FE-DIC, this is done using unstructured grids and a mechanically meaningful mesh refinement. However, when no a priori information is available about the location of the microstructure, the versatility of the improved spectral approach is clearly advantageous.

The developed spectral approach was based on a continuous formulation for the sought displacement field. The resulting displacement measurements were thus not reliable in the vicinity of a discontinuity, as demonstrated in chapter 5. On the other hand, a weaker form of discontinuity was addressed in chapter 4, which corresponded to discontinuities (jumps) of strain at the interface. In that case, the approach turned out to be successful. This is due to the fact that the pattern matching is significantly dependent on the displacement field rather than its derivatives, hence being more sensitive to displacement discontinuities.

6.2 Measurements on complex geometries

It is sometimes sought to measure displacements and strains on necessarily non-rectangular geometries. Regions containing holes or cruciform specimens in biaxial tests are possible ex-

amples. In FE framework, this is easily done by only meshing the complex geometry using an unstructured mesh (Leclerc *et al.*, 2009). In contrast, an inconvenience can be discerned in the improved spectral approach in dealing with such geometries. Indeed, the Fourier-based formulation for the sought displacement field was defined on a rectangular region. However, it is still possible to form the SSD criterion (1.1b) only for pixels within the complex geometry. In doing so, the Fourier integrals should be calculated excluding the *non-interested* regions from the rectangular zone. To this end, one just has to multiply the image functions and their derivatives by a proper mask *before* the frequency filtering is performed. This mask is zero in regions out of the non-rectangular ROI and one elsewhere. Nevertheless, this strategy creates undesirable textures, with zero information, which take part in the reconstruction process and consequently influence the measurements at other zones due to the nature of the frequency filtering. The affected zones are those near the complex boundaries, the extent of which can be estimated from the characteristic subset length given by equations (3.22) and (3.24). Thus, the robustness of the inverse problem in these regions might be degraded depending on the area of the zero-gradient regions and the chosen cutoff wavenumber. It is noteworthy that edge effects are inherent in all DIC approaches, thus leaving uncertain measurements near the boundaries with different levels of significance. For example, the mentioned significance for FE-DIC with C^0 continuity, should be lower than another FE-based formulation imposing higher order continuity (Langerholc *et al.*, 2012). Therefore, the possible advantages in this sense should be evaluated together with other accuracy parameters.

As an example of non-rectangular geometry, consider the 1024×1024-pixel 8-bit images shown in Figure 6.1, which corresponds to the cold expansion of a rivet assembly. The circle in the middle of the images corresponds to the location of a mandrel used for this purpose. By using the aforementioned strategy, the full-field displacements were measured using the improved spectral approach. A circular ring of width 20 pixels around the mandrel was considered to be excluded from the measurements. The width of this region was estimated as the half-width of the characteristic subset corresponding to $\kappa = 20$. Furthermore, the following tapered circular mask was used instead of on-off thresholding:

$$W(r) = \begin{cases} 0 & r < r_{\text{IN}} \\ \dfrac{1}{2}\left(1 + \cos\left(\pi \dfrac{r - r_{\text{OUT}}}{r_{\text{OUT}} - r_{\text{IN}}}\right)\right) & r_{\text{IN}} \leqslant r < r_{\text{OUT}} \\ 1 & r \geqslant r_{\text{OUT}} \end{cases} \tag{6.1}$$

where

$$r = \|\mathbf{x} - \mathbf{x}_c\|_2 \tag{6.2}$$

$\mathbf{x}_c$ is the coordinates of the center of the circle, r_{IN} denotes the hole radius, and r_{OUT} is the

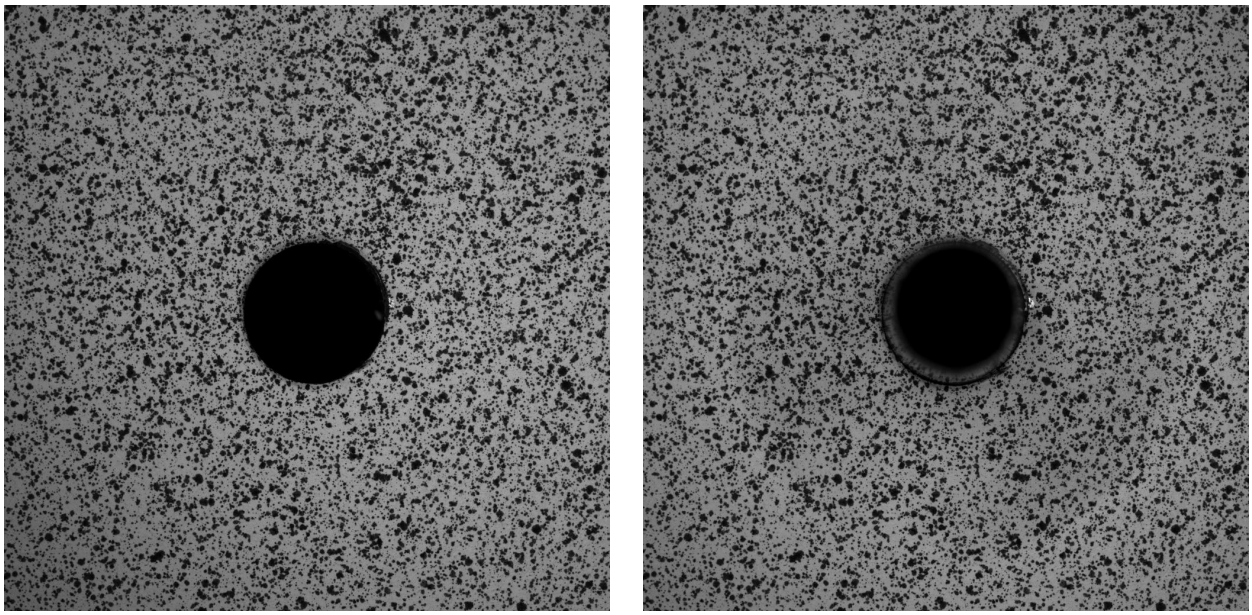

(a) (b)

Figure 6.1 1024 × 1024-pixel 8-bit images corresponding to the cold expansion of a rivet assembly on an aluminum alloy. (a) before the cold expansion (b) after the cold expansion

outer radius at which the mask reaches the value 1. The outer radius was chosen to be within the excluded ring. Thus, the masked functions were continuous at the edges.

Figure 6.2 presents the measured displacement fields for different values of κ. The large displacement gradients near the hole comply with the expected mechanical response of the assembly and therefore confirm the validity of the measurements. As seen from the displacement maps, the employed strategy was functional for this type of geometry. Also, one notes noisy measurements corresponding to $\kappa = 16, 20$. These uncertainties imply that the sought resolution was higher than the capacity of the intensity variations in revealing displacement spatial variations. On the other hand, the measurements by $\kappa = 16$ and 20 reveal no meaningful details that are not found in the lower resolution, i.e. that corresponding to $\kappa = 8$. These observations suggest that $\kappa = 8$ led to probably a better compromised resolution. Attaining higher resolutions in these cases is the subject of the regularized DIC, which is discussed in the sequel.

6.3 Regularization

Measurement instabilities occur due to several reasons, including insufficient intensity variations and noise. Considering the DIC as an inverse problem, it would be desirable to regularize the problem using a proper constraint. In that case, the new matching criterion Ξ

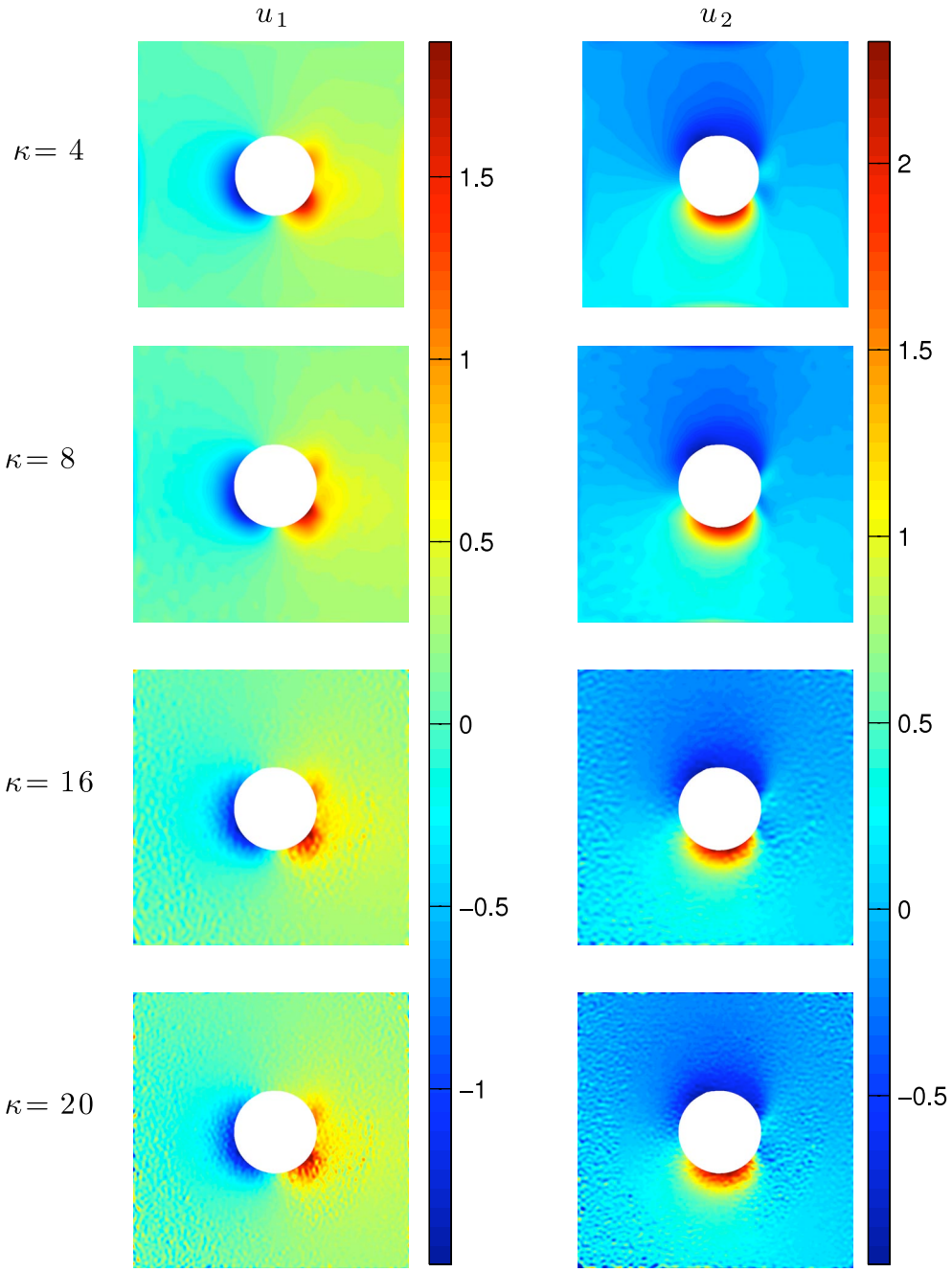

Figure 6.2 Measured displacement fields induced by the cold expansion for different values of κ calculated by the improved spectral approach

to be minimized is written as:

$$\Xi = \Phi_{\text{SSD}} + \gamma \Phi_{\text{REG}} \tag{6.3}$$

where Φ_{SSD} and Φ_{REG} denote the SSD criterion and the regularization term, respectively, and γ is the penalty parameter specifying the degree of significance of the regularization.

The regularization term may impose additional smoothness requirements on the displacement field or it may convey a mechanical meaning, e.g. satisfying the equilibrium condition. Irrespective of the type of constraint, the regularization will certainly come at additional computational costs. For the spectral approach, this leads to losing one advantage of the method, i.e. possibility of calculations in the spatial domain. For example, consider the following smoothness criterion, which aims at minimizing the variations of the displacement field:

$$\Phi_{\mathrm{REG}} = \int_{\mathrm{ROI}} \|\nabla_{\mathbf{x}}\mathbf{u}\|_F^2 \, \mathbf{dx} \tag{6.4}$$

where $\| \ \|_F^2$ denotes the Frobenius norm. Using the above term to regularize the spectral DIC leads to the following governing equation instead of equation (1.17) (see the Appendix):

$$\sum_n \widetilde{\mathbf{J}}_{[m-n]}\boldsymbol{\upsilon}_n + \gamma\|\boldsymbol{\omega}_m\|_2^2\boldsymbol{\upsilon}_m = \widetilde{\boldsymbol{\rho}}_{[m]} \tag{6.5}$$

As can be seen from equation (6.5), the additional term coming from the regularization is not a convolution product. Therefore, applying an inverse Fourier transform on equation (6.5) in this case will not simplify the task. Therefore, the solution for the regularized DIC should be found in the Fourier domain. However, this inconvenience will *partly* affect the computational efficiency of the approach. Indeed, the integrations involved in the governing equations are still calculated by FFT (leading to $\widetilde{\mathbf{J}}_{[m-n]}$ and $\widetilde{\boldsymbol{\rho}}_{[m]}$). Further studies are required to verify this hypothesis.

CONCLUSION

In this thesis, an improved global approach was developed for full-field displacement and strain measurements based on 2D and 3D images. With the global framework, in contrast with the possible local alternative, the DOF estimation in one ZOI depends also on that of other adjacent zones, thus increasing the robustness of the inverse problem. This advantage often comes at inherent computational expenses, especially at high displacement resolutions. The purpose of the thesis was therefore to reconcile these two seemingly contradictory advantages, i.e. low computational costs and high versatility in capturing strain heterogeneities.

Improvements were first performed on a 2D spectral approach previously developed in the literature. The remarkable potential of the approach was its versatility combined with low computational costs. The improvements consisted firstly in modifying the Fourier-based kinematic to increase the convergence speed and to decrease uncertainties for more complex displacement fields. Secondly, a strategy was developed for properly correcting for the boundary errors stemming from periodic basis functions. Also, a validated theoretical relation was presented to quantify the sensitivity of the improved spectral approach to image noise, which established a relation between the displacement resolution, noise level and texture properties. The developed algorithm was tested using computer-generated experiments, the results of which proved the functionality of the introduced modifications. Moreover, by comparing to the results obtained by the local approach, it was shown that the improved spectral approach outperformed the subset-based method thanks to the adopted global strategy as well as the high capacity of the improved method in estimating complex displacements. Also, an enhanced algorithm was developed to progressively allow for large number of Fourier modes using proper decision-making criteria within the measurement procedure. The ensemble of the comparisons and the obtained results validated the hypothesis that "proper improvements on the spectral approach will make it reliable and operational for practical cases" (chapter 2).

The potential application of such an approach for composite materials was illustrated by artificial and real SEM images of a FRP at micro-scale. A priori evaluations were performed first using simulated-real experiments. It consisted in artificially deforming the SEM images according to the displacement fields obtained by FE analysis of the replicated microstructure. These evaluations allowed for identifying suitable measurement parameters for the real measurements. Furthermore, they proved the high potentials of the approach in measuring full-field strains in the fiber scale. Comparing the obtained experimental results with those previously reported for the same experiment in the literature further revealed this capability. The study also took into account the effect of the recorded noise.

A global spectral DVC approach was developed from the extension of the 2D improved spectral approach. The potentials of the developed DVC technique were demonstrated by several artificial experiments simulating the volume images of composites recorded before and after deformation. Proper imaging resolution for accurate capturing of strain heterogeneities was estimated as a function of particle size and displacement resolution using a useful analogy presented in the 2D approach.

The main contribution of this thesis was the development of a global approach for accurate measurement of high-resolution full-field strains in 2D and 3D. This approach is very promising for strain mapping at micro-structural levels since it enables low computational costs while being highly versatile.

Recommendations for future studies

In the following, important questions raised during this thesis are discussed:

- **Measurements on complex geometries:** Further studies are recommended to characterize and subsequently reduce the edge effects induced by the non-rectangular boundaries. Specifically, the studies should consist of several artificial experiments on different types of geometry. The noise-sensitivity should be investigated while taking different geometries into account. Strategies should be developed to create tapered masks, such as that discussed in chapter 6, which are adaptable to a wider range of geometries. Once successful studies performed in 2D, the strategy could be developed to DVC.
- **Comparison to other global approaches:** A complement to what has been done in this thesis would be comparing the improved spectral approach with other global methods, such as FE-DIC and B-Splines DIC. One interesting hypothesis to verify is the efficiency of the highly continuous kinematic basis on the accuracy at high resolutions, when compared to a C^0 FE formulation. First, proper resolution parameters leading to equal measurement uncertainties should be identified for both approaches. The sensitivity to noise could be subsequently compared as a function of the noise level. This comparison also includes the theoretical noise sensitivity relations. To this end, first a quantitative analogy, similar to what was done with respect to the subset-based method, should be established between the element size in the FE-DIC and the cutoff wavenumber in the improved spectral approach. This analogy allows for a fair comparison of the noise sensitivities as a function of displacement resolution.

  As for high-resolution strain measurements, it would be interesting to compare the reconstruction capacity of various approaches. For example, for FE-DIC, it would be interesting to verify possible advantages of mesh refinement using unstructured grids.

The comparison of the calculation time and memory requirements should be performed to complete this task.

- **Regularization:** First, proper regularization terms should be chosen. One possible choice would be the minimization of the Dirichlet Energy (norm of displacement gradients integrated over space) as demonstrated in chapter 6. The additional computation costs dictated by the regularization should be evaluated, especially compared to other approaches. Mechanical regularizations could also be sought. For example, under the assumption of having a periodic micro-structure subjected to periodic boundary conditions, there are iterative solutions of the equilibrium equation (Gururajan, 2006) in the frequency domain that can be coupled with the image correlation equation. In that case, the efficiency of such a constraint for non-periodic micro-structures should be verified. The periodic boundary conditions, however, are almost satisfied since the a priori non-periodicity correction is implemented. The new approach, once developed, should be validated through a series of artificial and real experiments. The effect of the penalization coefficient should be investigated. Once the feasibility of the regularization is validated, it would be interesting to evaluate the effect of non-exact mechanical properties on the final uncertainty of the measurements.
- **Applications:** The real applications of the developed DVC algorithm was not investigated in this thesis. Indeed, as a complementary to the artificial experiments on the composites, it would be interesting to conduct experiments on these materials. First and foremost, a suitable fabrication strategy should be investigated, by which sufficient texture could be acquired by the 3D imaging system. To this end, addition of small particles during the fabrication process might be necessary. In this regard, it is crucial to design the fabrication procedure with respect to the practical resolution given by the imaging system, so that the acquired volume image possesses sufficient texture for the DVC. Given the measurements are to be performed at high resolutions, the size of the reinforcement should be large enough to accurately reveal the strain heterogeneities. The recommendations given in the articles will be of great use during the elaboration process. X-ray synchrotron microtomography is strongly recommended for this purpose because of its great image quality suitable for quantitative image analysis. The imaging artifacts, however, are inevitable during the image reconstruction. The regularized DVC algorithm would increase the robustness of the approach in dealing with such noises.

REFERENCES

AMINI, S., MORTAZAVI, F., SUN, J., LEVESQUE, M., HOEMANN, C. and VILLEMURE, I. (2013). Stress relaxation of swine growth plate in semi-confined compression: depth dependent tissue deformational behavior versus extracellular matrix composition and collagen fiber organization. *Biomechanics and Modeling in Mechanobiology*, 12, 67–78.

ANZELOTTI, G., NICOLETTO, G. and RIVA, E. (2008). Mesomechanic strain analysis of twill-weave composite lamina under unidirectional in-plane tension. *Composites Part A: Applied Science and Manufacturing*, 39, 1294 – 1301.

ASTER, R., BORCHERS, B. and THURBER, C. (2005). *Parameter Estimation and Inverse Problems (International Geophysics)*. Academic Press.

AVRIL, S., BONNET, M., BRETELLE, A.-S., GRÉDIAC, M., HILD, F., IENNY, P., LATOURTE, F., LEMOSSE, D., PAGANO, S., PAGNACCO, E. and PIERRON, F. (2008). Overview of identification methods of mechanical parameters based on full-field measurements. *Experimental Mechanics*, 48, 381–402.

BARNSLEY, M. F., DEVANEY, R. L., MANDELBROT, B. B., PEITGEN, D. and VOSS, R. F. (1988). *The Science of Fractal Images*. Springer-Verlag, Berlin.

BARRANGER, Y., DOUMALIN, P., GERMANEAU, A. and VALLE, V. (2010). X-ray computed tomography coupled to digital volume correlation applied to a stationary crack case. *EPJ Web of Conferences*, 6, 42015.

BAY, B., SMITH, T., FYHRIE, D. and SAAD, M. (1999). Digital volume correlation: three-dimensional strain mapping using x-ray tomography. *Experimental Mechanics*, 39, 217 – 26.

BAY, B. K. (1995). Texture correlation: A method for the measurement of detailed strain distributions within trabecular bone. *Journal of Orthopaedic Research*, 13, 258–267.

BENOIT, A., GUÉRARD, S., GILLET, B., GUILLOT, G., HILD, F., MITTON, D., PÉRIÉ, J.-N. and ROUX, S. (2009). 3d analysis from micro-mri during in situ compression on cancellous bone. *Journal of Biomechanics*, 42, 2381 – 2386.

BESNARD, G., HILD, F. and ROUX, S. (2006). "finite-element" displacement fields analysis from digital images: Application to portevin-le châtelier bands. *Experimental Mechanics*, 46, 789 – 803.

BORNERT, M., BRÉMAND, F., DOUMALIN, P., DUPRÉ, J., FAZZINI, M., GRÉDIAC, M., HILD, F., MISTOU, S., MOLIMARD, J., ORTEU, J. J., ROBERT, L., SURREL,

Y., VACHER, P. and WATTRISSE, B. (2009). Assessment of digital image correlation measurement errors: Methodology and results. *Experimental Mechanics*, 49, 353–370.

BORNERT, M., CHAIX, J., DOUMALIN, P., DUPRÉ, J., FOURNEL, T., JEULIN, D., MAIRE, E., MOREAUD, M. and MOULINEC, H. (2004). Mesure tridimensionnelle de champs cinématiques par imagerie volumique pour l'analyse des matériaux et des structures. *Photomécanique*, 4/3-4, 43–88.

BRÉMAND, F., GERMANEAU, A., DOUMALIN, P. and DUPRÉ, J. (2008). Study of mechanical behavior of cancellous bone by digital volume correlation and x-ray micro-computed tomography. *Soc. Exp. Mech. - Int. Congr. Exhib. Exp. Appl. Mech.* Orlando, FL, United states, vol. 3, 1527 – 1533.

BRUCK, H., MCNEILL, S., SUTTON, M. and PETERS, W. (1989). Digital image correlation using newton-raphson method of partial differential correction. *Experimental Mechanics*, 29, 261–267.

CANAL, L., GONZALEZ, C., MOLINA-ALDAREGUIA, J., SEGURADO, J. and LLORCA, J. (2012). Application of digital image correlation at the microscale in fiber-reinforced composites. *Composites Part A: Applied Science and Manufacturing*, 43, 1630–1638.

CHEN, D. J., CHIANG, F. P., TAN, Y. S. and DON, H. S. (1993). Digital speckle-displacement measurement using a complex spectrum method. *Applied Optics*, 32, 1839–1849.

CHENG, P., SUTTON, M., SCHREIER, H. and MCNEILL, S. (2002). Full-field speckle pattern image correlation with B-Spline deformation function. *Experimental Mechanics*, 42, 344–352.

CHEVALIER, L., CALLOCH, S., HILD, F. and MARCO, Y. (2001). Digital image correlation used to analyze the multiaxial behavior of rubber-like materials. *European Journal of Mechanics - A/Solids*, 20, 169 – 187.

CHIANG, F. P., WANG, Q. and LEHMAN, F. (1997). New developments in full-field strain measurements usign speckles. G. F. Lucas and D. A. Stubbs, éditors, *Nontraditional Methods of Sensing Stress, Strain, and Damage in Materials and Structures*, ASTM, Kansas City, Missouri, USA, no. 1318 Special Technical Publication Optical, Non-Contacting Strain Measurement Devices. 156–159.

CHIVERS, K. F. and CLOCKSIN, W. F. (2000). Inspection of surface strain in materials using optical flow. *11 British Machine Vision Conference*. 392–401.

CLAIRE, D., HILD, F. and ROUX, S. (2004). A finite element formulation to identify damage fields: the equilibrium gap method. *International Journal for Numerical Methods in Engineering*, 61, 189–208.

DAVIS, C. Q. and FREEMAN, D. M. (1998). Statistics of subpixel registration algorithms based on spatiotemporal gradients or block matching. *Optical Engineering*, 37, 1290–1298.

D'ERRICO, J. (2005). Surface fitting using gridfit. Matlab Central Files (url:http://www.mathworks.com/matlabcentral/fileexchange/8998), Retrieved 10 May, 2011.

FAGERHOLT, E., BORVIK, T. and HOPPERSTAD, O. (2013). Measuring discontinuous displacement fields in cracked specimens using digital image correlation with mesh adaptation and crack-path optimization. *Optics and Lasers in Engineering*, 51, 299 – 310.

FONSECA, J. Q. D., MUMMERY, P. M. and WITHERS, P. J. (2005). Full-field strain mapping by optical correlation of micrographs acquired during deformation. *Journal of Microscopy*, 218, 9–21.

FORSBERG, F. (2008). *X-ray Microtomography and Digital Volume Correlation for Internal Deformation and Strain Analysis*, Luleå University of Technology,Department of Applied Physics and Mechanical Engineering.

FORSBERG, F., MOOSER, R., ARNOLD, M., HACK, E. and WYSS, P. (2008). 3d micro-scale deformations of wood in bending: synchrotron radiation mu-ct data analyzed with digital volume correlation. *J. Struct. Biol. (USA)*, 164, 255 – 62.

FORSBERG, F. and SIVIOUR, C. R. (2009). 3d deformation and strain analysis in compacted sugar using x-ray microtomography and digital volume correlation. *Measurement Science and Technology*, 20, 095703 (8pp).

FORSBERG, F., SJÖDAHL, M., MOOSER, R., HACK, E. and WYSS, P. (2010). Full three-dimensional strain measurements on wood exposed to three-point bending: Analysis by use of digital volume correlation applied to synchrotron radiation micro-computed tomography image data. *Strain*, 46, 47 – 60.

FOUINNETEAU, M. and PICKETT, A. (2007). Shear mechanism modelling of heavy tow braided composites using a meso-mechanical damage model. *Composites Part A: Applied Science and Manufacturing*, 38, 2294 – 2306.

FRANCK, C., HONG, S., MASKARINEC, S., TIRRELL, D. and RAVICHANDRAN, G. (2007). Three-dimensional full-field measurements of large deformations in soft materials using confocal microscopy and digital volume correlation. *Experimental Mechanics*, 47, 427 – 438.

GATES, M., LAMBROS, J. and HEATH, M. (2011). Towards high performance digital volume correlation. *Experimental Mechanics*, 51, 491–507.

GERMANEAU, A., DOUMALIN, P. and DUPRÉ, J.-C. (2008). Comparison between x-ray micro-computed tomography and optical scanning tomography for full 3d strain measurement by digital volume correlation. *NDT&E International*, 41, 407 – 415.

GEYMONAT, G. and PAGANO, S. (2003). Identification of mechanical properties by displacement field measurement: A variational approach. *Meccanica*, 38, 535–545.

GHOSSEIN, E. and LÉVESQUE, M. (2012). A fully automated numerical tool for a comprehensive validation of homogenization models and its application to spherical particles reinforced composites. *International Journal of Solids and Structures*, 49, 1387 – 1398.

GIOACCHINO, F. and FONSECA, J. Q. D. (2012). Plastic strain mapping with sub-micron resolution using digital image correlation. *Experimental Mechanics*, 1–12.

GONZALEZ, R. C. and WOODS, R. E. (2007). *Digital Image Processing (3rd Edition)*. Prentice Hall.

GRÉDIAC, M. (2004). The use of full-field measurement methods in composite material characterization: interest and limitations. *Composites Part A: Applied Science and Manufacturing*, 35, 751 – 761.

GUILLEBAUD-BONNAFOUS, C., VASCONCELLOS, D., TOUCHARD, F. and CHOCINSKI-ARNAULT, L. (2012). Experimental and numerical investigation of the interface between epoxy matrix and hemp yarn. *Composites Part A: Applied Science and Manufacturing*, 43, 2046 – 2058.

GURURAJAN, M. (2006). *Elastic Inhomogeneity Effectson Microstructures: A phase field study*, Indian Institute of Science.

HALL, S., BORNERT, M., DESRUES, J., PANNIER, Y., LENOIR, N., VIGGIANI, G. and BESUELLE, P. (2010). Discrete and continuum analysis of localised deformation in sand using x-ray ct and volumetric digital image correlation. *Geotechnique*, 60, 315 – 322.

HARDISTY, M. R. and WHYNE, C. M. (2009). Whole bone strain quantification by image registration: A validation study. *Journal of Biomechanical Engineering-Transactions of the ASME*, 131.

HILD, F., PÉRIÉ, J.-N. and CORET, M. (1999). Mesure de champs de déplacements 2D par corrélation d'images numériques : Correli^{2d}, LMT-Cachan.

HILD, F., RAKA, B., BAUDEQUIN, M., ROUX, S. and CANTELAUBE, F. (2002). Multi-scale displacement field measurements of compressed mineral-wool samples by digital image correlation. *Applied Optics*, 41, 6815–6828.

HILD, F. and ROUX, S. (2012). Comparison of local and global approaches to digital image correlation. *Experimental Mechanics*, 52, 1503–1519.

HILD, F., ROUX, S., GRAS, R., GUERRERO, N., MARANTE, M. E. and FLÓREZ-LÓPEZ, J. (2009). Displacement measurement technique for beam kinematics. *Optics and Lasers in Engineering*, 47, 495–503.

ISO/IEC guide 99 (2007). *International vocabulary of metrology - Basic and general concepts and associated terms (VIM).*

JÄHNE, B. (2004). *Practical handbook on image processing for scientifc and technical applications*. CRC Press, Boca Raton, FL.

JIN, H. and BRUCK, H. A. (2005). Pointwise digital image correlation using genetic algorithms. *Experimental Techniques*, 29, 36 – 39.

KEYS, R. (1981). Cubic convolution interpolation for digital image processing. *Acoustics, Speech and Signal Processing, IEEE Transactions on*, 29, 1153 – 1160.

LANGERHOLC, M., SLAVIČ, J. and BOLTEŽAR, M. (2012). Absolute nodal coordinates in digital image correlation. *Experimental Mechanics*, 1–12.

LECLERC, H., PÉRIÉ, J.-N., ROUX, S. and HILD, F. (2011). Voxel-scale digital volume correlation. *Experimental Mechanics*, 51, 479–490.

LECLERC, H., PÉRIÉ, J.-N., ROUX, S. and HILD, F. C. (2009). Integrated digital image correlation for the identification of mechanical properties. *Proceedings of the 4th International Conference on Computer Vision/Computer Graphics CollaborationTechniques*. Springer-Verlag, Berlin, Heidelberg, MIRAGE '09, 161–171.

LEHMANN, T. M., GÖNNER, C. and SPITZER, K. (1999). Survey: Interpolation methods in medical image processing. *IEEE Transactions on Medical Imaging*, 18, 1049–1075.

LENOIR, N., BORNERT, M., DESRUES, J., BESUELLE, P. and VIGGIANI, G. (2007). Volumetric digital image correlation applied to x-ray microtomography images from triaxial compression tests on argillaceous rock. *Strain (UK)*, 43, 193 – 205.

LOMOV, S. V., IVANOV, D. S., VERPOEST, I., ZAKO, M., KURASHIKI, T., NAKAI, H., MOLIMARD, J. and VAUTRIN, A. (2008). Full-field strain measurements for validation of meso-fe analysis of textile composites. *Composites Part A: Applied Science and Manufacturing*, 39, 1218 – 1231.

LU, H. and CARY, P. (2000). Deformation measurements by digital image correlation: Implementation of a second-order displacement gradient. *Experimental Mechanics*, 40, 393 – 400.

MAKEEV, A., HE, Y., CARPENTIER, P. and SHONKWILER, B. (2012). A method for measurement of multiple constitutive properties for composite materials. *Composites Part A: Applied Science and Manufacturing*, 43, 2199 – 2210.

MENG, L., JIN, G. and YAO, X. (2007). Application of iteration and finite element smoothing technique for displacement and strain measurement of digital speckle correlation. *Optics and Lasers in Engineering*, 45, 57 – 63.

MOËS, N., DOLBOW, J. and BELYTSCHKO, T. (1999). A finite element method for crack growth without remeshing. *International Journal for Numerical Methods in Engineering*, 46, 131–150.

MORTAZAVI, F., LÉVESQUE, M. and VILLEMURE, I. (2013). Image-based continuous displacement measurements using an improved spectral approach. Manuscript accepted for publication on Jan. 29, 2013 in Strain.

MOULINEC, H. and SUQUET, P. (1998). A numerical method for computing the overall response of nonlinear composites with complex microstructure. *Computer Methods in Applied Mechanics and Engineering*, 157, 69 – 94.

MOUTRILLE, M.-P., DERRIEN, K., BAPTISTE, D., BALANDRAUD, X. and GRÉDIAC, M. (2009). Through-thickness strain field measurement in a composite/aluminium adhesive joint. *Composites Part A: Applied Science and Manufacturing*, 40, 985–996.

NICOLETTO, G., MARIN, T., ANZELOTTI, G. and RONCELLA, R. (2011). Application of high magnification digital image correlation technique to micromechanical strain analysis. *Strain*, 47, e66–e73.

NOCEDAL, J. and WRIGHT, S. J. (2000). *Numerical Optimization*. Springer.

PAN, B. (2009). Reliability-guided digital image correlation for image deformation measurement. *Appl. Opt.*, 48, 1535–1542.

PAN, B., HUIMIN, X., TAO, H., WEINING, W. and YAN, F. (2006a). Displacement smoothing and strain estimation using savitzky-golay filters in digital image correlation. *Key Engineering Materials*, 326-328 I, 135 – 138.

PAN, B. and LI, K. (2011). A fast digital image correlation method for deformation measurement. *Optics and Lasers in Engineering*, 49, 841 – 847.

PAN, B., LU, Z. and XIE, H. (2010). Mean intensity gradient: An effective global parameter for quality assessment of the speckle patterns used in digital image correlation. *Optics and Lasers in Engineering*, 48, 469 – 477.

PAN, B., XIE, H.-M., XU, B.-Q. and DAI, F.-L. (2006b). Performance of sub-pixel registration algorithms in digital image correlation. *Measurement Science and Technology*, 17, 1615 – 1621.

PASSIEUX, J.-C. and PÉRIÉ, J.-N. (2012). High resolution digital image correlation using proper generalized decomposition: Pgd-dic. *International Journal for Numerical Methods in Engineering*, 92, 531–550.

PÉRIÉ, J.-N., LECLERC, H., ROUX, S. and HILD, F. (2009). Digital image correlation and biaxial test on composite material for anisotropic damage law identification. *International Journal of Solids and Structures*, 46, 2388–2396.

PILCH, A., MAHAJAN, A. and CHU, T. (2004). Measurement of whole-field surface displacements and strain using a genetic algorithm based intelligent image correlation method. *Journal of Dynamic Systems, Measurement and Control, Transactions of the ASME*, 126, 479 – 488.

POISSANT, J. and BARTHELAT, F. (2010). A novel "subset splitting" procedure for digital image correlation on discontinuous displacement fields. *Experimental Mechanics*, 50, 353–364.

QIU, H., YAN, J., KWON, O.-H. and SUTTON, M. A. (2008). Crack detection by digital image correlation. *11th International Congress and Exhibition on Experimental and Applied Mechanics 2008*. Society for Experimental Mechanics, Orlando, FL, United states, vol. 2, 927 – 933.

RÉTHORÉ, J. (2010). A fully integrated noise robust strategy for the identification of constitutive laws from digital images. *International Journal for Numerical Methods in Engineering*, 84, 631–660.

RÉTHORÉ, J., ELGUEDJ, T., SIMON, P. and CORET, M. (2010). On the use of nurbs functions for displacement derivatives measurement by digital image correlation. *Experimental Mechanics*, 50, 1099–1116.

RÉTHORÉ, J., GRAVOUIL, A., MORESTIN, F. and COMBESCURE, A. (2005). Estimation of mixed-mode stress intensity factors using digital image correlation and an interaction integral. *International Journal of Fracture*, 132, 65–79.

RÉTHORÉ, J., HILD, F. and ROUX, S. (2007). Shear-band capturing using a multiscale extended digital image correlation technique. *Computer Methods in Applied Mechanics and Engineering*, 196, 5016 – 5030.

RÉTHORÉ, J., HILD, F. and ROUX, S. (2008a). Extended digital image correlation with crack shape optimization. *International journal for numerical methods in engineering*, 73, 248–272.

RÉTHORÉ, J., LIMODIN, N., BUFFIÈRE, J.-Y., HILD, F., LUDWIG, W. and ROUX, S. (2011). Digital volume correlation analyses of synchrotron tomographic images. *The Journal of Strain Analysis for Engineering Design*, 46, 683–695.

RÉTHORÉ, J., MUHIBULLAH, ELGUEDJ, T., CORET, M., CHAUDET, P. and COMBESCURE, A. (2013). Robust identification of elasto-plastic constitutive law parameters from digital images using 3d kinematics. *International Journal of Solids and Structures*, 50, 73 – 85.

RÉTHORÉ, J., ROUX, S. and HILD, F. (2009). An extended and integrated digital image correlation technique applied to the analysis of fractured samples. *European Journal of Computational Mechanics/Revue Européenne de Mécanique Numérique*, 18, 285–306.

RÉTHORÉ, J., TINNES, J.-P., ROUX, S., BUFFIÈRE, J.-Y. and HILD, F. (2008b). Extended three-dimensional digital image correlation (x3d-dic). *C.R. Mecanique*, 336, 643–9.

ŘIHA, L., FISCHER, J., ŠMíD, R. and DOČEKAL, A. (2007). New interpolation methods for image-based sub-pixel displacement measurement based on correlation. *IEEE Instrumentation and Measurement Conference*. Institute of Electrical and Electronics Engineers Inc., Warsaw, Poland.

ROUX, S. and HILD, F. (2006). Stress intensity factor measurements from digital image correlation: post-processing and integrated approaches. *International Journal of Fracture*, 140, 141–157. 10.1007/s10704-006-6631-2.

ROUX, S., HILD, F. and BERTHAUD, Y. (2002). Correlation image velocimetry: A spectral approach. *Applied Optics*, 41, 108–115.

ROUX, S., HILD, F., VIOT, P. and BERNARD, D. (2008). Three-dimensional image correlation from x-ray computed tomography of solid foam. *Composites Part A: Applied Science and Manufacturing*, 39, 1253 – 1265.

ROUX, S., RETHORE, J. and HILD, F. (2009). Digital image correlation and fracture: an advanced technique for estimating stress intensity factors of 2d and 3d cracks. *Journal of Physics D: Applied Physics*, 42, 214004 (21pp).

SCHREIER, H. and SUTTON, M. (2002). Systematic errors in digital image correlation due to undermatched subset shape functions. *Proc. Soc. Exp. Mech. (USA)*, 49, 303 – 10.

SCHREIER, H. W., BRAASCH, J. R. and SUTTON, M. A. (2000). Systematic errors in digital image correlation caused by intensity interpolation. *Optical Engineering*, 39, 2915–2921.

SCRIVENS, W., LUO, Y., SUTTON, M., COLLETTE, S., MYRICK, M., MINEY, P., COLAVITA, P., REYNOLDS, A. and LI, X. (2007). Development of patterns for digital image correlation measurements at reduced length scales. *Experimental Mechanics*, 47, 63–77.

SMITH, B., LI, X. and TONG, W. (1998). Error assessment for strain mapping by digital image correlation. *Experimental Techniques*, 22, 19 – 21.

SMITH, T., BAY, B. and RASHID, M. (2002). Digital volume correlation including rotational degrees of freedom during minimization. *Proc. Soc. Exp. Mech. (USA)*, 49, 272 – 278.

SUN, Y., PANG, J. H. L., WONG, C. K. and SU, F. (2005). Finite element formulation for a digital image correlation method. *Applied Optics*, 44, 7357 – 7363.

SURREL, Y. (2004). Les techniques optiques de mesure de champ : essai de classification. *Instrumentation, Mesure, Métrologie*, 4, 11–42.

SUTTON, M., WOLTERS, W., PETERS, W., RANSON, W. and MCNEILL, S. (1983). Determination of displacements using an improved digital correlation method. *Image and Vision Computing*, 1, 133 – 139.

SUTTON, M. A., ORTEU, J.-J. and SCHREIER, H. (2009). *Image Correlation for Shape, Motion and Deformation Measurements: Basic Concepts,Theory and Applications*. springer publishing company, incorporated edition.

TONG, W. (2005). An evaluation of digital image correlation criteria for strain mapping applications. *Strain*, 41, 167 – 175.

TRICONNET, K., DERRIEN, K., HILD, F. and BAPTISTE, D. (2009). Parameter choice for optimized digital image correlation. *Optics and Lasers in Engineering*, 47, 728 – 737.

UNSER, M., ALDROUBI, A. and EDEN, M. (1993a). B-spline signal processing. i. theory. *Signal Processing, IEEE Transactions on*, 41, 821 –833.

UNSER, M., ALDROUBI, A. and EDEN, M. (1993b). B-spline signal processing. ii. efficiency design and applications. *Signal Processing, IEEE Transactions on*, 41, 834 –848.

VENDROUX, G. and KNAUSS, W. (1998). Submicron deformation field measurements: Part 2. improved digital image correlation. *Experimental Mechanics*, 38, 86–92.

VERHULP, E., RIETBERGEN, B. V. and HUISKES, R. (2004). A three-dimensional digital image correlation technique for strain measurements in microstructures. *Journal of Biomechanics*, 37, 1313 – 1320.

WAGNE, B., ROUX, S. and HILD, F. (2002). Spectral approach to displacement evaluation from image analysis. *Eur. Phys. J. AP*, 17, 247–252.

WANG, Y., SUTTON, M., BRUCK, H. and SCHREIER, H. (2009). Quantitative error assessment in pattern matching: Effects of intensity pattern noise, interpolation, strain and image contrast on motion measurements. *Strain*, 45, 160 – 178.

WATTRISSE, B., CHRYSOCHOOS, A., MURACCIOLE, J.-M. and NÉMOZ-GAILLARD, M. (2001). Analysis of strain localization during tensile tests by digital image correlation. *Experimental Mechanics*, 41, 29 – 39.

WU, T., CORET, M. and COMBESCURE, A. (2011). Strain localisation and damage measurement by full 3d digital image correlation: Application to 15-5ph stainless steel. *Strain*, 47, 49 – 61.

YOSHIKAWA, N., KUZUKAMI, S. and KUWAZURU, O. (2006). Identification of displacement field by x-ray ct. *Key Engineering Materials*, 326-328 I, 765 – 768.

ZAUEL, R., YENI, Y., BAY, B., DONG, X. and FYHRIE, D. (2006). Comparison of the linear finite element prediction of deformation and strain of human cancellous bone to 3d digital volume correlation measurements. *Journal of Biomechanical Engineering*, 128, 1 – 6.

APPENDIX: REGULARIZED SPECTRAL DIC

Applying the optimality condition on the regularized DIC yields the following equation:

$$\nabla_{\boldsymbol{v}_m}\Phi_{\text{SSD}} + \gamma\nabla_{\boldsymbol{v}_m}\Phi_{\text{REG}} = \mathbf{0} \quad m = 1, 2, 3, \cdots K \tag{6}$$

The gradient of the SSD criterion leads to the same equation (1.7a). As for the regularization term, consider the minimization of the Dirichlet Energy functional, i.e.:

$$\Phi_{\text{REG}} = \int_{\text{ROI}} \|\nabla_{\mathbf{x}}\mathbf{u}\|_F^2 \, \mathbf{dx} \tag{7}$$

The gradient of the above functional with respect to the unknown DOF is written as:

$$\nabla_{\boldsymbol{v}_m}(\Phi_{\text{REG}}) = 2\int_{\text{ROI}} \nabla_{\boldsymbol{v}_m}(\nabla_{\mathbf{x}}\mathbf{u}) : \nabla_{\mathbf{x}}\mathbf{u}\,\mathbf{dx} \quad m = 1, 2, 3, \cdots K \tag{8}$$

where (:) denotes the contraction operator (the generalization of the trace operator for arbitrary tensors). Considering that:

$$\nabla_{\mathbf{x}}\mathbf{u}(\mathbf{x}) = \sum_{n=1}^{K} (\boldsymbol{v}_n \otimes \nabla_{\mathbf{x}}\psi_n)(\mathbf{x}), \tag{9}$$

the gradient $\nabla_{\boldsymbol{v}_m}(\Phi_{\text{REG}})$ is simplified to the following:

$$\begin{aligned}\nabla_{\boldsymbol{v}_m}(\Phi_{\text{REG}}) &= 2\int_{\text{ROI}} \sum_{n=1}^{K} (\boldsymbol{v}_n \otimes \nabla_{\mathbf{x}}\psi_n) \cdot \nabla_{\mathbf{x}}\psi_m \, \mathbf{dx} \\ &= 2\int_{\text{ROI}} \sum_{n=1}^{K} (\boldsymbol{v}_n \nabla_{\mathbf{x}}\psi_n \cdot \nabla_{\mathbf{x}}\psi_m) \, \mathbf{dx}\end{aligned} \tag{10}$$

Using the spectral decomposition (1.14a) for the sought displacement field, the above gradient is restated in the following form:

$$\begin{aligned}\nabla_{\boldsymbol{\upsilon}_m}\left(\Phi_{\mathrm{REG}}\right) &= -2\sum_{n=-K/2}^{K/2-1}\boldsymbol{\omega}_n^T\boldsymbol{\omega}_m\boldsymbol{\upsilon}_n\int_{\mathrm{ROI}}\exp\left(\hat{\imath}\left(\boldsymbol{\omega}_m+\boldsymbol{\omega}_n\right)\cdot\mathbf{x}\right)\mathbf{dx}\\ &= -2\sum_{n=-K/2}^{K/2-1}\boldsymbol{\omega}_n^T\boldsymbol{\omega}_m\boldsymbol{\upsilon}_n\widetilde{\delta}_{[-m-n]}\\ &= 2\|\boldsymbol{\omega}_m\|_2^2\boldsymbol{\upsilon}_m \quad m=-K/2,-K/2+1,\cdots K/2-1\end{aligned} \tag{11}$$

where $\widetilde{\delta}_{[n]}$ is the unit impulse in the Fourier domain and the second line of the equation was deduced from the unit function's Fourier transform. Thus, the optimality condition for the regularized spectral DIC is written as:

$$\sum_n\widetilde{\mathbf{J}}_{[m-n]}\boldsymbol{\upsilon}_n+\gamma\|\boldsymbol{\omega}_m\|_2^2\boldsymbol{\upsilon}_m=\widetilde{\boldsymbol{\rho}}_{[m]} \tag{12}$$